Grant agreement no.: FCH-JU-325386

Support to Safety Analysis of Hydrogen and Fuel Cell Technologies

Report on Model Benchmarking Exercise "I"

The SUSANA project is co-funded by the European Commission within the 7th Framework Program

List of Authors

(randomly ordered by list of partner Institutions)

Olaf Jedicke (project coordinator)

Authors

Alexei Kotchourko
Ke Ren
Volodymyr Shentsov
Boris Chernyavskiy
Dmitriy Makarov
James Keenan
Vladimir Molkov
Daniele Baraldi
Daniele Melideo
Stella Giannissi
Ilias Tolias
Alexandros Venetsanos
Simon Coldrick

Content

1. Introduction

Within the SUSANA project a CFD benchmarking exercise has been carried out, in order to assess the model performance in predicting phenomena related to hydrogen safety. For the benchmarking exercise several experiments have been selected, in order to cover a whole range of phenomena: release and dispersion, ignition, deflagration and detonation. During the benchmark the best practices guidelines and other findings obtained din the WP3 are utilized.

The experiments for this benchmarking exercise have been chosen from the Model Validation Database (MVD) that has been created during the task 5.1 of the work package. The project partners have simulated different experiments involving the relevant phenomena.

- **Release and dispersion**: JRC, NCSRD and UU have simulated the GAMELAN (5mm, 180 NL/min) experiment related to helium release in a partially closed box of 1 m^3 volume. In addition, HSL and JRC have simulated the Standard Benchmark Exercise Problem (SBEP) V21 of HySafe Network of Excellence (NoE) regarding hydrogen release in a full scale single car garage.
- **Ignition:** UU has simulated the spontaneous ignition in a Pressure Relief Device (PRD).
- **Deflagration:** KIT has simulated a vented deflagration experiment (HIWP3-28_29_30) of 18% hydrogen-air mixture in a small (1 m^3) enclosure, while both NCSRD and UU have simulated a deflagration experiment of large-scale hemispherical stoichiometric hydrogen-air mixture in open atmosphere.
- **Detonation:** KIT has simulated the detonation experiments of uniform hydrogen-air mixture which have been carried out at the RUT tunnel facilities in Russia (KI-RUT Hyd05 and KI-RUT Hyd05).

2. Release and Dispersion Benchmark

2.1 GAMELAN experiment

2.1.1 Experimental description

The experimental set up (Cariteau & Tkatschenko, 2013) is a parallelepiped enclosure with a square base of 0.93m width and 1.26m height. The examined case has an opening of total area 32400 mm^2 (vent b: 180 x 180 mm).

The vent is located in the middle of the wall and 20mm below the ceiling. Figure 2-1 shows the top and side view of the facility for the examined case (vent b). Helium is injected in the enclosure through a 5mm nozzle. The injection point is located in the middle of the floor and 0.21m from it and the release rate is 180NL/min. the release is in quiescent environment and the ambient temperature is 295.51 K. Experimental geometry and conditions are summarized in Table 2-1.

Table 2-1. Summary of the experimental conditions.

Enclosure dimension l × w × h (mm)	Vent dimension w × h (mm)	Nozzle diameter D (mm)	Nozzle height (mm)	Release rate Q_{HE} (NL/min)	T (K)
930 × 930 × 1260	180 x 180	5	210	180	295.51

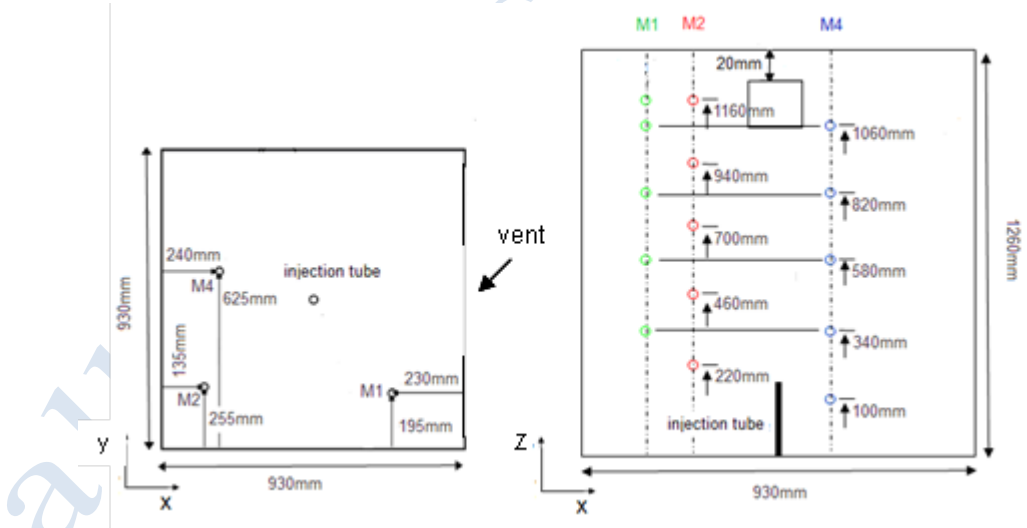

Figure 2-1. The top and the side view of the GAMELAN facility with ventb. The sensors' location is also shown.

The volume Richardson number has been verified by (Cariteau and Tkatschenko 2012) that is relevant parameter that characterizes the filling regime in a closed box, i.e. stratified, stratified with a homogeneous layer, homogeneous layer. The volume Richardson is given by

$$R_{iv} = g\frac{\rho_a - \rho_0}{\rho_0}\frac{V^{1/3}}{u_0^2} \quad (2.1)$$

where g is the gravitational acceleration, ρ_a is the air density, ρ_0 is the hydrogen density, V is the volume of the enclosure and u_0 is the average source velocity. For very low volumetric Richardson number ($R_{iv} < 2.5 \cdot 10^{-3}$) the upper layer descends almost until the bottom of the enclosure and a homogeneous mixture inside the enclosure is formed. For $0.0025 < R_{iv} < 3$, a homogeneous layer is formed in the upper layer of the enclosure, while a more or less stratified layer is formed in the lower part of the enclosure. For $R_{iv} > 3$, stratification without homogenous layer is observed.

Similarly in (Cariteau and Tkatschenko 2013) the relevance of the volume Richardson with the filling regime in partially closed box has been verified. In the vented case in very low R_{iv} values the dispersion is homogeneous over the height of the enclosure. The critical value of R_{iv} to reach the homogeneous mixture inside the enclosure is the approximately same as in the closed case, ie. 0.0023. For $R_{iv} > 1$ there is an upper homogeneous layer followed by a steep gradient and a lower homogenous layer. The thickness of these layers, the concentration levels and the gradient depend on the vent size.

In the examined case the R_{iv} is 0.027, i.e. smaller than unity, therefore, a homogenous layer over the height of the enclosure is expected.

2.1.2 JRC modelling

2.1.2.1 Modelling strategy

The main parameters of the CFD simulations are:

- CFD code: ANSYS CFX 15.0
- Isothermal simulation.
- Source modelled as a 3D pipe.
- Facility wall thickness 5 mm.
- Multicomponent flow model: the code assumes that the various components of a fluid are mixed at the molecular level and that they share the same mean velocity, pressure and temperature fields, and that mass transfer takes place by convection and diffusion.
- Symmetry is assumed.
- The computational domain outside the box is extended in all the three directions to avoid boundary conditions at the opening.
- SST model Transitional model*:* The k-ω based Shear-Stress-Transport (SST) model was originally designed to give highly accurate predictions of the onset and the amount of flow separation under adverse pressure gradients by the inclusion of transport effects into the formulation of the eddy-viscosity. This results in a major improvement in terms of flow separation predictions but not only. The full transition model is based on two transport equations, one for the intermittency and one for the transition onset criteria in terms of momentum thickness Reynolds number. It is called 'Gamma Theta Model' and it is the recommended transition model for general-purpose applications. It uses a new empirical correlation (Langtry and Menter) which has been developed to cover standard bypass transition as well as flows in low free-stream turbulence environments. This built-in

correlation has been extensively validated together with the SST turbulence model for a wide range of transitional flows.
- Advection scheme: High resolution.
- Transient scheme: Second order backward Euler.

2.1.2.2 Mesh description

A symmetry plane passing through the helium source was modelled. The geometry model is constituted by two main domains as shown in Figure 2-2: the “test facility” domain which represents the CEA-GAMELAN facility/box, and a much larger “external” domain to reduce the potential effects of an outlet boundary condition when it is placed directly at the box.

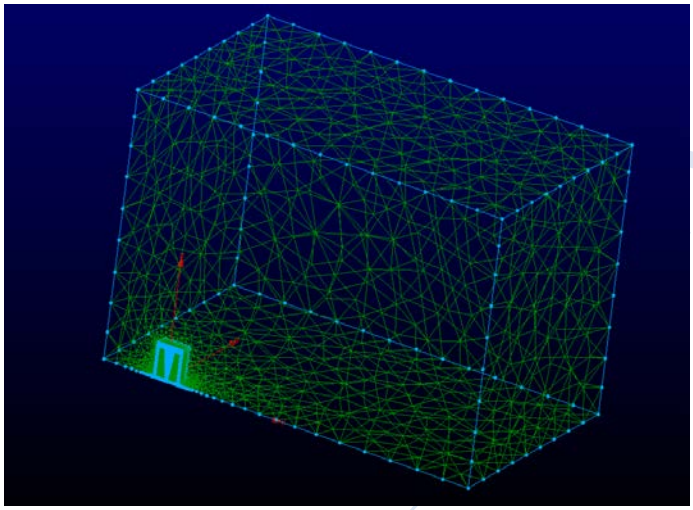

Figure 2-2. External domain and test facility domain.

A tetrahedral mesh was generated as illustrated in Figure 2-3. The total number of nodes is 212k. The mesh has grid refinement in selected zones of the test facility in order to better understand the flow behaviour (e.g. finer grid resolution at the source and at the top of the facility where the flow impinges against the wall).

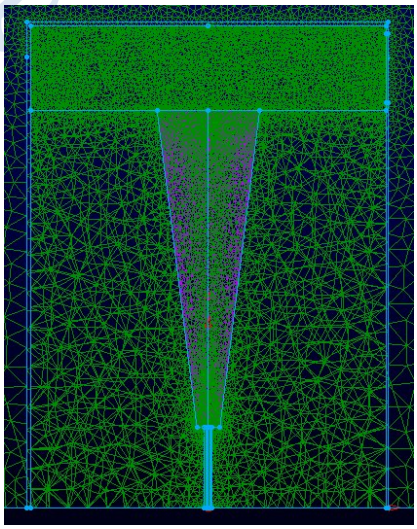

Figure 2-3. Detail of the mesh at the symmetry plane.

2.1.2.3 Sensitivity analysis

In the framework of the HyIndoor project, several sensitivity analyses were performed for the GAMELAN facility with different vent size (i.e. 3.6 cm x 90 cm, 18 cm x 18 cm and 90 cm x 18 cm) at different mass flow rates (e.g. 4 NL/min and 60 NL/min). Some of them are listed below:

- Mesh typology (hexahedral or tetrahedral elements)
- Grid independency simulations with increasingly finer mesh resolutions. Mesh refinements in different regions of the domain were also considered.
- Transient simulation: time step imposed at 0.1 s; a simulation using an adaptive time step scheme (starting with an initial time step of 0.001 s) shows similar results. It must be emphasized that CFX is an implicit code.
- Different turbulent models
- Simulations without symmetry were performed and give identical results.

2.1.2.4 Results

The comparison between the CFD result and the experimental data at fixed times (i.e. 100, 475 and 870) is shown in Figure 2-4. The predicted results (red line in the figure) slightly underestimate the He concentration at the beginning of the simulation. At later times, the simulation results and the experimental data are overlapping for the 7 sensors that are located at a height larger than 0.4 m. For the 3 sensors below 0.4 m, the simulated concentrations are slightly below the experimental measurements. Overall the CFD results are in good agreement with the experimental data.

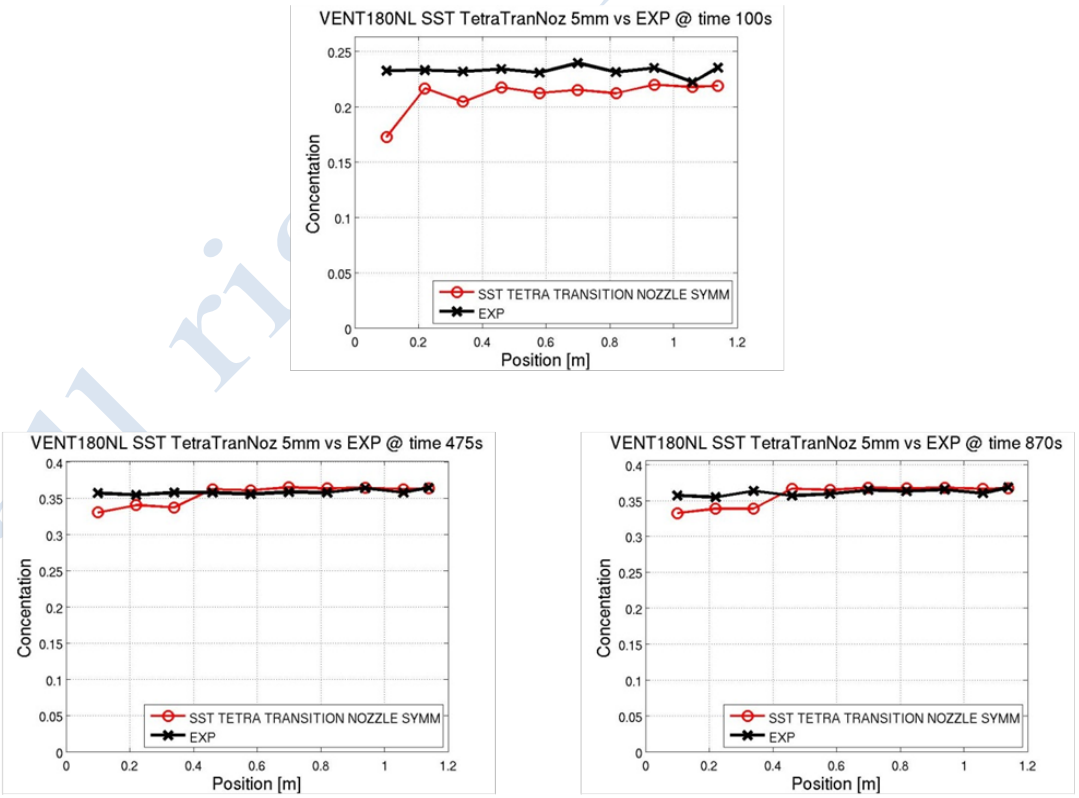

Figure 2-4. Helium concentration during injection with the 5mm source at 180 NL/min.

Wall thickness sensitivity

An additional geometry models was generated to reproduce the facility without any wall thickness, in order to understand influence of the wall thickness on the results, as shown in Figure 2-5. Due to the absence of the wall thickness, the He concentrations decrease inside the facility, causing an under-estimation of the results during the whole simulation.

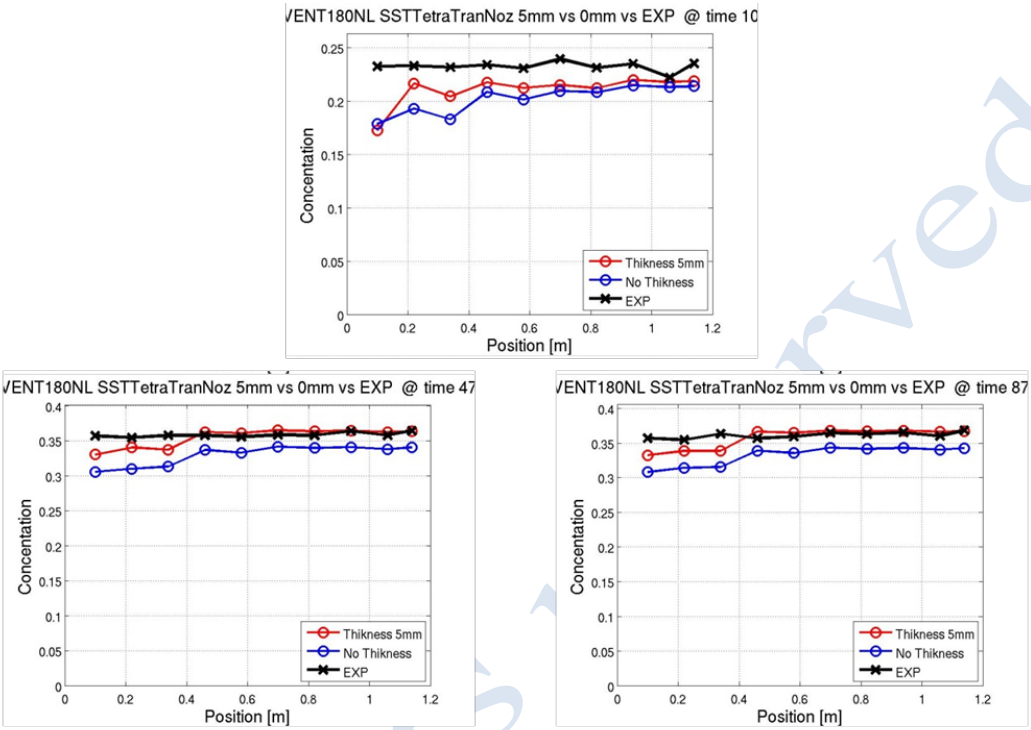

Figure 2-5. Helium concentration during injection with the 5mm source at 180 NL/min; influence of the facility wall thickness.

2.1.3 NCSRD modelling

2.1.3.1 Simulation set-up

For the simulation the ADREA-HF CFD code has been used. The 3D time dependent conservation equations of mass, momentum and energy are solved. To model the turbulence the standard k-ε with extra buoyancy terms has been used. The good performance of the k-ε model in simulating similar cases has been verified in (Giannissi et al. 2015).

The enclosure is naturally ventilated through the vent. As helium arrives in the vent region it flows out through the upper part of the vent and fresh air flows in through the lower part of the vent due to the density difference. This should be taken under consideration during the domain design. Domain extension, especially, in the dimensions where flow occurs is essential for accurately simulating the exchange flow through the vent (see Figure 2-6). Therefore, the domain was extended almost half box's width (0.5m) along the x-and z-direction. On the y-direction less extension is needed, and, therefore, the domain was extended approximately ¼ box's width (0.2m).

A wall thickness equal to 5mm was assumed only for the wall with the vent. All other walls have zero thickness.

According to the best practices (SUSANA, 2014) grid resolution on the nozzle and in regions where high gradients are expected is necessary. Therefore, the grid is refined on the source, near the walls and near the vent region. Different grid resolutions were tested to perform a grid independency study. First, three different grid sizes were examined with main difference the number of cells used to discretize the source. Table 2-2 shows the grids' characteristics. Symmetry was assumed along the y-axis in all grids.

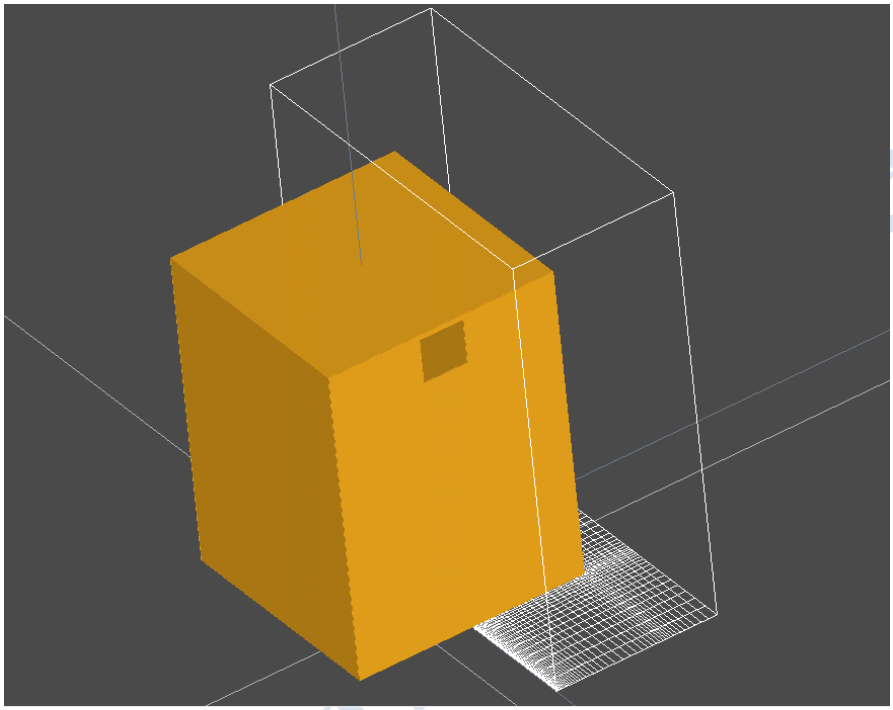

Figure 2-6. The GAMELAN box and the domain for the simulation. The grid (grid2) on ground plane is also shown.

Table 2-2. Grid characteristics.

	number of cells (in the symmetric domain)	**cells along inlet diameter**	**minimum cell size (x and y direction)**	**minimum cell size (z direction)**	**expansion ratio**
Grid1	222 180	1	0.005	0.01	1.1-1.14
Grid2	263 623	2	0.0025	0.01	1.1-1.14
Grid3	361 228	4	0.00125	0.01	1.1-1.14

Then, another two grids were tested with 2 cells along diameter like grid2, but different total number of cells (a coarser and a finer grid than grid2 were constructed). Table 2-3 shows the characteristics of the two new grids. Grid2 characteristics are repeated in Table 2-3 for direct comparison with the other two grids.

Table 2-3. Grid characteristics.

	number of cells (in the symmetric domain)	cells along inlet diameter	minimum cell size (x and y direction)	minimum cell size (z direction)	expansion ratio
Grid2a	123 830	2	0.0025	0.025	1.12
Grid2	263 623	2	0.0025	0.01	1.1-1.14
Grid2b	359 738	2	0.0025	0.008	1.1-1.14

The boundary conditions that will be applied are also of great significance for predicting accurate results and achieving fast convergence. No-slip conditions have been applied on the walls. In the outlets along x and y-axis zero gradient boundary conditions have been applied, since the boundary is set far enough from disturbances. On the top boundary, in which helium is directed, a constant pressure condition was imposed. This boundary condition is more appropriate, since the flow is buoyancy driven (Versteeg and Malalasekera 2007).

For initial conditions zero values were set for the velocity. The temperature was set according to the experimental measurement (see Table 2-1).

For the time discretization the 1st order implicit scheme is used. The CFL number was kept constant and equal to 80, in order to restrict the increase of time step. For the coarser grid (grid1), a lower CFL number (equal to 30) was tested that decreased 2.6 times the maximum time step and showed that the results are not affected.

For the convective terms the 2nd order MUSCL scheme is used. Simulations with 3rd order numerical scheme (QUICK) have also been carried out in the past shown little improvement of the results and slower convergence. A 1st order scheme has been also tested and although it was faster it under-predicted the concentration levels in the lower part of the enclosure. Therefore, the 2nd order scheme was preferred which exhibits better convergence behavior compared to the higher order scheme and more accurate results compared to the 1st order scheme.

2.1.3.2 Model performance measures

A useful tool to evaluate the performance of the dispersion models against the experimental dataset is the statistical analysis. The statistical measures often consist of one or more statistical parameters, and/or a graphical presentation. These measures compare the predicted values with the observed (measured) values at all available sensors. There are two types of measures: one type that indicates whether the model in general under- or over-predicts the measurements and one type that indicates the level of scatter. Usually, a pair of the two types is used, in order the statistical analysis to be complete. Two pairs of different statistical performance indicators are recommended (these indicators are also recommended by (Hanna 1989) and (Hanna, Chang, and Strimaitis 1993) for evaluating air dispersion models; fractional bias (FB) and normalized mean square error (NMSE), geometric mean bias (MG) and geometric mean variance (VG).

FB and NMSE

FB is the mean error that defines the residual of the observed (Co) and the predicted concentrations (Cp). The bias is normalized by the data-set averaged concentration. FB is an indicator if the model overall under-over predicts the concentration. FB ideal value is zero, negative FB values show overprediction and positive FB values indicate underprediction.
NMSE indicates the scatter of the entire dataset and estimated the overall deviation between the observed and the predicted values. NMSE ideal value is zero. Small values indicate better model performance.

The FB and NMSE is calculated by

$$FB = 2\frac{\overline{C}_o - \overline{C}_p}{\overline{C}_o + \overline{C}_p} \tag{2.2}$$

$$NMSE = \frac{\overline{\left(C_o - C_p\right)^2}}{\overline{C}_o \cdot \overline{C}_p} \tag{2.3}$$

The overbar denotes the average over the entire dataset.

MG and VG

MG measures the relative mean bias, and by taking the logarithm of the observed to predicted ratios rather than just the ratio, the asymmetry in the averaging process is over come, and MG value is less influenced by extreme ratios. The MG ideal value is unity. MG values smaller than unity indicate overprediction and values higher than unity show underprecition. MG values of 0.5-2.0 can be thought of as “factor of two” overpredictions and underpredictions in the mean, respectively. VG measures the relative scatter. The ideal value is unity and VG values close to unity indicate less scatter. VG value of about 1.6 indicates a typical factor of two scatter between the individual pairs of measured and predicted values.

The MG and the VG is calculated by

$$MG = \exp\left[\overline{\ln\left(\frac{C_o}{C_p}\right)}\right] \tag{2.4}$$

$$VG = \exp\left[\overline{\ln\left(\frac{C_o}{C_p}\right)^2}\right] \tag{2.5}$$

FB and MG are measures of mean bias and indicate only systematic errors, whilst NMSE and VG reflect both systematic and unsystematic (random) errors. MG and VG are more appropriate for dataset where both observed and predicted values vary by many orders of magnitude. However, MG and VG are strongly influenced by extremely low value, whilst FB and NMSE are strongly influenced by infrequently occurring high observed and predicted values.

A “good” model would be expected to have mean bias $\pm 30\%$ of the mean, i.e. $|FB| < 0.3$ or $0.7 < MG < 1.3$, and random scatter about a factor of two to three, i.e. NMSE<1.5 or VG<4.

Besides the statistical parameters graphical presentation can also be used to evaluate the dispersion models: scatter plot and MG vs VG plot. Scatter plot is a diagram with the observed values versus the predicted values of concentration at each sensor. The points of the

perfect model would be along the line y=x. The closer to this line the points are the better the model's performance is. In MG vs VG plot a perfect model would be placed at MG=1 and VG=1.

2.1.3.3 Results and discussion

Figure 2-7 shows the time histories of the predicted and the measured helium concentrations with the three grids that differ in the number of cells along the source diameter. It shows that the results have some discrepancies. The simulation with the finer grid underpredicts the concentration especially at the early stage of the release. The simulations with the two coarser grids are similar at most of the sensors.

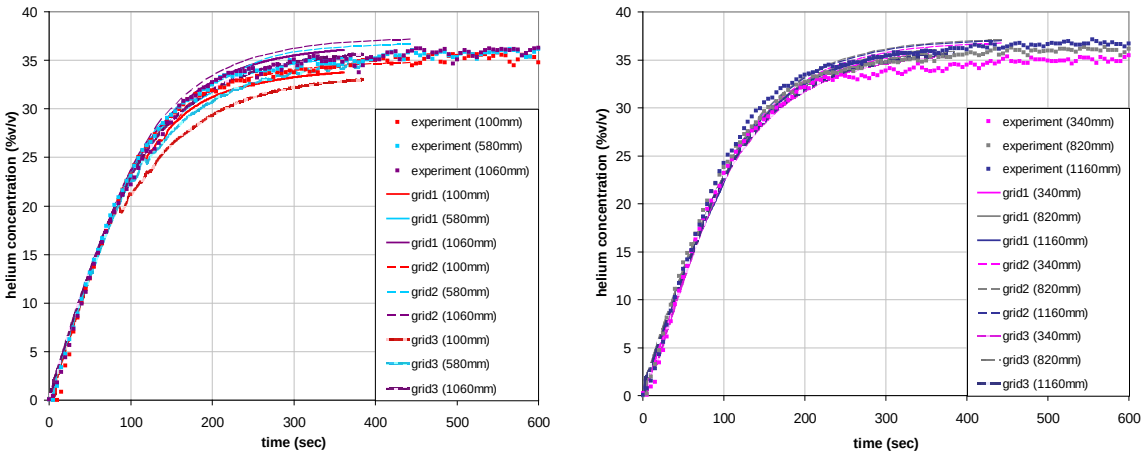

Figure 2-7. The predicted versus the measured helium concentration time histories for the sensor mast M4 (left) and sensor mast M1 (right) with grid1, 2 and 3.

A measure to compare the computational results obtained by the different grids is the relative error between them. The relative error is defined as the difference between the coarse grid result and the fine grid result to the fine grid result (relative error= $(C_{coarse}- C_{fine})/ C_{fine}$). The relative error is calculated in all sensors at all time steps and the maximum value is recorded: the smaller the relative errors the closer to grid independency. Off course, zero relative errors indicate that grid independency has been achieved.

The relative error between the two fine grids (grid2 and grid3) is ranged from 0.001% -27.5% for all sensors and all available time steps. The extrema (very high and very low errors) are found at the early stage of the release at the bottom and at the top sensors respectively. As release is progressed the high errors decrease and the low errors increase and they are ranged from approximately 8% at the bottom sensors to about 4% at the top sensors. Close to steady state the relative error between grid2 and grid3 is less than 4% at most of the sensors, except for the bottom sensors where the error is approximately 5%. The relative error between grid1 and grid2 varied from 0.002% to 11% for all sensors and all available time steps. Close to steady state the difference between the two predictions decreases and the relative error at all sensors is approximately 2%.

Figure 2-8 shows the time histories of the predicted and the measured helium concentrations with the three grids with 2 cells along the diameter but different total cell number. The results with the coarser grid (grid2a) are quite different from the results with the two finer grids. The concentration levels with the coarser grid are under-predicted at all sensors, as steady state approaches. Moreover, unphysical oscillations are observed. The relative error between the

two fine grids (grid2 and grid2b) is ranged from 0.0008%-7% for all sensors and all available time steps. At steady state the relative error is less than 4% at all sensors.

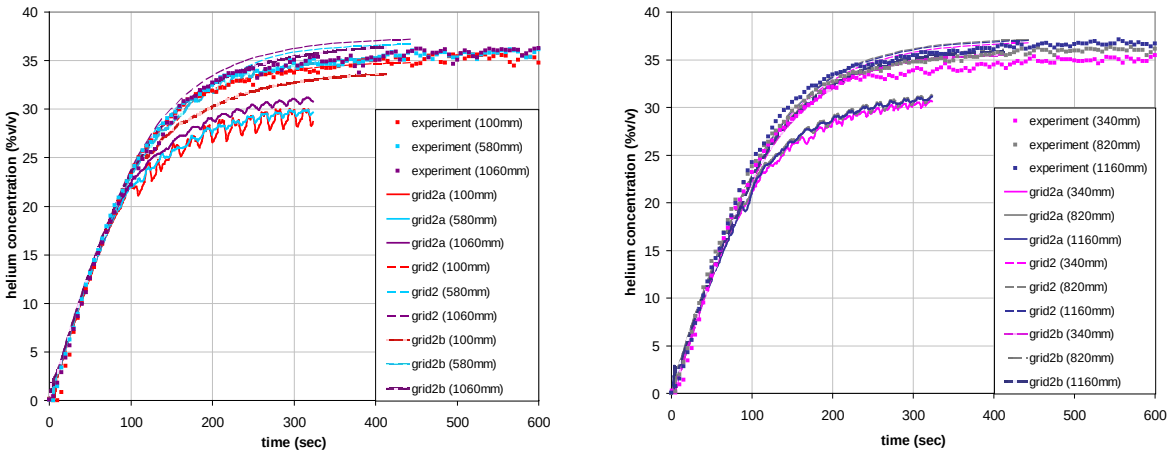

Figure 2-8. The predicted versus the measured helium concentration time histories for the sensor mast M4 (left) and sensor mast M1 (right) with grid2a, grid2 and grid2b.

Comparing the results with grid2b and grid3 we observe that close to the steady state the predictions are similar. The main difference of the grids is the number of cells along the source diameter, and consequently the minimum cell size. However, the total number of cells is almost the same. Therefore, it we can be concluded that the 2 cells discretization along the source diameter is sufficient, but small expansion ratio inside the box is necessary.

The small relative error between the predictions with grid2 and grid3, and between grid2 and grid2b in conjunction with the lesser computational cost that simulation with grid2 demands, the prediction with grid2 is considered sufficient and close to independent. Therefore, for the prediction with grid2 extra material is presented next.

Figure 2-9 (left) shows the helium concentration with grid2 versus the height of the enclosure in comparison with the measured concentration at steady state (400 sec). The formation of homogenous mixture over the entire height of the enclosure, as the volume Richardson number that is less than 1 indicates (see Section 2.1.1), is supported by the measurements which record almost same concentration levels over the entire enclosure. An almost homogenous mixture is also predicted by the simulation, as the vertical profile shows. In Figure 2-9 (right) with the concentration contours the produced homogenous mixture is shown and the bidirectional flow through the vent is also obvious. The helium flows out the facility through the upper part of the vent, while fresh air enters the facility through the lower part of the vent.

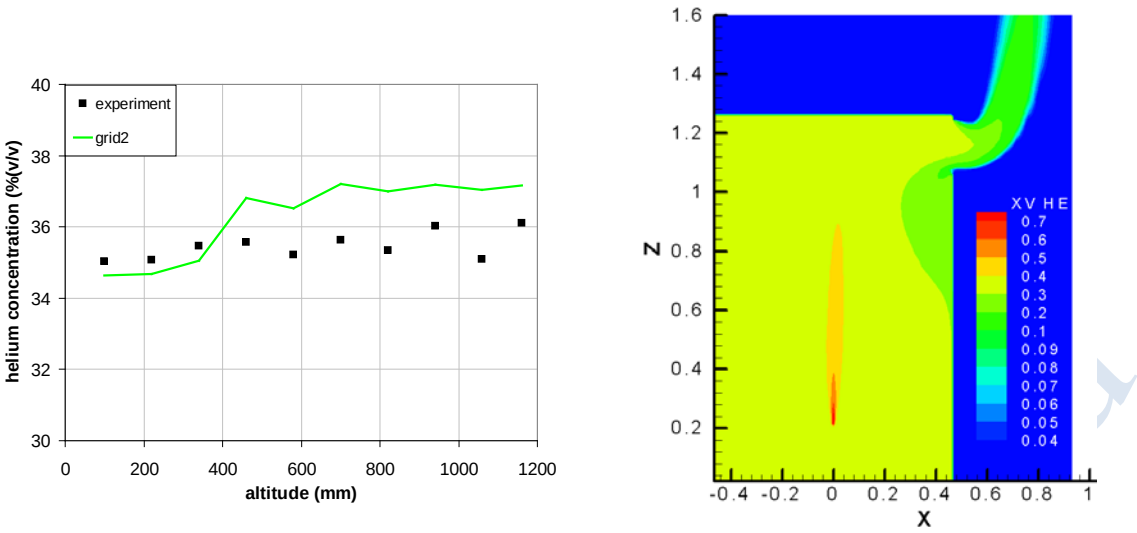

Figure 2-9. The predicted helium concentration (with grid2) compared with the experimental one at steady state (400 sec) over the height of the enclosure (left) and the predicted helium concentration contours on symmetry plane and at steady state (right).

Further statistical analysis has been performed for the grid2 simulation. Table 2-4 presents the statistical measures. With FB absolute values below 0.3 and MG values range between 0.7 and 1.3 the model can be considered as a "good" model. The small values of the NMSE and the VG indicate a random scatter about a factor of two to three. The negative FB value and the MG value below unity reveals that the model overall overpredict the helium concentration at steady state.

Table 2-4. The statistical measures for the grid2 simulation.

	ideal value	prediction
FB	0	-0.025
NMSE	0	1.52
MG	1	0.97
VG	1	1.001

Figure 2-10 shows the scatter plot and the MG versus VG plot at steady state. In the scatter plot the results are close to the diagonal line (ideal), and in the MG vs. VG plot they are placed close to unity. This indicates a good model performance. Furthermore, according to the scatter plot the model overpredicts the concentration at steady state at the majority of the sensors. However, in the lower part of the enclosure the model tends to slightly under-predict the concentration (point below the diagonal line).

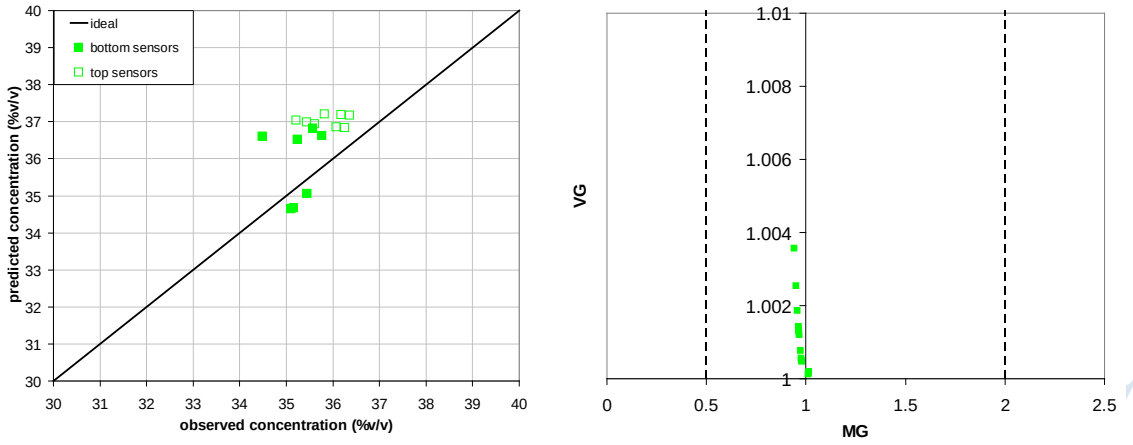

Figure 2-10. The scatter plot with the observed versus the predicted helium concentration (right) and the MG versus VG plot (left) for the grid2 simulation.

2.1.3.4 Conclusions

The GAMELAN experiment with helium release through a 5mm nozzle and release rate 180NL/min has been simulated by NCSRD. The simulation is consistent with the experiment, though it tends to slightly under-predict the concentration on the lower part of the enclosure and to overpredict it on the upper part of the enclosure. The standard k-ε model proved to be appropriate to simulate accurately enough this release case. The good performance of the k-ε model was expected, because the Reynolds number of the release is very high (~7000) and corresponds to fully turbulent flow.

According to the experiment and based on the volume Richardson number a homogeneous mixture over the height of the enclosure was produced. An almost homogeneous model was also predicted by the simulation.

A statistical analysis was performed and showed that the prediction overall over-predicts the concentration at steady state. The small FB and MG values indicate that the model can be considered as good.

2.1.4 UU modelling

2.1.4.1 Governing equations

Dispersion of helium in the enclosure is simulated using Navier-Stokes equations. Turbulence modeling is performed with three different models – the laminar, the standard *k-ε* and the Large Eddy Simulation (LES).

Laminar model does not calculate the turbulent viscosity and therefore is strictly appropriate for laminar flows only. The “upper” value of the laminar flow of water in the pipe is said to correspond to Reynolds number *Re*=2100 (Reynolds, 1883). However, the transition from laminar to turbulent flow is not sharp and it is commonly accepted that a flow in a pipe is laminar when Reynolds number is below about *Re*=1000, and the flow is turbulent when *Re*>4000. The case under consideration, with Reynolds number Re=6968, should be considered turbulent. It should be noted, however, that much of the gas mixture in the enclosure far from the release pipe as well as air outside of the enclosure are in the environment with much lower Reynolds numbers. Finally, it is known that if a laminar model

is chosen for simulation of a flow which is in fact turbulent, the convergence of simulations is difficult to achieve and the simulation would obviously not give a correct solution.

The standard k-ε model is the two-equation turbulence model which includes transport equations for the turbulence kinetic energy, k, and the turbulence dissipation rate, ε, the description of which can be found elsewhere (Launder and Spalding, 1972). The turbulent viscosity is calculated by combining k and ε as follows: $\mu_t=\rho C_\mu k^2/\varepsilon$, where C_μ =0.09 is the model constant. In the derivation and application of the k-ε model, it is assumed that the flow is fully turbulent, and the effects of molecular viscosity are negligible. Therefore, the standard k-ε model is applicable to turbulent flows only and its performance for laminar flows is expected to be poor due to a neglect of the physical requirement to choose a model that corresponds to a flow type.

Finally, the dynamic LES Smagorinsky-Lilly (Lilly, 1992), the turbulent viscosity is calculated as $\mu_t=\rho L_S^2|\bar{S}|$, where $L_S=min(\kappa l, C_s\Delta)$ is the mixing length at sub-grid scales, in which κ is the von Kármán constant, $|\bar{S}|\equiv(2\bar{S}_{ij}\bar{S}_{ij})^{1/2}$, where S_{ij} is the strain tensor, l is the distance to the closest wall, C_s is the Smagorinsky coefficient (a constant in the original Smagorinsky model), and $\Delta=V^{1/3}$ is the local grid scale computed by a volume of a computational cell. The main difference between the original Smagorinsky model (Smagorinsky, 1963) and the dynamic Smagorinsky-Lilly (Lilly, 1992) model is that the coefficient C_s is calculated dynamically based on the information provided by the resolved scales of motion rather than to be the constant as in the original model. To determine the model coefficient the use of two filters is required, the grid filter and the test filter, the model uses information on the energy content of the smallest resolved scales. Since the Smagorinsky coefficient in the dynamic model is the square of its original quantity according to Lilly (1992), $C_S=\sqrt{C}$.

2.1.4.2 Simulation approach

Calculation domain

Simulation used a block-structured hexahedral computational grid. Calculation domain encompassed both the enclosure itself and a part of surrounding space in order to avoid boundary conditions being imposed directly at a vent. This external computational domain a form of hexahedron surrounding the enclosure measuring $H\times W\times L$ = 2.5 × 3.0 × 2.5 m (see Figure 2-11 and Figure 2-12).

The helium inflow boundary is a polygon inscribed in a circle with a cross-sectional area consisting of 20 control volumes (CVs, 8 CVs across the diameter) for the 5 mm diameter pipe. The polygon cross-section area is equal to the cross-section area of the enclosure of the pipe. The inflow boundary is located inside the release pipe at distance 5 cm from the pipe exit. There are 10 cells along the pipe axis from the inflow boundary to the pipe exit for all grids.

Computational grid was generated as follows. The vertical size of CVs at both the pipe exit and at the ceiling of the enclosure was 7 mm (the same as inside the pipe). The CV expansion ratio of 1.05 was applied both downwards from this area, and upwards from the release source (Figure 2-11). Then the expansion ratio of 1.05 was applied both downwards from this area, and upwards from the release source. The largest vertical cell size generated this way was 9.2 mm. This cell size was reached in 6 steps from the top and in 13 steps from the bottom. Remaining cells height was 9.2 mm. The total number of cells along the height of the

enclosure in grid is 155. The total number of CVs within the enclosure is 834,710, and the entire domain contains 2,338,620 CVs. The vent was resolved by H W=26×69 cells. The expansion ratio applied in all horizontal directions from the release point was 1.05 (unless the mesh from walls was encountered). The expansion ratio applied from the walls towards the release point and outside the enclosure was 1.10.

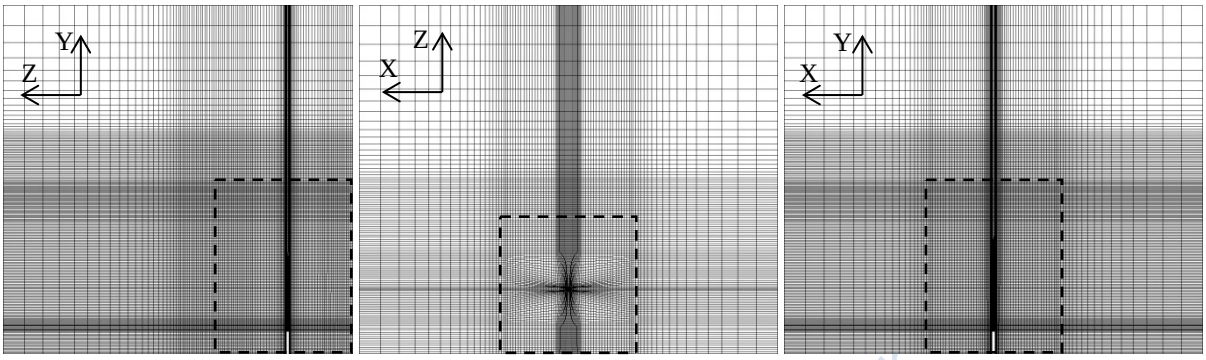

Figure 2-11. Grid cross sections: x=0 (left), y=0 (middle), z=0 (right). The enclosure boundaries are shown by dashed lines (Molkov and Shentsov, 2014).

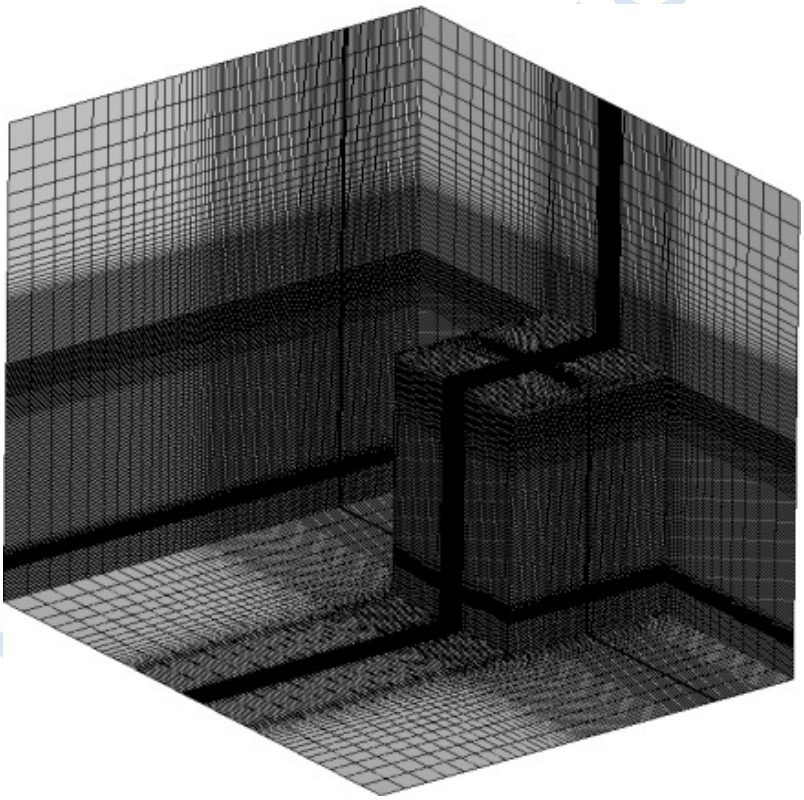

Figure 2-12. 3D view of the mesh (Molkov and Shentsov, 2014).

Initial and boundary conditions

Initial temperature of released helium and air temperature in the domain were set to the value specified in Table 2-1. Non-slip boundary conditions were applied to all solid surfaces. Release was initiated through the velocity inlet boundary condition with 100% of helium and constant velocity throughout the inlet cross-section. Initial inlet turbulence intensity and length scale were calculated from equations $I=0.16Re^{-1/8}$ and $L=0.07d$ respectively with

Reynolds number calculated as $Re=(\dot{V}d)/(\nu A)$, where $\nu=\mu/\rho$ is the kinematic viscosity, in which ρ is the density that was obtained taking into account different release temperature T, and μ=1.87e-5$(T/T_0)^{0.7}$ is the helium dynamic viscosity (Peterson, 1970), where T_0=273.15K is the reference temperature. Initial velocities were set to zero in the whole calculation domain. The "pressure outflow" condition was set at the domain boundaries with the same temperature as in the domain and the gauge pressure equal to zero. The main constants in applied models are as follows: standard k-ε (Sc_t=0.85, C_μ=0.09, $C_{1-\varepsilon}$=1.44), LES (Sc_t=0.7, C_S is calculated dynamically). Somewhat higher value of turbulent Schmidt number for standard k-ε model of 0.85 compared to commonly applied value of 0.7 was chosen based on preliminary simulations of these experiments.

2.1.4.3 Numerical details

- Code: Numerical simulation was performed using ANSYS Fluent14.5 CFD software
- Discretisation: finite volume
- Solver type: coupled, pressure based solver
- Transient numerical scheme: bounded 2nd order implicit
- For the three turbulence models were used in this simulation:
  - Laminar
    - Numerical scheme for convective terms: second order upwind for momentum, energy and species equations
    - CFL number: 175
  - k-ε
    - Numerical scheme for convective terms: second order upwind for momentum, energy and species equations
    - CFL number: 178
  - LES
    - Spatial discretization of convective terms: bounded central differencing scheme for the momentum equation and second order upwind scheme in the species and energy equations
    - CFL number: 208

2.1.4.4 Results and Discussion

The results obtained from these three models runs were compared against experimental data obtained at CEA. Experimental data provided steady-state concentrations of helium along the height of the enclosure, while the numerical simulations also allowed monitoring of concentration evolution during the release. In order to keep calculation time within practical limits, a relatively high *CFL* numbers of 175 – 200 were applied in all three models, specifically *CFL*=175 for the laminar model, *CFL*=208 for the LES model, and *CFL*=178 for the standard k-ε model. It should be noted that these CFL numbers occur in the relatively small number of cells near release origin where the flow velocities are maximal.

Figure 2-13 (left) shows distribution of helium concentration along the enclosure height at five different moments of time (50, 100, 150, 475, and 533 s) simulated by the laminar model (curve designated S7) and the steady-state concentration distribution observed in experiment (solid curve designated E5). It is seen that the steady-state near-constant concentration distribution observed in the experiment was not reached even after 533 seconds – while (see Figure 2-13, right) LES and standard k-ε model demonstrate that the steady state should be

reached no later than by 475 second. At this point simulation was terminated due to its excessive running time (already twice the duration of LES and *k-ε* runs, see Table 2-5). It can be concluded that the laminar simulation is not able to adequately reproduce the behaviour of helium dispersion in this experiment. This result is not surprising, as the Reynolds number for this release parameter is equal 6968 (Molkov and Shentsov, 2014), i.e., lying in the turbulent flow area for which laminar model is ill suited.

Figure 2-13 (right) shows distribution of helium concentration along the enclosure height at four different moments of time (50, 100, 150, and 475 s) simulated using the LES (curve S8) and the standard *k-ε* (curve S9) models, compared against the steady-state helium concentration distribution in experiment (curve E5). It is seen that both simulations reached steady-state distribution by 475 second after beginning of the release.

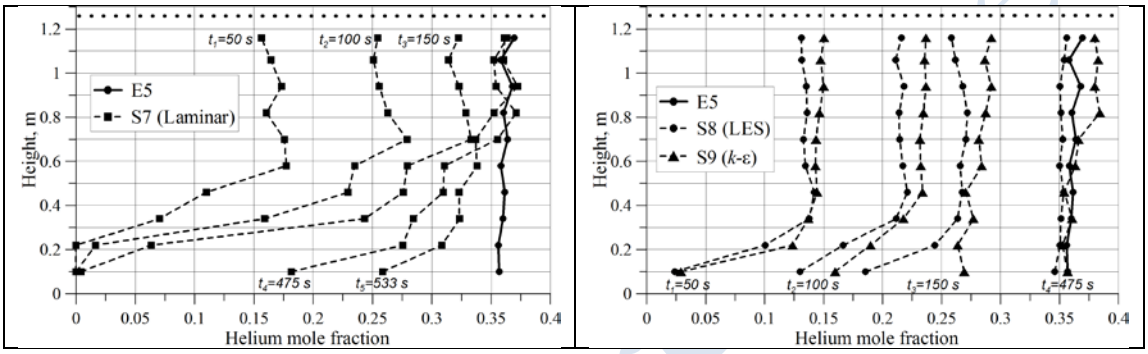

Figure 2-13. Left: comparison of experimental steady-state concentration distribution measurements (solid line "E5") with results obtained from the laminar model (CFL=175) data illustrated by dashed curves "S7". Right: comparison of simulations using the LES (CFL=208, dashed curves with round markers "S8") and the standard k-□□ (CFL=178, dashed curves with triangular markers "S9") models against the experimental steady-state concentration distribution (solid lines, "E5").

Table 2-5. Summary of numerical simulation parameters.

No.	*Δt*, s	*CFL*	Release time, s	Model applied	Number of CPUs	CPU rate, s/h	CPU time, days	*Re*
S7	0.005	175	475	Laminar	54	0.38	52	6968
S8	0.005	208	475	LES	48	0.74	27	6968
S9	0.005	178	475	Standard *k-ε*	54	0.73	27	6968

The performance of the LES model and the standard *k-ε* model is noticeably better compared to the laminar model in the prediction of the steady-state concentrations in this turbulent flow release experiment, as can be expected. Comparing the results of the LES and *k-ε* simulations, the LES model insignificantly under predicts the (near-uniform) concentration in this experiment, while correctly predicting its (near-) uniform character. Meanwhile the standard *k-ε* model very closely matches experimental data in the lower part of enclosure, and slightly over predicts the concentration at the top of the enclosure, thus predicting a two-layers distribution rather than experimentally observed uniform mixture.

It can be concluded that the best performance in simulation of the turbulent release and following dispersion is, therefore, demonstrated by the LES model, which produces correct near-uniform distribution of helium concentration with insignificant under prediction of its maximum value. In comparison, the standard *k-ε* model also gives helium concentration levels close to the experiment, but predicts layered structure of hydrogen distribution which

was not observed in experiment. The laminar model does not provide good match with experimentally observed data within a reasonable running time. Detailed description of numerical results can be found in (Molkov and Shentsov, 2014) and (Giannissi et al., 2015).

2.1.4.5 Conclusions

Numerical simulation of helium release in the enclosure with one vent had been carried out using different numerical approaches. Numerical results were compared with the results of a series of experiments with helium release and dispersion within the 1.26 x 0.93 x 0.93 m enclosure performed at CEA. Three CFD models were applied, including the laminar, the dynamic LES, and the standard k-ε model.

LES model was proven capable to reproduce experimental data for 180 Nl/min release with acceptable accuracy. Standard k-ε model was also able to reproduce experimental data at the end of the release, although it predicted the appearance of layered concentration structure which was not observed in experiment (or LES). The laminar model was not capable to reproduce experimental data with reasonable accuracy.

The successful performance of the LES model was to some extent predictable, since the conditions of the simulation covered full range of flow types from fully turbulent (in the vicinity of the release) to the essentially laminar (far from the release origin) and LES is the only model of three applied which is able to simulate both laminar and turbulent flows in one computational domain simultaneously (the laminar viscosity is recovered by the LES model in regions where the flow laminarisation takes place).

2.1.5 Overall Conclusions

For the release and dispersion benchmarking the GAMELAN experiment related to helium release inside a partially enclosed box with one vent was chosen and simulated by JRC, NCSRD and UU. The flow of the experiment was fully turbulent and according to the volume Richardson number a uniform mixture over the entire height of the enclosure is produced at steady state.

The project partners simulated the experiment using their own methodology and CFD code. All modeling set ups were relied on the best practices guidelines that were developed within this project. Overall, the predictions exhibited good performance. All turbulence models (standard k-ε model, SST transitional model and LES model) predicted accurately enough the concentration levels, while the laminar model was not able to adequately reproduce the behaviour of helium dispersion. K-ε model tends to overpredict the concentration on the upper part of the enclosure and to under-predict it on the lower part of the enclosure. SST transitional model slightly under-predicts the concentration on the bottom sensors, while on the upper part of the enclosure the prediction is in very good agreement with the experiment. LES model produces very good results; however, it tends to slightly under-predict the concentration at most of the sensors.

Sensitivity analysis concerning the wall thickness performed by JRC showed that the simulation with no wall thickness leads to more under-prediction of the concentration.

2.1.6 References

Becker T., Ebert F., Vergleich zwischen Experiment und Theorie der Explosion großer, freier Gaswolken. Chem.-Ing.-Tech., V.57, N.1, pp 42-45, 1985.

Breitung, W., Dorofeev, S.B., Efimenko, A.A., Kochurko, A.S., Redlinger, R., Sidorov., V.P., Large Scale Experiments on Hydrogen-Air Detonation Loads and Their Numerical Simulation. Proc. 20th Int. Symp. on Shock Waves, Pasadena, CA, USA, pp 405, 1995.

Cariteau, B., and I. Tkatschenko. 2012. "Experimental Study of the Concentration Build-up Regimes in an Enclosure without Ventilation." International Journal of Hydrogen Energy 37(22):17400–408. Retrieved January 7, 2015 (http://linkinghub.elsevier.com/retrieve/pii/S036031991200804X).

Cariteau, B., and I. Tkatschenko. 2013. "Experimental Study of the Effects of Vent Geometry on the Dispersion of a Buoyant Gas in a Small Enclosure." International Journal of Hydrogen Energy 38(19):8030–38. Retrieved May 5, 2014 (http://linkinghub.elsevier.com/retrieve/pii/S0360319913007404).

Giannissi, SG et al. 2015. "CFD Benchmark on Hydrogen Release and Dispersion in Confined, Naturally Ventilated Space with One Vent." International Journal of Hydrogen Energy. Retrieved January 6, 2015 (http://www.sciencedirect.com/science/article/pii/S0360319914033485).

Hanna, SR. 1989. "Confidence Limits for Air Quality Model Evaluations, as Estimated by Bootstrap and Jackknife Resampling Methods." Atmospheric Environment (1967). Retrieved January 7, 2015 (http://www.sciencedirect.com/science/article/pii/0004698189901613).

Hanna, SR, JC Chang, and DG Strimaitis. 1993. "Hazardous Gas Model Evaluation with Field Observations." Atmospheric Environment. Part A. …. Retrieved January 7, 2015 (http://www.sciencedirect.com/science/article/pii/096016869390397H).

Launder B. and Spalding D. (1972), Lectures in mathematical models of turbulence. Academic Press, London, England. 1972.

Lilly D (1992), A proposed modification of the Germano subgrid-scale closure model. Physics of Fluids A: Fluid Dynamics 4. (1992): 633–635.

Molkov V. and Shentsov V. (2014), Numerical and physical requirements to simulation of gas release and dispersion in an enclosure with one vent. Int. J. of Hydrogen Energy, v.39 (35), pp. 13328-13345, doi:10.1016/j.ijhydene.2014.06.154

Petersen H. (1970), The properties of helium: density, specific heats, viscosity, and thermal conductivity at pressures from 1 to 100 bar and from room temperature to about 1800 K. Denmark 1970. Forskningscenter Risoe. Risoe-R, no. 224.

Reynolds O (1883),. An experimental investigation of the circumstances which determine whether the motion of water shall be direct or sinuous, and of the law of resistance in parallel channels. Proceedings of the royal society of London, vol. 35, no. 224–226, pp. 84–99, 1883.

Smagorinsky J. (1963), General circulation experiments with the primitive equations. I. The Basic Experiment. Month. Wea. Rev. 91.3 (1963): 99–164.

SUSANA (SUpport to SAfety ANalysis of Hydrogen and Fuel Cell Technologies), Guide to best practices in numerical simulations, 2015.

Versteeg, HK, and W. Malalasekera. 2007. An Introduction to Computational Fluid Dynamics: The Finite Volume Method. Retrieved November 13, 2014 (http://www.mie.utoronto.ca/labs/mussl/cfd20.pdf).

2.2 GARAGE_SBEP experiment

2.2.1 Experimental facility

The GARAGE facility is representative of a realistic single vehicle private garage. During the experiments, the GARAGE facility was situated indoors to attenuate the effect of the meteorological conditions on the simulation results. The interior dimensions of the facility are 5.76 m (length) x 2.96 m (width) x 2.42 m (height). The internal volume of GARAGE is 40.92 m^3 as represented in Figure 2-14.

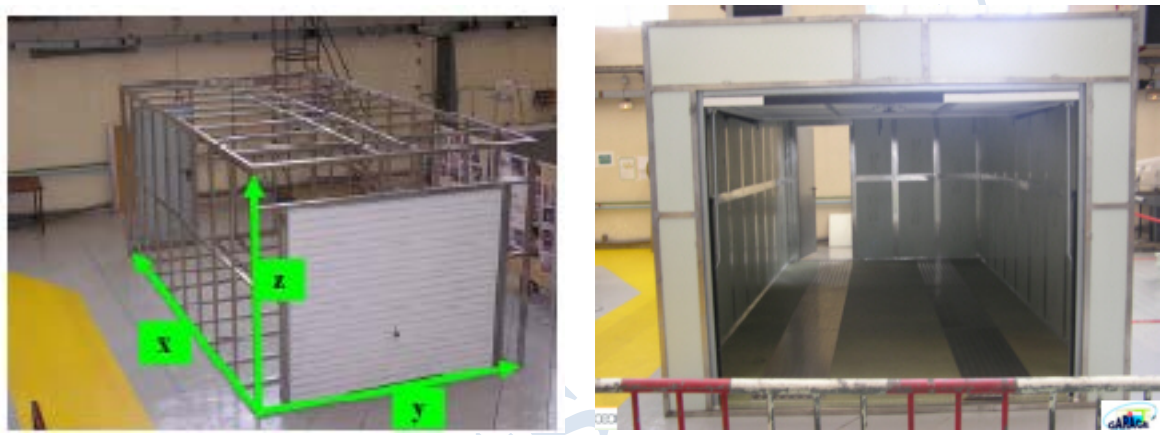

Figure 2-14. GARAGE set-up at CEA Saclay, Left: structural steel skeleton and Right: interior of the facility with the panels.

The parameters related to the test simulated with the CFD code are reported in Table 2-6.

Table 2-6. Experiment parameters.

Garage x-dimension (mm)	5760
Garage y-dimension (mm)	2960
Garage z-dimension (mm)	2420
x release (mm)	-2880
y release (mm)	1480
z release (mm)	220
Exit diameter (mm)	29,7
Volumetric flow rate - STP (NL/min)	18
He mass flow rate (g/s)	0,054
Garage Temperature T (°C)	24,1
Exit velocity (m/s)	0,47
Release Direction	Upwards
Release Type	Continuous
Release duration (s)	3740
Released volume - STP (NL)	1122

He released mass (gr)	200,28
Target concentration (%)	2,94%
Total measurement time (s)	90440

The test was performed without ventilation. The upper vent was kept closed. The lower vent was kept open in order to maintain the test facility at constant atmospheric pressure for the duration of the tests.

Concentrations were measured using mini-catharometers at 57 positions within the garage (see Figure 2-15).

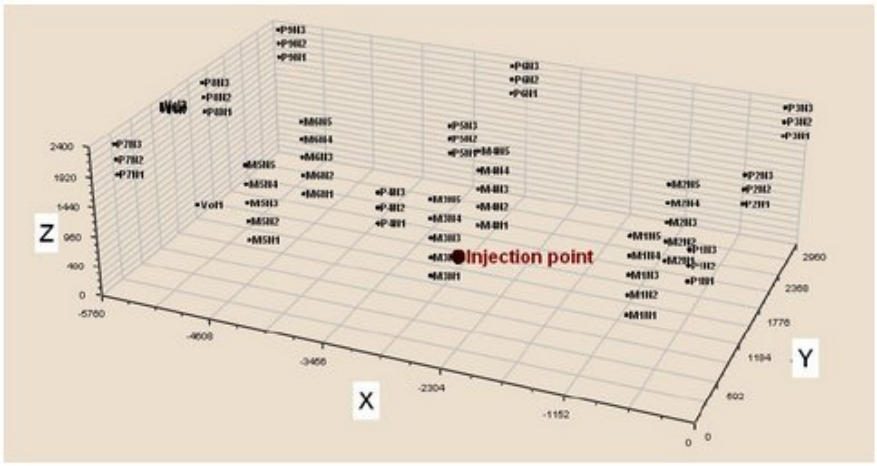

Figure 2-15. Sensor locations.

Table 2-7 presents the coordinates of the sensors of masts M1 and P1.3.

Table 2-7. Sensor coordinates.

Sensor name	x (mm)	y (mm)	z (mm)
M1N1	-1000	1001	315
M1N2	-1000	1001	630
M1N3	-1000	1002	945
M1N4	-1000	1000	1260
M1N5	-1000	995	1575
P1N1	-190	155	1900
P1N2	-190	151	2135
P1N3	-190	150	2370

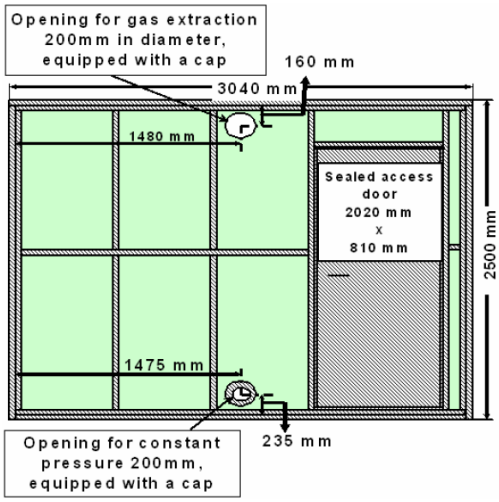

Figure 2-16. Openings (upper vent closed, lower vent open).

2.2.1.1 Sealing efficiency

The leakage rate from the fully sealed garage has been separately estimated to be 0.01 ACH, see Gupta et al. (2007).

2.2.1.2 Experimental results

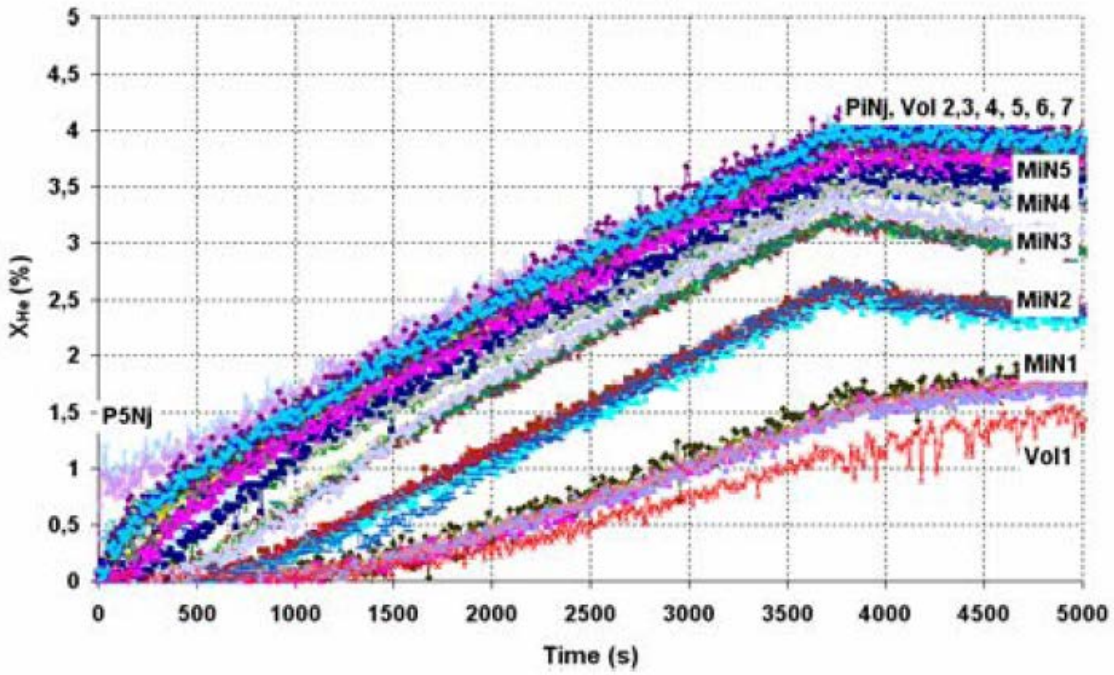

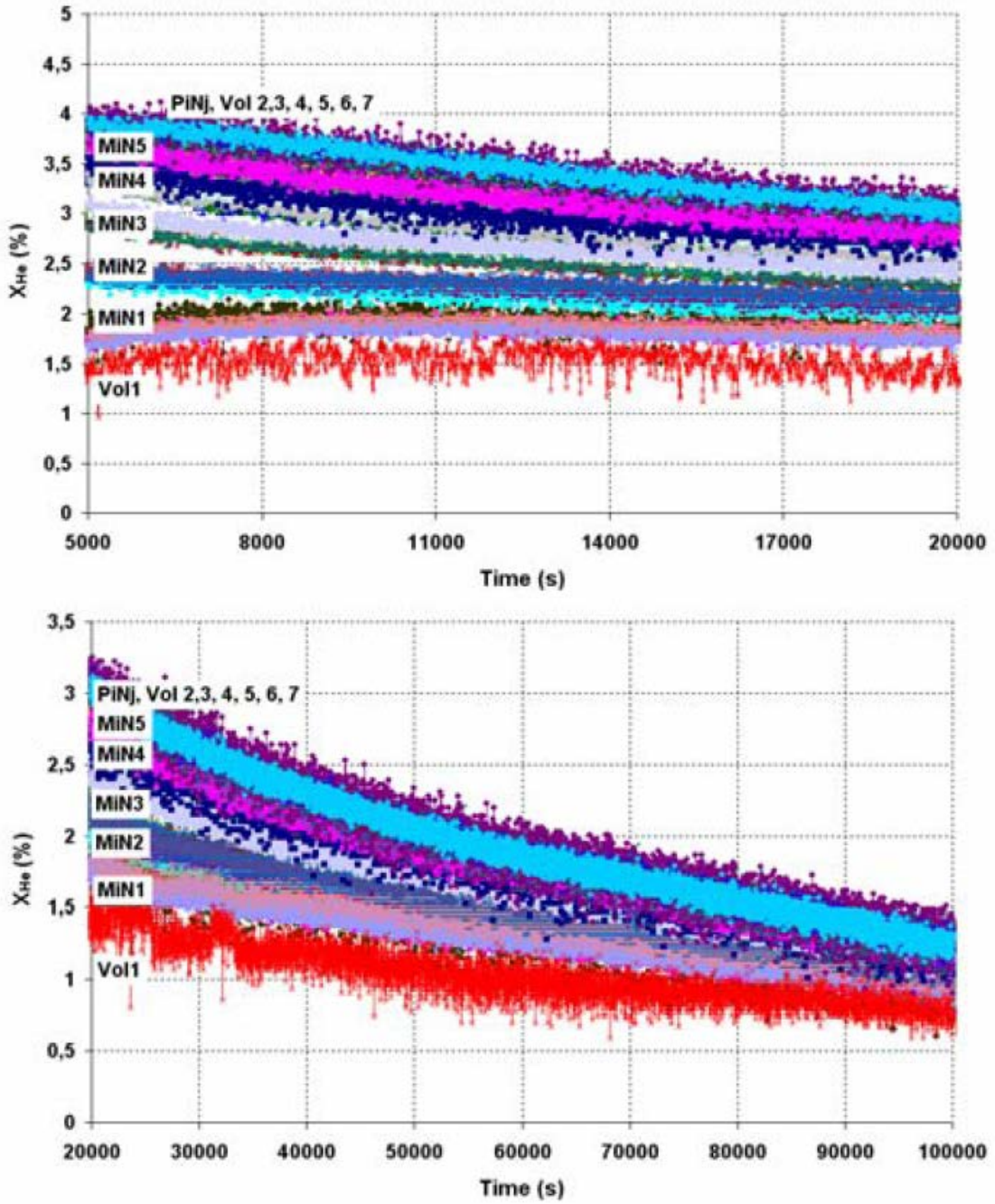

Figure 2-17. Measured Evolution of helium concentration (XHe) with time inside the GARAGE

2.2.2 HSL modeling

These simulations were performed in 2011. Since then, research has shown that the use of tetrahedral meshes for stably stratified problems such as this can lead to numerical errors. Whereas conventional wisdom would indicate that tetrahedral meshes would lead to excessive numerical diffusion, the opposite actually occurs and the numerical errors lead to an over-prediction of the stratification. These simulations are included to highlight this problem in comparison to the simulations reported in Section 2.2.3.

2.2.2.1 Governing equations

Helium dispersion is modelled using the unsteady Navier-Stokes equations together with the total energy equation and Menter's shear stress transport (SST) turbulence model. This turbulence model included the effect of buoyancy on the production and destruction of turbulent kinetic energy.

2.2.2.2 Simulation approach

The computational domain was built using the dimensions given in Table 2-6 and is shown in Figure 2-18. The domain is meshed using a hybrid mesh consisting of prismatic cells on the walls and tetrahedral cells away from the surface layers. Two meshes are constructed, with characteristics given in Table 2-8.
The walls and release pipe are set with smooth no-slip conditions with a constant temperature of 10 ^{o}C. The vent was set as an opening with a relative pressure of zero to allow flow in or out of the domain. The total simulation time is 12,000 s with helium being injected for the first 3740 s. The helium injection mass flow rate is specified in Table 2-5.

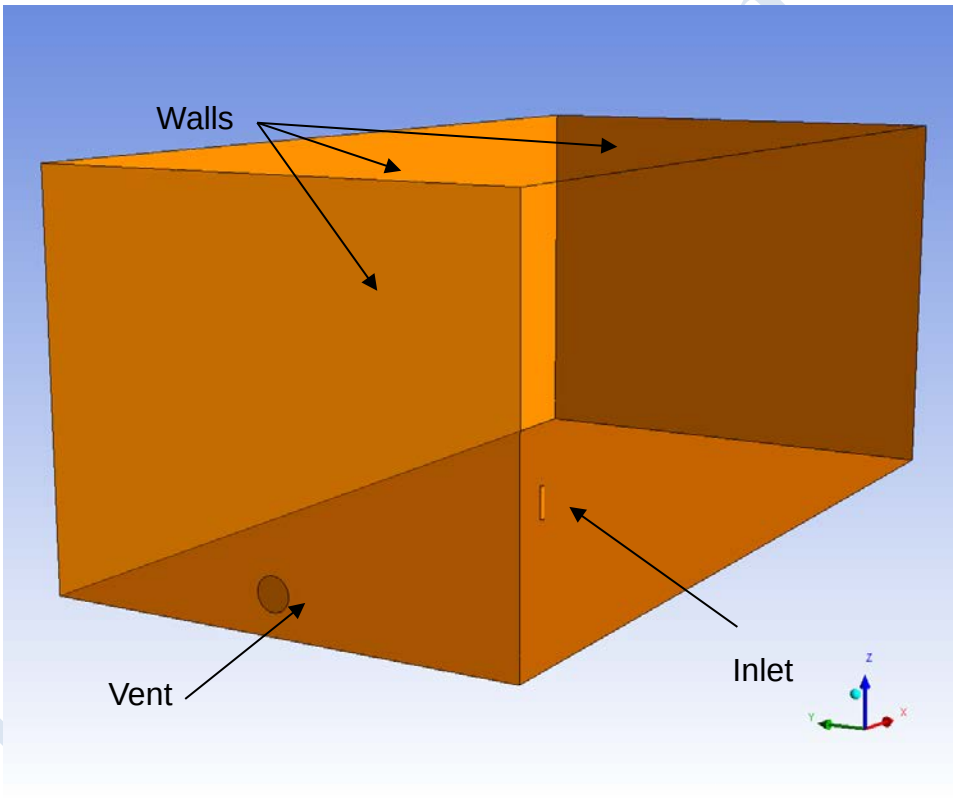

Figure 2-18. Computational domain.

Table 2-8. Details of the meshes used.

	Mesh 1	**Mesh 2**
number of elements	387,257	458,808

2.2.2.3 Numerical details

The details of the numerical simulation are as follows:

- Code: CFX 12.1

- SST turbulence model
- Finite volume solver
- High order scheme for convective terms
- Second order backward Euler for transient terms
- 0.5 s time step.

2.2.2.4 Results and discussion

Results for the simulations for the two meshes are plotted in Figure 2-19. Here, sensors are grouped according to the respective height within the domain. The dashed line in each plot indicates the high resolution CFD results. Generally speaking the results from the different meshes agree well with only minor difference on the lower sensors.

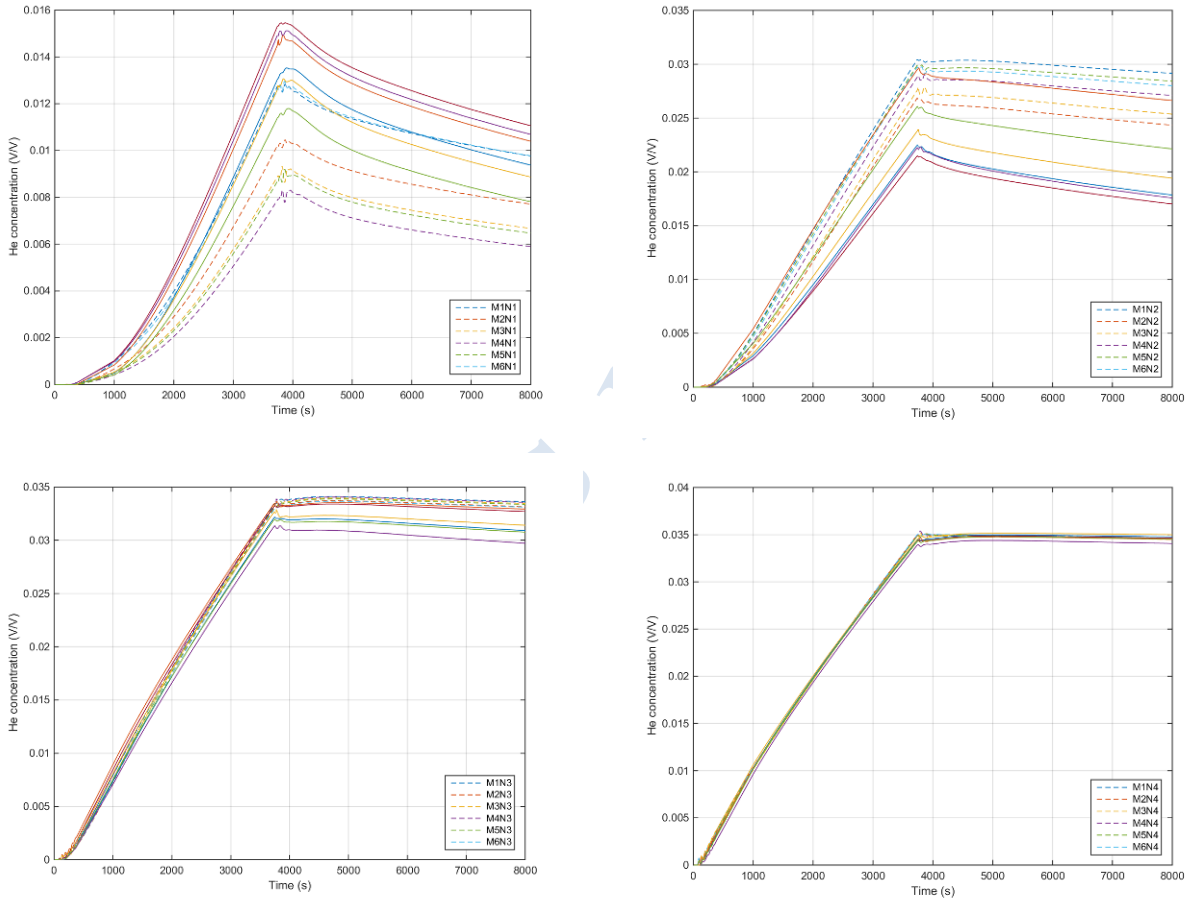

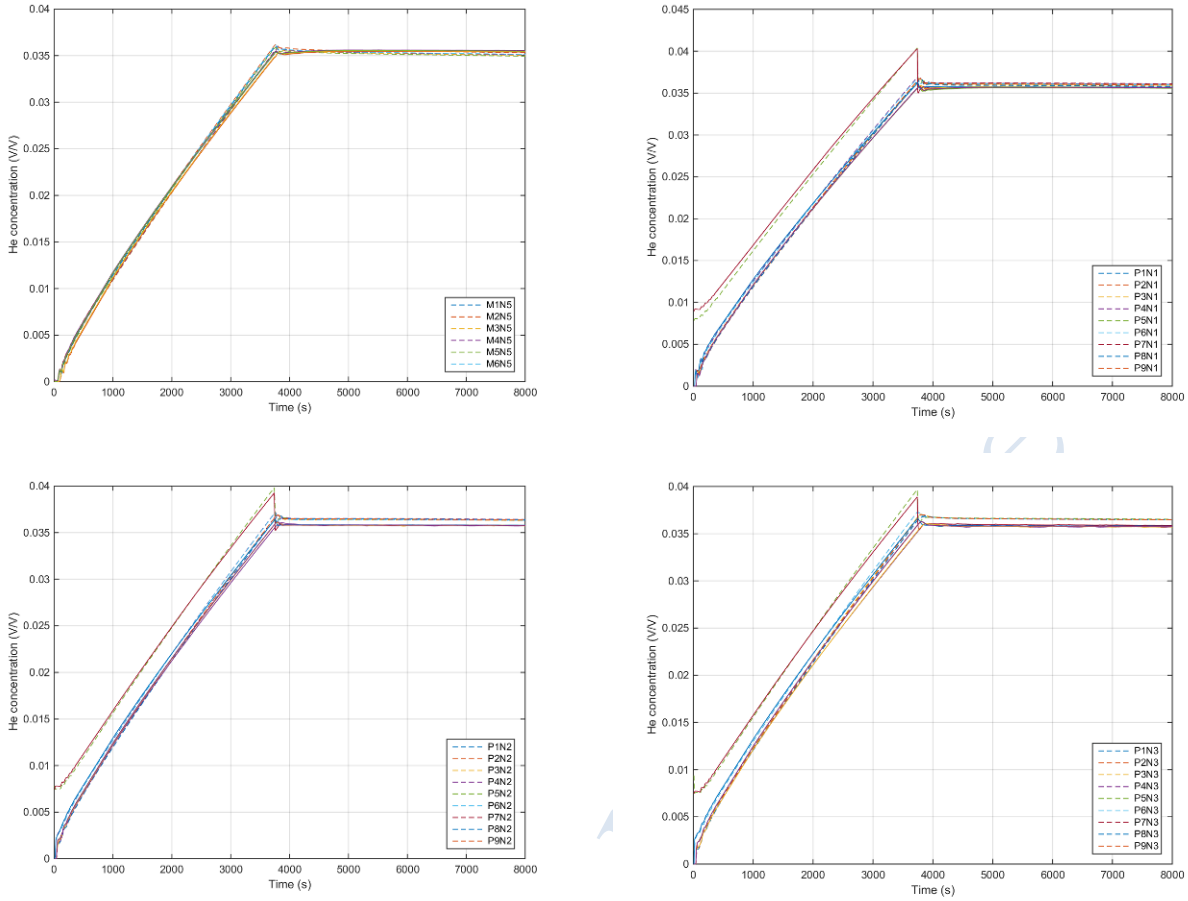

Figure 2-19. Results for the two mesh densities – fine mesh shown with dashed lines and coarse mesh shown with solid lines.

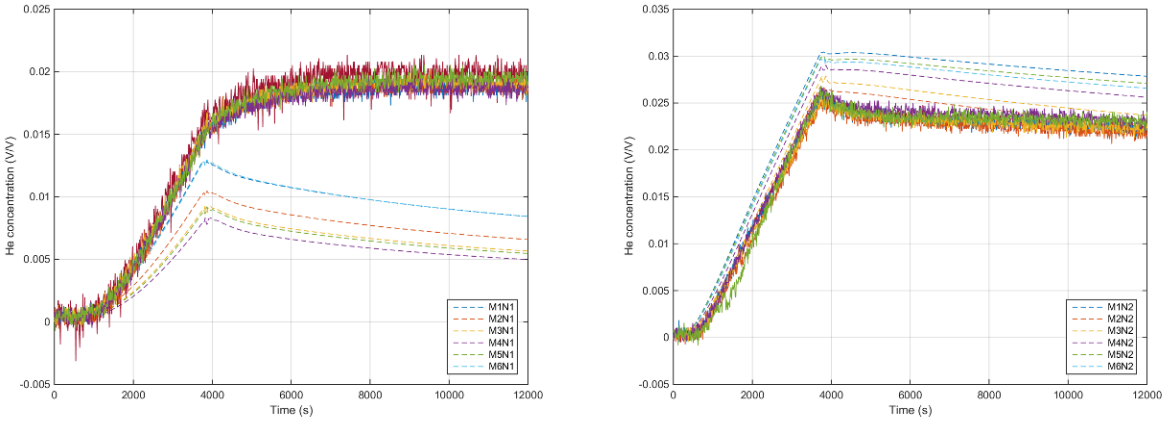

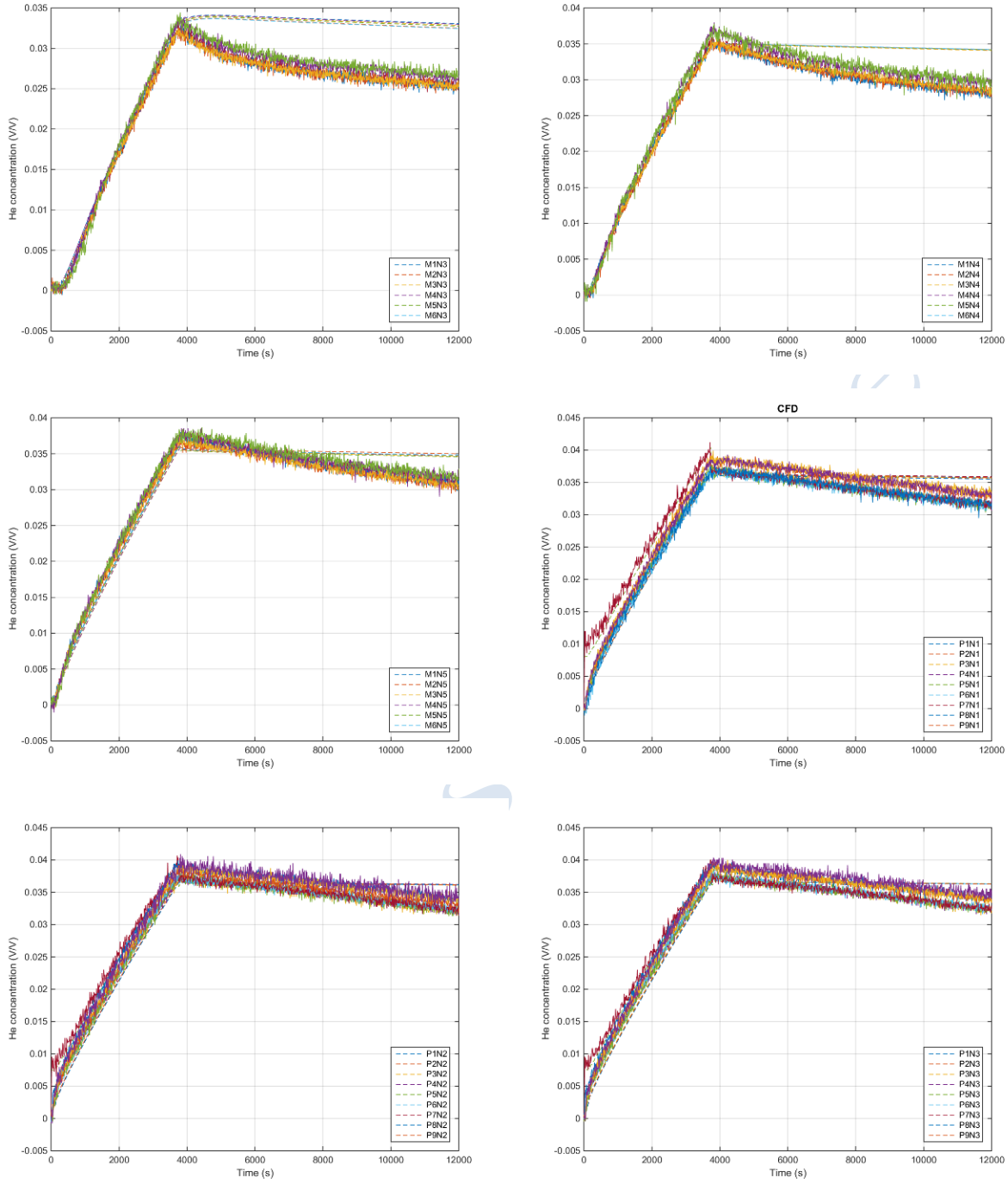

Figure 2-20. Comparison of experimental and CFD results grouped according to sensor height. Dash lines in each case indicate the CFD Simulations.

Sensors near the top of the domain exhibit a sharp drop in concentration as soon as the release is switched off. On the whole, the finer mesh appears to predict increased stratification. Figure 2-20 shows the CFD results plotted against the experiments. In the period when the helium is being injected, both the CFD predictions and experiments exhibit similar behaviour. Once the release is switched off, the experimental data show continued mixing as the concentration at the lower sensors increases. The CFD results do not show this behaviour and

appear to show increased stratification as time continues. Studies of similar flows at HSL have found that the tetrahedral mesh can lead to the prediction of unphysical stratification and the problem can be resolved by using a structured mesh aligned with the geometry.

2.2.2.5 Conclusions

The SBEP V21 problem was simulated using CFX using a tetrahedral mesh encompassing only the interior of the garage. Simulation results were in good qualitative agreement with the experiment during the filling stage. Once the jet was switched off, the experimental results showed continued mixing, but this was not replicated in the CFD model. The model results appear to show increased stratification with time, which we now believe to be due to the use of a mesh that is not aligned to be perpendicular to the gravity vector.

2.2.3 JRC modelling

2.2.3.1 Modelling strategy

The main parameters of the CFD simulations are:

- CFD code: ANSYS CFX 15.0
- Isothermal simulation.
- Source modelled as a 3D pipe or velocity profile imposed.
- Multicomponent flow model: the code assumes that the various components of a fluid are mixed at the molecular level and that they share the same mean velocity, pressure and temperature fields, and that mass transfer takes place by convection and diffusion.
- The computational domain extended beyond the garage by a box of dimensions 2 m × 3 m × 3 m in the X, Y and Z.
- Simulation with:
  - laminar model.
  - SST model Transitional model as fluid model*:* The k-ω based Shear-Stress-Transport (SST) model was originally designed to give highly accurate predictions of the onset and the amount of flow separation under adverse pressure gradients by the inclusion of transport effects into the formulation of the eddy-viscosity. This results in a major improvement in terms of flow separation predictions but not only. The full transition model is based on two transport equations, one for the intermittency and one for the transition onset criteria in terms of momentum thickness Reynolds number. It is called 'Gamma Theta Model' and it is the recommended transition model for general-purpose applications. It uses a new empirical correlation (Langtry and Menter) which has been developed to cover standard bypass transition as well as flows in low free-stream turbulence environments. This built-in correlation has been extensively validated together with the SST turbulence model for a wide range of transitional flows.
- Advection scheme: High resolution.
- Transient scheme: Second order backward Euler.

2.2.3.2 Mesh description

- Hybrid meshes: hexahedral and tetrahedral computational cells
- Grid refinement in selected zones of domain
- 1251 nodes on the source half plane in both meshes

- Mesh A: ~460k nodes (tetra mesh in the jet release zone and on top)
- Mesh B: ~550k nodes (tetra mesh in the jet release zone) see Figure 2-21

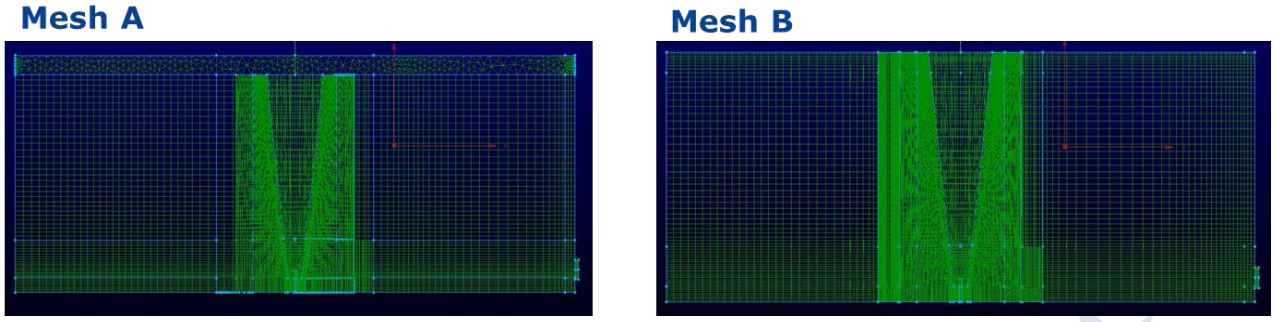

Figure 2-21. Mesh typology.

2.2.3.3 Results

The comparisons of the CFD molar concentration at some selected sensors (i.e. from m1n1 until m1n5 and from p1n1 to p1n3) and for two different cases are reported in Figure 2-22 and Figure 2-23; in particular in the following two figures are reported:

- black line: experimental data
- blue line: laminar simulation using the mesh B (see Figure 2-21) and imposing the mass flow rate at the nozzle
- red line: laminar simulation using the mesh A (see Figure 2-21) and imposing the velocity profile at the nozzle

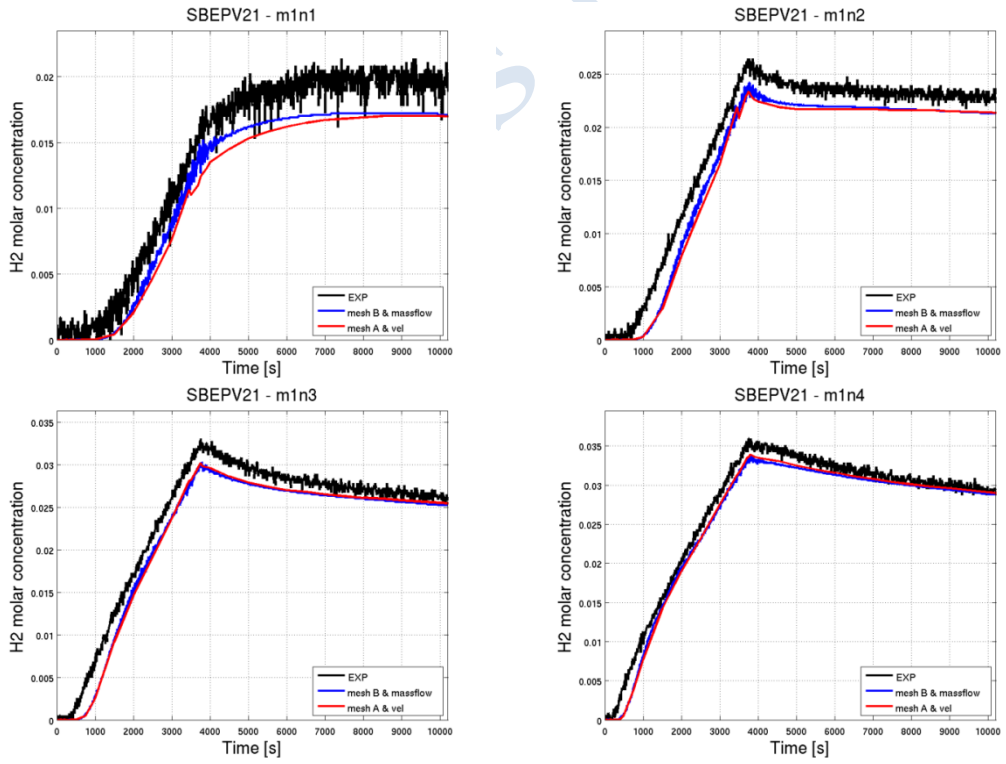

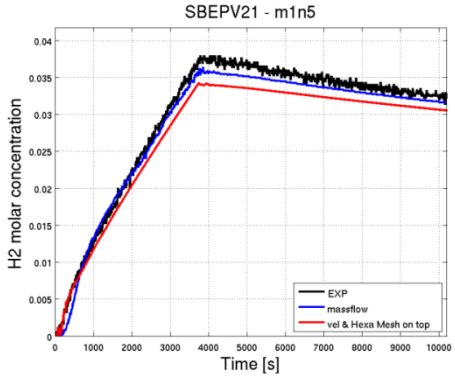

Figure 2-22. Concentration at sensors m1n1 – m1n5; mesh A vs. mesh B. Laminar model.

The two CFD models produce roughly the same results: in the lower part of the facility (i.e. sensors m1n1 – m1n5) they slightly under-predict the molar mass concentration, while in the upper part of the facility (i.e. sensors p1n1 – p1n3) they slightly over-predict the experimental data values.

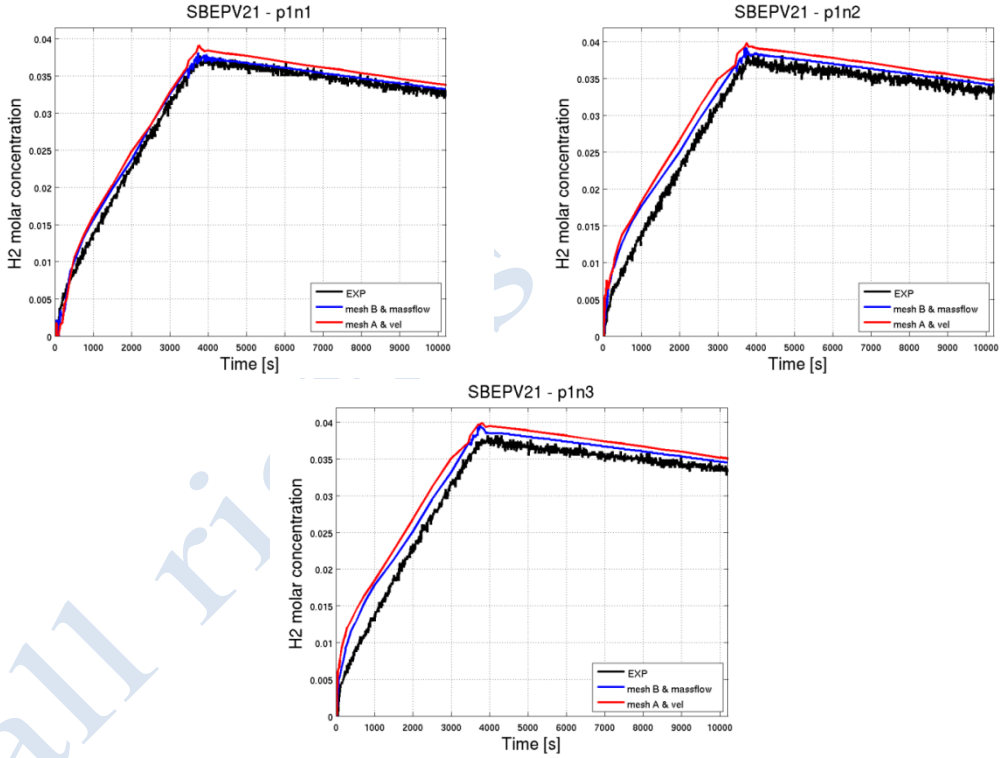

Figure 2-23. Concentration at sensors p1n1 – p1n3; mesh A vs. mesh B. Laminar model.

In Figure 2-24 and in Figure 2-25 the comparison among the experimental data and two different CFD models are reported:

- black line: experimental data
- blue line: laminar model and imposing the mass flow rate at the nozzle
- red line: SST transitional and imposing the mass flow rate at the nozzle

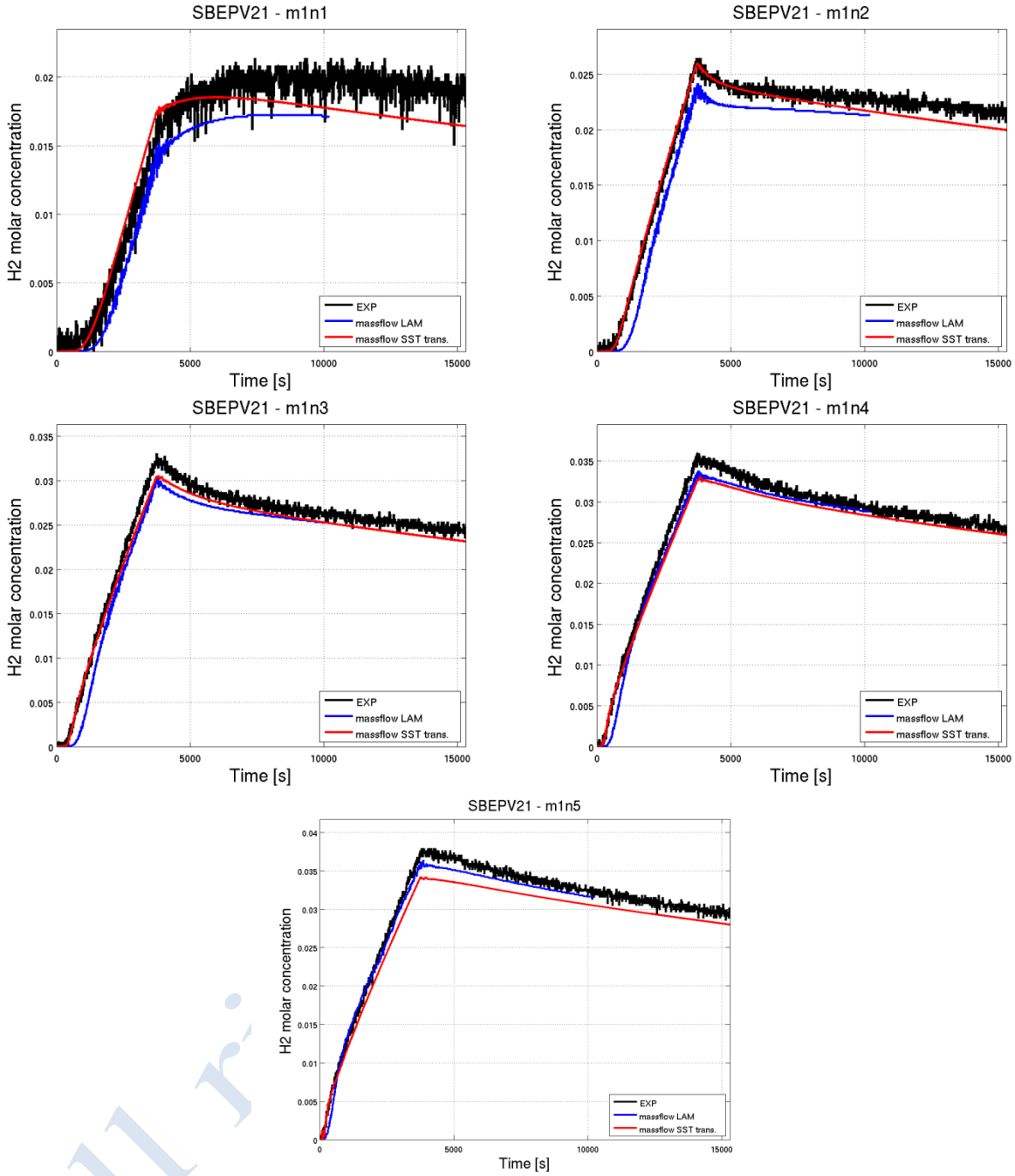

Figure 2-24. Concentration at sensors m1n1 – m1n5; laminar vs. SST transitional model.

Both the laminar and the SST model slightly under-predict the molar mass concentration in the lower part of the facility (i.e. sensors m1n1 – m1n5), while in the upper part of the facility (i.e. sensors p1n1 – p1n3) the laminar model slightly over-predict the experimental data values and the SST model slightly under-predict them.

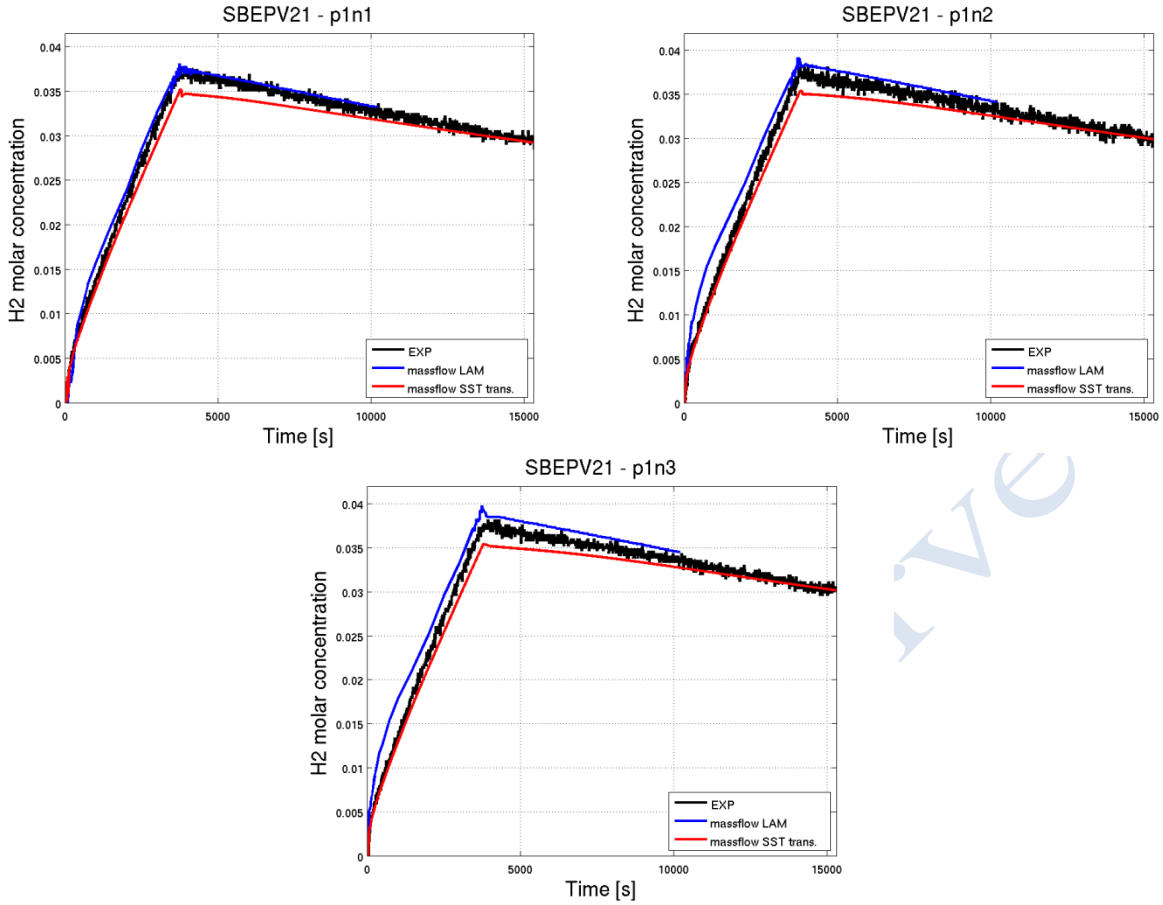

Figure 2-25: Concentration at sensors p1n1 – p1n3; laminar vs. SST transitional model.

2.2.3.4 Conclusions

The CFX code was used by JRC to reproduce the SBEP21 with a general good agreement between experimental measurements and simulation results. Both the laminar and the SST model slightly under-predict the molar mass concentration in the lower part of the facility, while in the upper part of the facility the laminar model slightly over-predict the experimental data values and the SST model slightly under-predict them.

2.2.4 Overall conclusions

For the release and dispersion benchmarking exercise the Standard Benchmark Exercise Problem (SBEP) V21 was chosen and simulated by JRC and HSL. The experiment involves helium release inside a garage like facility with one vehicle.

In JRC calculations, overall good agreement was found between the predictions and the experiment. Both laminar model and SST transitional turbulence model produced good results. However, both models tend to slightly under-predict the concentration in the lower part of the enclosure, while in the upper part the laminar model slightly over-predict the concentration and the SST model slightly under-predict it.

In HSL calculations, simulation results were in good qualitative agreement with the experiment during the filling stage. Once the jet was switched off, the experimental results showed continued mixing, but this was not replicated in the CFD model. The model results

appear to show increased unphysical stratification with time. That effect is probably linked to the use of the unstructured mesh.

2.2.5 References

Cariteau, B., 2007, HYSAFE deliverable D65, Experimental results on helium release inside a full scale GARAGE set-up, CEA

Gupta S., Brinster, J., Studer, E., Tkatschenko, I., 2007, Hydrogen Related Risks Within a Private Garage: Concentration Measurements In a Realistic Full Scale Experimental Facility, ICHS-2, San Sebastian,

Venetsanos A.G. et al, 2010, HYSAFE, SBEP-V21 He release and dispersion in a realistic full scale experimental facility.

3. Ignition Benchmark

3.1 Spontaneous ignition experiment

3.1.1 Experimental description

Experimental research on spontaneous ignition had been conducted by Golub et al. (2010). The hydrogen was released from a high pressure system into a channel ending in a T-shaped nozzle mimicking Pressure Relief Device (PRD). The geometry of a high-pressure system and T-shaped channel were taken Golub et al. (2010).

The high-pressure system consisted of a 210 mm long tube with 16 mm internal diameter (ID) followed by a 280 mm long tube with 10 mm ID at the end of which a flat burst disk, made of a soft metal with cuts to facilitate failure. On the other side of the burst disk is a simulated PRD open to atmosphere Figure 3-1. The PRD has a 48 mm long axial channel of 6.5 mm ID with a flat end, and two radial channels on opposite sides of the axial channel to vent hydrogen to atmosphere. Each radial channel has 6.25 mm length and 4 mm ID (distance from the end connected to the atmosphere of one radial channel to the end of another is 19 mm). Radial channels are flush with the axial channel end wall and positioned so that the edge of each side channel touches tangentially the flat end wall of the axial channel. The burst disk opening time was estimated as about 10 μs (Golub et al., 2010). To register spontaneous ignition a light sensor was installed along the axis of radial channels of the PRD.

Golub et al. (2010) stated that the light sensor did not record any signal when the initial pressure in high-pressure chamber was below 1.2 MPa, and record positive signal when the pressure was 2.9 MPa. Private communication (Golub, 2010) indicated that the ignition was also observed at pressure 2.43 MPa.

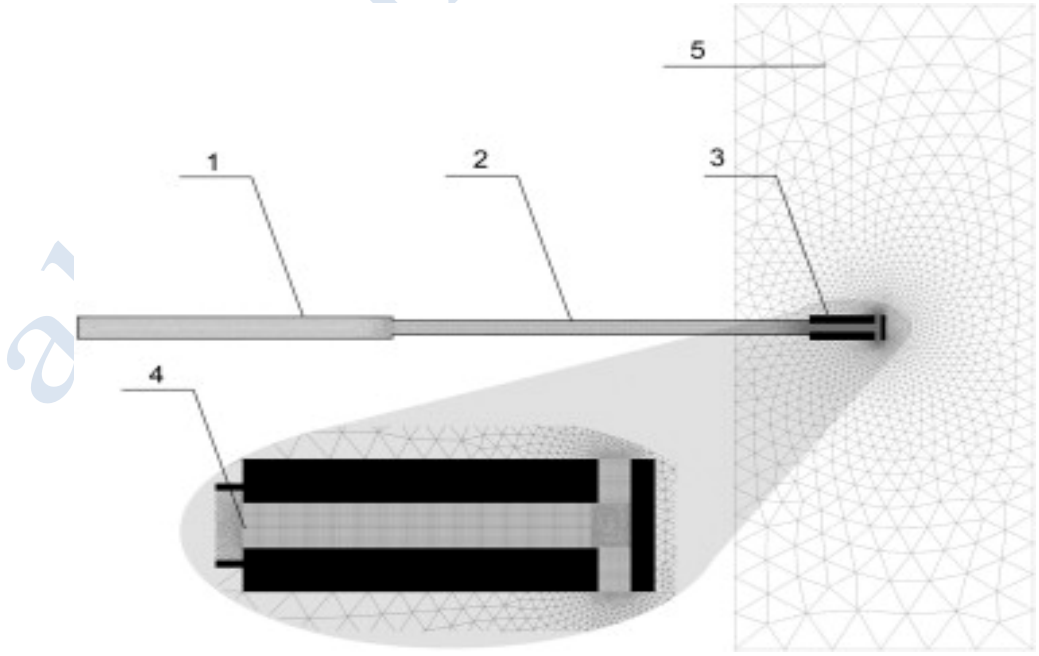

Figure 3-1. The geometry and computational domain: 1 and 2 – high-pressure tubes, 3 – PRD, 4 – burst disk, and 5 – external domain (Bragin et al., 2013).

3.1.2 UU modelling

3.1.2.1 Mathematical methodology

Governing equations

Simulation of spontaneous ignition employed Large Eddy Simulation (LES) approach with a set of filtered three-dimensional compressible equations for conservation of mass, momentum (Navier-Stokes), energy and species serving as governing equations.

Renormalization group (RNG) theory (Yakhot and Orszag, 1986) is used to calculate the effective viscosity μ_{eff} as

$$\mu_{eff} = \mu\left[1 + H\left(\mu_s^2\ \mu_{eff} / \mu^3 - 100\right)\right]^{1/3},$$

where $\mu_s = \overline{\rho}\left(C_{RNG}\ V_{CV}^{1/3}\right)^2 \sqrt{2\widetilde{S}_{ij}\widetilde{S}_{ij}}$ and $H(x)$ is Heaviside function.

The effective Prandtl and Schmidt numbers are calculated following the RNG theory by purely theoretical equations (Yakhot and Orszak, 1986)

$$\left|\frac{1/N_{eff} - 1.3929}{1/N - 1.3929}\right|^{0.6321} \left|\frac{1/N_{eff} + 2.3929}{1/N + 2.3929}\right|^{0.3679} = \frac{\mu}{\mu_{eff}},$$

where N stands for laminar Prandtl or Schmidt numbers. Laminar Prandtl and Schmidt numbers are calculated according to kinetic theory.

Combustion model

Hydrogen spontaneous ignition simulation used EDC model (Magnussen, 1981) with updates incorporating detailed Arrhenius chemical kinetics in turbulent flames as the combustion sub-model. EDC model expression for a combustion rate is based on an assumption that chemical reactions occur in the small scale structures on the Kolmogorov's scale where the dissipation of turbulence energy takes place.

In the EDC model adopted in FLUENT code a source term in the species transport equation is modelled as

$$R_m = \frac{\rho\left(\xi^*\right)^2}{\tau^*\left[1 - \left(\xi^*\right)^3\right]}\left(Y_m^* - Y_m\right),$$

where R_m is a net rate of production of specie m by chemical reactions, ξ^* is the length fraction of the fine scale turbulent structures where the reaction occurs, Y_m^* is the fine scale species mass fraction (specie m) after reacting over the time τ^*, Y_m is a species mass fraction for specie m in the surrounding fine scales state. The multiplier with a square of the length fraction of fine scales represents the mass exchange between the surrounding and fine structure regions. The length fraction of fine structures is evaluated in this LES model similar to EDC RANS model as

$$\xi^* = C_\xi u_\eta / u_{SGS},$$

where the volume fraction constant is taken as C_ξ = 2.1377 similar to RANS. The upper limit ξ^* = 1 is applied when the fine scales velocity is larger than residual SGS velocity.

The scale of a LES residual velocity at the sub-grid scale (SGS) level is

$u_{SGS} = \mu_t / (\rho \cdot L_{SGS})$,
where μ_t is turbulent viscosity, and the SGS length scale is determined as

$L_{SGS} = C_{RNG} V^{1/3}$.
The Kolmogorov's velocity u_η is

$$u_\eta = \left(\frac{\mu \cdot u_{SGS}^3}{\rho \cdot L_{SGS}} \right)^{1/4},$$
where μ is laminar viscosity.

Characteristic sub-grid eddy and Kolmogorov's timescales are respectively

$\tau_{SGS} = L_{SGS} / u_{SGS}$, and

$$\tau_\eta = \left(\frac{\mu \cdot L_{SGS}}{\rho \cdot u_{SGS}^3} \right)^{1/2}.$$

The volume fraction of the fine scales is calculated as ξ^{*3} and species are assumed to react in the fine structures over a time scale

$\tau^* = C_\tau \tau_\eta$,
where a time scale constant is taken equal to C_τ = 0.4082 similar to applied in the EDC RANS model.

Magnussen (Magnussen, 1989) model assumes that all the fine scales in the cell are perfectly stirred reactors with a residence time τ^*. Combustion at the fine scales is assumed in this model to take place as a constant-pressure reactor. The reactor type is determined by the choice of a mixing rate $1/\tau^*$ and a time-step Δt. In FLUENT initial conditions at the constant pressure reactor are taken as the current species and temperature in the cell. Arrhenius reactions governed by the following equation proceed over the time scale τ^*.

All of the reactions considered in the chemical mechanism involved are elementary (reversible). For reversible reaction the molar rate of creation or destruction of species *i* in reaction *r* is given by

$$\hat{R}_{m,R} = \Gamma \left(\nu''_{m,r} - \nu'_{m,r} \right) \left(k_{f,r} \prod_{n=1}^{N} \left[C_{n,r} \right]^{\nu'_{m,r}} - k_{b,r} \prod_{n=1}^{N} \left[C_{n,r} \right]^{\nu''_{m,r}} \right),$$
where *N* is number of chemical species in the system; $\nu'_{m,r}$ is stoichiometric coefficient for reactant *m* in reaction *r*; $\nu''_{m,r}$ is stoichiometric coefficient for product *m* in reaction *r*; $k_{f,r}$ is forward rate constant for reaction *r*; $k_{b,r}$ is backward rate constant for reaction *r*. Γ represents the net effect of third bodies on the reaction rate and is given by

$$\Gamma = \sum_{n=1}^{N} \gamma_{n,r} C_n,$$
where $\gamma_{m,r}$ is the third-body efficiency of *m*-th species in the *r*-th reaction.

The forward rate constant for reaction *r* without pressure dependency is computed in conventional form of Arrhenius equation

$k_{f,r} = AT^{\beta_r} \exp(-E_r / RT)$.

All reactions are reversible, with the backward rate constant for reaction *r* calculated from the forward rate and the equilibrium constant K_r using the equation

$k_{b,r} = k_{f,r} / K_r$.

The equilibrium constant K_r is computed as

$$K_r = \exp\left(\frac{\Delta S_r^0}{R} - \frac{\Delta H_r^0}{RT}\right) \cdot \left(\frac{P_{atm}}{RT}\right)^{\sum_{i=1}^{N}\left(\nu''_{m,r} - \nu'_{m,r}\right)},$$

where P_{atm} denotes atmospheric pressure (101,325 kPa). The term within the exponential function represents the change in Gibbs free energy and its components are computed as

$$\frac{\Delta S_r^0}{R} = \sum_{i=1}^{N}\left(\nu''_{m,r} - \nu'_{m,r}\right)\frac{S_m^0}{R},$$

$$\frac{\Delta H_r^0}{RT} = \sum_{i=1}^{N}\left(\nu''_{m,r} - \nu'_{m,r}\right)\frac{h_m^0}{RT},$$

where S_m^0 and h_m^0 are entropy and enthalpy respectively of the *m*-th species respectively evaluated at temperature *T* and atmospheric pressure.

Specific heats of mixtures were approximated as piecewise-polynomial functions of temperature with polynomial coefficients calculated according to mass-weighted mixing law.

Chemical reaction model

Simulation utilized the detailed 21-step chemical reaction mechanism of hydrogen combustion in air employing 37 elementary reactions (Gutheil et al, 1993). The specific reaction rate constants are given in Table 3-1. The forward reaction rate constants are presented in the table, and backward rates for reversible reactions are calculated through the equilibrium constants.

Table 3-1. Specific reaction rate constants (Gutheil et al., 1993).

No.	**Reactions**	***A*, KJ/mol**	***β*r,**	***E*r, mol/m^3**
1	H+O2=OH+O	2.00E+14	0.00	70.30
2	H2+O=OH+H	1.80E+10	1.00	36.93
3	H2O+O=OH+OH	5.90E+09	1.30	71.25
4	H2+OH=H2O+H	1.17E+09	1.30	15.17
5	H+O2+M=HO2+M	2.30E+18	-0.8	0.00
	Third-body chaperon efficiencies H2/1./ H2O/6.5/ O2/0.4/ N2/0.4/			
6	H+HO2=OH+OH	1.50E+14	0.00	4.20
7	H+HO2=H2+O2	2.50E+13	0.00	2.93
8	OH+HO2=H2O+O2	2.00E+13	0.00	4.18
9	H+H+M=H2+M	1.80E+18	-1.00	0.00

	Third-body chaperon efficiencies H2/1./ H2O/6.5/ O2/0.4/ N2/0.4/			
10	H+OH+M=H2O+M	2.20E+22	-2.00	0.00
	Third-body chaperon efficiencies H2/1./ H2O/6.5/ O2/0.4/ N2/0.4/			
11	HO2+HO2=H2O2+O2	2.00E+12	0.00	0.00
12	H2O2+M=OH+OH+M	1.30E+17	0.00	190.38
13	H2O2+OH=H2O+HO2	1.E+13	0.00	7.53
14	O+HO2=OH+O2	2.E+13	0.00	0.00
15	H+HO2=O+H2O	5.E+12	0.00	5.90
16	H+O+M=OH+M	6.2E+16	-0.60	0.00
	Third-body chaperon efficiencies H2O:5, others 1			
17	O+O+M=O2+M	6.17E+15	-0.50	0.00
18	H2O2+H=H2O+OH	1.E+13	0.00	15.02
19	H2O2+H=HO2+H2	4.79E+13	0.00	33.26
20	O+OH+M=HO2+M	1.E+16	0.00	0.00
21	H2+O2=OH+OH	1.7E+13	0.00	200.0
	Nitrogen Chemistry			
22	O+N2=N+NO	1.82E+14	0.00	319.02
23	O+NO=N+O2	3.8E+09	1.00	173.11
24	H+NO=N+OH	2.63E+14	0.00	210.94
25	NO+M=N+O+M	3.98E+20	-1.50	627.65
26	N2+M=N+N+M	3.72E+21	-1.60	941.19
27	N2O+O=NO+NO	6.92E+13	0.00	111.41
28	N2O+O=N2+O2	1.E+14	0.00	117.23
29	N2O+N=N2+NO	1.E+13	0.00	83.14
30	N+HO2=NO+OH	1.E+13	0.00	8.31
31	N2O+H=N2+OH	7.6E+13	0.00	63.19
32	HNO+O=NO+OH	5.01E+11	0.50	8.31
33	HNO+OH=NO+H2O	1.26E+12	0.50	8.31
34	NO+HO2=HNO+O2	2.E+11	0.00	8.31
35	HNO+HO2=NO+H2O2	3.16E+11	0.50	8.31
36	HNO+H=NO+H2	1.26E+13	0.00	16.63

37	HNO+M=H+NO+M	1.78E+16	0.00	203.7

3.1.2.2 Simulation approach

Calculation domain

The axial and radial channels of the PRD were meshed with a hexahedral grid with a uniform control volume (CV) size of about 400 μm both along the axial channel and in its cross-section, excluding the intersection zone. The intersection area of the axial and the radial channels was meshed with tetrahedral CVs with size of about 200 μm, i.e. the largest CV size used in numerical simulations of the spontaneous ignition phenomenon up to date. This is due to the application of the LES technique requiring 3D domain and thus larger CV size to simulate a problem within reasonable computation time. The high-pressure chamber was meshed by tetrahedrons with the smallest CV size of about 250 μm clustered near the membrane of the PRD and rapidly increasing away from it reaching the maximum cell width of 10 mm at the far end. The total number of control volumes in the computational domain amounted to a moderate number of 417,685 cells.

Initial and Boundary Conditions

No-slip impermeable adiabatic boundary conditions were used on walls. Non-reflecting open "pressure-far-field" boundaries were implemented outside of the PRD. The high-pressure system was modelled as closed to exclude potential effects of inlet boundary conditions on the process. This assumption is justified because the observation time in simulation is less than a time required for rarefaction wave to reach the far end of the high-pressure system. Hydrogen initial pressure in the high-pressure system p0 = 1.5, 2.4 and 2.9 MPa. Initial temperature T0 = 300 K and the mole fraction of hydrogen equal to 1 were assumed in the high-pressure system before the burst disk rupture in all cases. Space within PRD and external area were filled with air (0.23 mass fraction of oxygen and 0.77 of nitrogen) at atmospheric conditions (p0 = 0.101 MPa and T0 = 300 K).

Burst disk opening

The non-instantaneous burst disk opening plays an important role in the process of ignition due to effect on mixing between hydrogen and air. The opening of a membrane was therefore approximated in simulations by a step-like process consecutive opening of 10 concentric sections (see Figure 3-2).

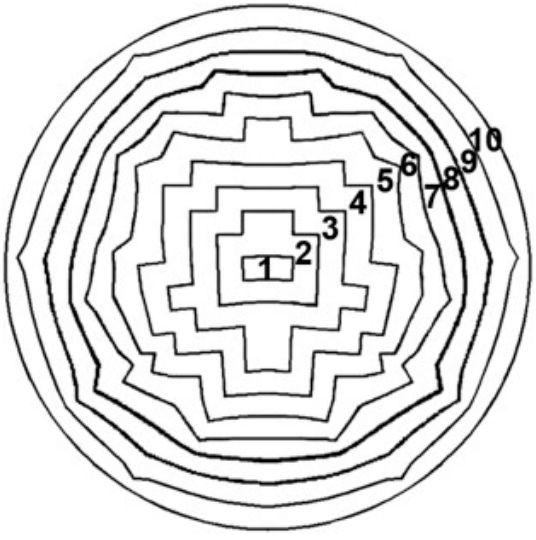

Figure 3-2. Step-like approximation of a burst disk rupture process: 1–10 are sections that open in series (Bragin et al., 2013).

Opening time of a diaphragm sections was calculated using Spence and Woods (1964) approach

$$t = k(\rho b d / p)^{1/2}$$

where ρ is the density of the diaphragm material, b and d are thickness and diameter of the diaphragm, respectively, and the values of k are found to be in a range 0.91–0.93 (Wen et al., 2009). Density of annealed copper was taken to be equal 8900 kg/m^3. Diaphragm sections opening times for various initial pressures are listed in Table 3-2.

Table 3-2. Opening time for diaphragm sections.

Initial pressure, MPa	Opening time, μs, for section									
	1	2	3	4	5	6	7	8	9	10
1.5	0	4.5	9	13.5	18	22.5	27	31.5	36	40.4
2.43	0	3.5	7.1	10.6	14.2	17.7	21.3	24.8	28.3	31.9
2.90	0	3.2	6.5	9.7	12.9	16.2	19.4	22.6	25.9	29.1

3.1.2.3 Numerical details

- Code: Numerical simulation was performed using Fluent 6.3 CFD software
- Discretisation: finite volume
- Solver type: coupled, density based solver
- Numerical scheme for convective terms: second order upwind AUSM flux splitting
- Transient numerical scheme: explicit time stepping
- In-Situ Adaptive Tabulation (ISAT) method (Pope, 1997) is used to reduce chemical reaction calculation time
- CFL number: 0.2

3.1.2.4 Results and Discussion

Numerical simulations were performed for initial hydrogen pressure 1.5 MPa and 2.9 MPa. For the case with 1.5 MPa initial pressure no auto-ignition was observed and hydrogen-air mixture temperature remained well below the combustion temperature (Figure 3-3, left). The absence of ignition is further confirmed by the absence of noticeable quantities of reaction products, such as hydroxyl OH (Figure 3-3, right).

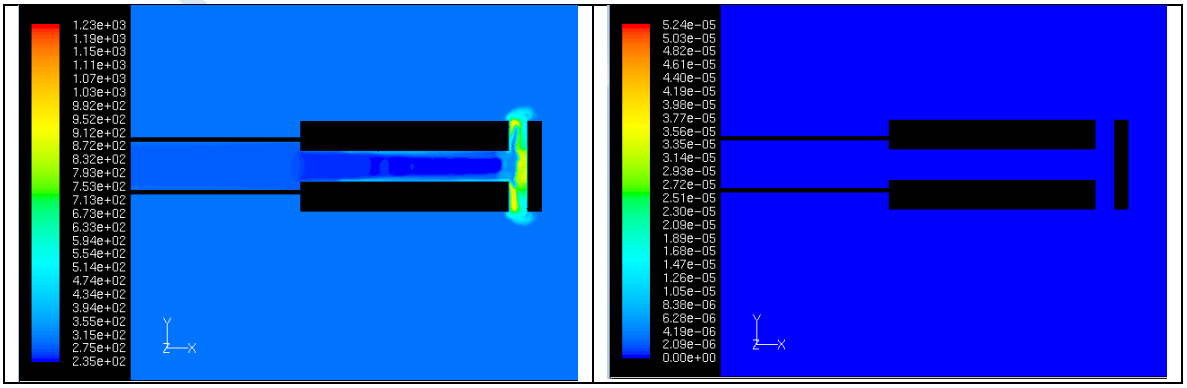

Figure 3-3. Temperature (left) and OH concentration (right) contours at the axis of the T-shaped PRD at t=7.46e-5 s for the case with 1.5 MPa initial pressure.

For the case with initial pressure 2.9 MPa, the ignition was observed at approximately 6.2e-5 second, after the secondary reflection of shock wave from the radial channels of T-shaped PRD (Figure 1.3-2, top). Observation of flow evolution (see movie) indicates that ignition occurs at the location of the leading shock wave secondary reflection. The first reflection occurs when the shock traveling along the axis of the channel reaches the closed off end of the PRD. At this time the ignition is not possible as the area still lacks hydrogen. Once the hydrogen flows around the edge from the axial into radial channels, it starts mixing with air heated by shocks, providing the necessary conditions for ignition of the mixture. It can be seen that for both initial pressures combustion is initiated in the radial channel in a location which is closer to the upstream wall. The fact of ignition and its location can be confirmed by sudden appearance of large quantities of hydroxyl OH at the same locations (Figure 3-4, bottom). These observations are in agreement with the experiment (Golub et al., 2010). Additional simulation at 2.4 MPa initial pressure indicated a tentative ignition in a significantly smaller region (detailed simulations reported in Bragin et al., 2013 indicate that it is self-extinguished within approximately 1e-5 s). More details on the simulation results are provided in Bragin et al., (2013).

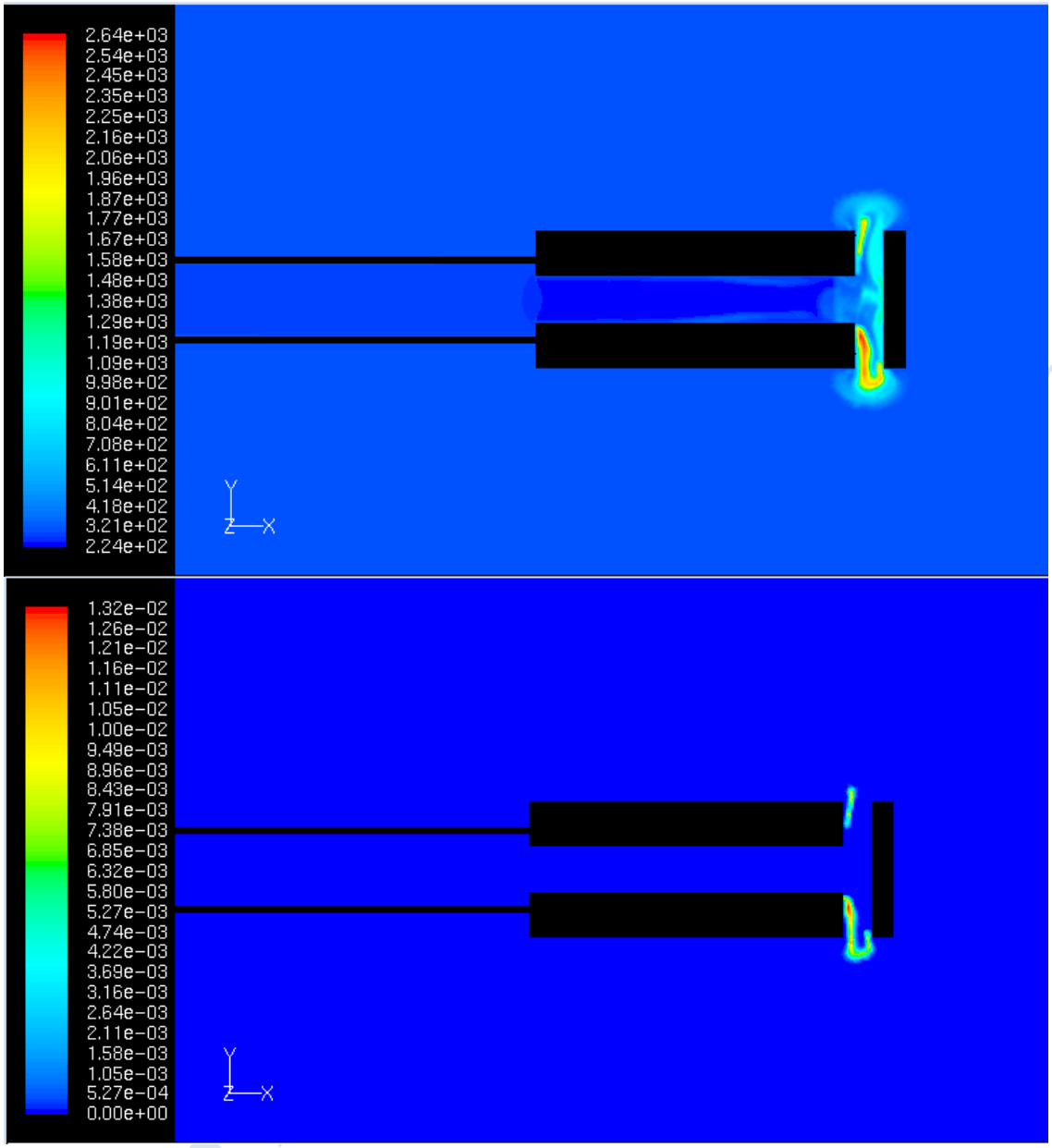

Figure 3-4. Temperature (top) and OH concentration (bottom) contours at the axis of the T-shaped PRD at t=6.65e-5 s for the case with 2.9 MPa initial pressure.

3.1.2.5 Conclusions

The LES model based on the eddy dissipation concept with detailed Arrhenius kinetics for modelling of SGS combustion, and renormalization group theory for modelling of SGS turbulence was applied to modelling of the hydrogen spontaneous ignition during release into the T-shaped channel. Gradual rupture of the flat burst disk was implement to simulate realistic process of PRD burst which affects the mixing process between heated by shock air and expanding hydrogen.

Numerical simulations predicted hydrogen autoignition at the release pressure of 2.9 MPa, while no ignition was observed for the release at 1.5 MPa, which matches the results of experiments.

3.1.3 References

Bragin M.V., Makarov D.M. and Movkov V.V. (2013), Pressure limit of hydrogen spontaneous ignition in a T-shaped channel, *Intl J of Hydrogen Energy*, 38 (2013): 8039-8052.

Golub V.V., Volodin V.V., Baklanov D.I., Golovastov S.V., Lenkevich D.A (2010)., Experimental investigation of hydrogen ignition at the discharge into channel filled with air, In: Physics of Extreme States of Matter, ISBN 978-5-901675-96-0, Chernogolovka, 2010: 110-113.

Golub V (2010), Private communication.

Gutheil E., Balakrishnan, G., Williams F. (1993), Structure and extinction of hydrogen-air diffusion flames, in N. Peters, B. Rogg (Eds.), Reduced kinetic mechanisms for applications in combustion systems, Springer-Verlag, New York (1993), p. 179

Magnussen B (1981), On the structure of turbulence and a generalized eddy dissipation concept for chemical reactions in turbulent flow. In: Proceedings of the 19th American Institute for Aeronautics and Astronautics Aerospace Science meeting, St. Louis; 12–15 January 1981.

Magnussen B (1989), Modelling of pollutant formation in gas turbine combustors based on the eddy dissipation concept. In: Proceedings of the CIMAC conference, Tianjin, China; 4–9 June, 1989.

Pope S. (1997), Computationally efficient implementation of combustion chemistry using in situ adaptive tabulation, *Combust Theory Model*, 1 (1997), pp. 41–63.

Spence D.A. and Woods B.A. (1964), A review of theoretical treatments of shock-tube attenuation, *J Fluid Mech* 1964;19:161-174.

Wen J., Xu B., Tam V. (2009), Numerical study on spontaneous ignition of pressurized hydrogen release through a length of tube, *Combust Flame*, 156 (No. 11) (2009), pp. 2173–2189.

Yakhot V. and Orszag S. (1986), Renormalization group analysis of turbulence. I. Basic theory, *J Sci Comput*, 1 (1986), pp. 3–51.

4. Deflagration Benchmark

4.1 Vented deflagration experiment

4.1.1 Experimental description

The KIT facility is a chamber similar to a garage (see Figure 4-1) in which has been installed a box with glass walls. Inside this transparent facility Figure 4-2, a reactive mixture is introduced during the experiments.

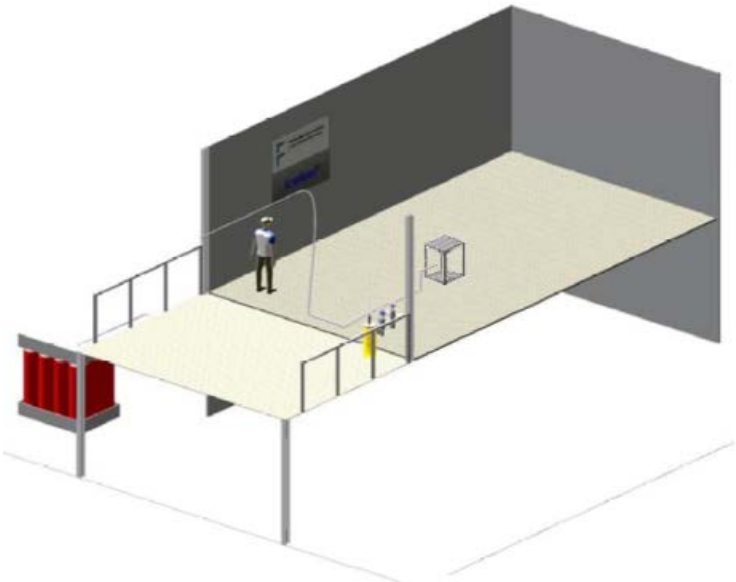

Figure 4-1. KIT facility.

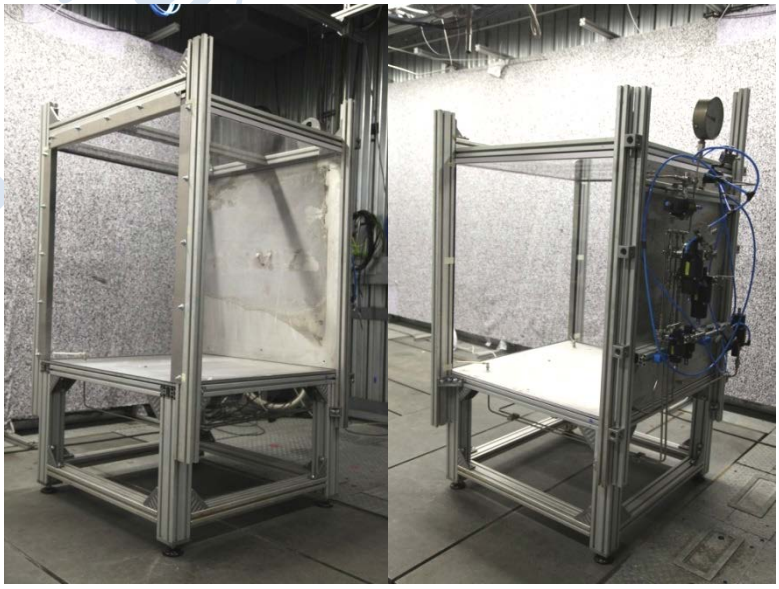

Figure 4-2. Box located inside the KIT facility.

The location of the transducers inside of the facility can be described watching the Figure 4-3. In green are marked the transducers located inside of the box (transducers 1-4) and in orange the transducers located outside (transducers 5-8). Transducer 9 (located close to the opening) is marked in red.

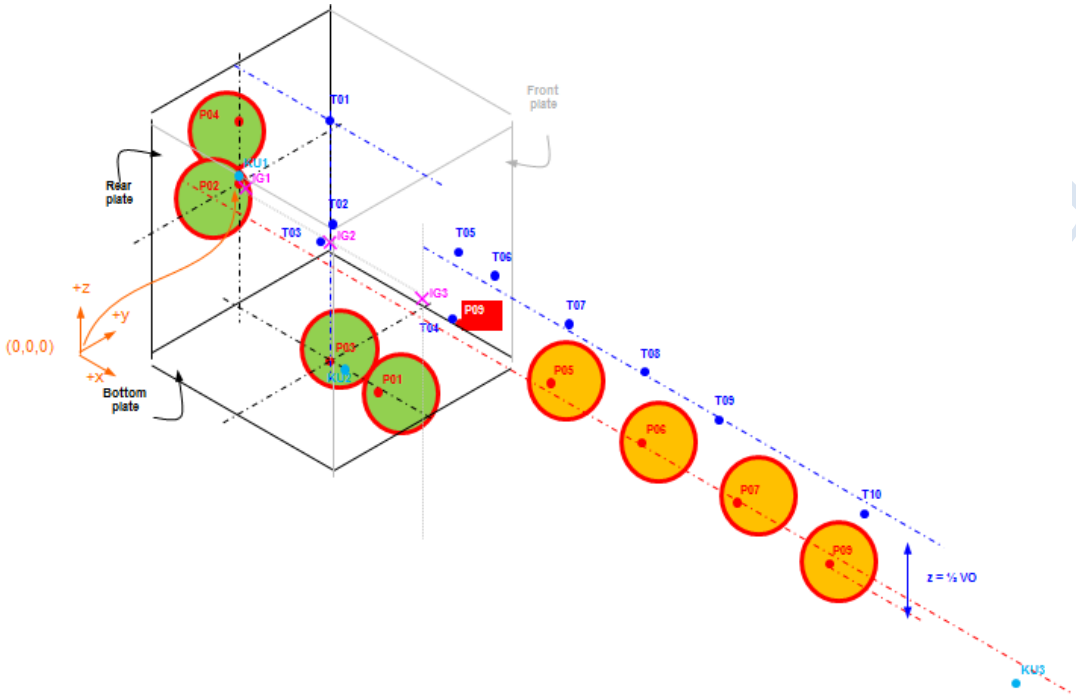

Figure 4-3. Possition of the transducers in the KIT facility. In green interior transducers. In orange exterior transducers.

A realistic view of the transducers and the structure created to support them can be seen in the Figure 4-4.

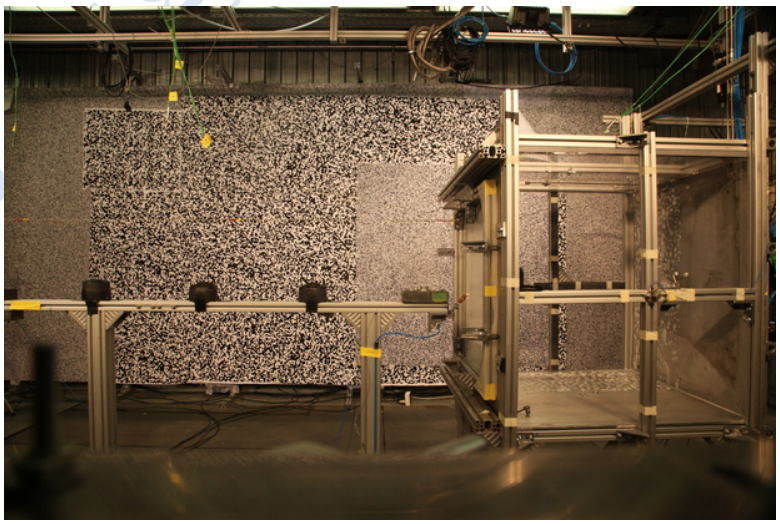

Figure 4-4. Transducers and the structure created to support them.

For simulations we will be mainly interested in a case in which a hydrogen-air mixture of 18% vol. H_2 was introduced inside of the box. The enclosure communicates with the surrounding atmosphere through a hole. Experiments were carried out with openings of different sizes. For the cases chosen for ulterior simulation, it was found taken into account the case with 50% venting.

4.1.2 KIT modelling

4.1.2.1 Governing equations

- The modeling carried out includes the numerical integration of the Navier-Stokes equations. The solution was carried out utilizing the TVD scheme as hydrodynamic solver (Harten 1983).
- The turbulence was modeling utilizing the *k-ε* turbulence model originally created originally by Jones and Launder 1974 or the eddy viscosity eddy diffusivity Large Eddy Simulation model (utilized only in seldom cases (Furebi)).

Combustion model (KYLCOM Model)

KYLCOM model is based on a forest fire algorithm which is utilized to make the flame propagate with a burning speed estimated from an algebraic expression. A phenomenological expression, taking into account local temporal and spatial characteristics of the fluid such as, turbulence level, transport coefficients, other mixture properties, etc., is employed to calculate the flame velocity. The forest fire CREBCOM algorithm Efineko (2001) is used to provide flame advancing mechanism in the course of time integration. The KYLCOM model, as others in 'flame speed' approach, has, therefore, two relatively independent parts, where the first one is responsible for correct evaluation of the turbulent flame speed in the current local conditions, and the second is responsible for the corresponding flame propagation in the simulated media.

KYLCOM description

During the last decades intensive efforts were made to gain the knowledge required to predict turbulent flame velocity under different conditions. The deduced relations take into account the effect of turbulence, integral length of the turbulence, Lewis number, stretching of flame, etc. on combustion rate. They traditionally are expressed in terms of the gas characteristics of fresh gases and differ significantly in their complexity, set of parameters and range of applicability. Following the previous experience of the authors, the formula due to Schmidt et al. (1998) $S_t = S_L + \frac{u'}{\sqrt{1+\frac{1}{Da^2}}}$, was utilized.

Flame propagation model. CREBCOM

For the propagation of the flame the CREBCOM algorithm was utilized. CREBCOM model belongs to the category of Forest Fire models pioneered by Bak et al. (1990). The main characteristic of this model is that a cell starts burning when one or more of the surrounding cells is already consumed up to a limit. An advantage of CREBCOM model is that it does not introduce any special flag or indicator showing whether some cell is burning or not.

Let *f* be a progress variable of the reaction, equal to 0 for the fresh mixtures and to 1 for the completely developed reaction. Let us introduce the criteria value

$$F_{i,j,k} = f^2_{i+1,j,k} + f^2_{i-1,j,k} + f^2_{i,j+1,k} + f^2_{i,j-1,k} + f^2_{i,j,k+1} + f^2_{i,j,k-1} - 3f^2_{i,j,k}.$$

Then CREBCOM burning criteria states that a cell is considered to be burning if F is more than $\left(\frac{1}{2}\right)^2$ That gives us the expression for the chemical reaction rate

$$\frac{df_{i,j,k}}{dt} = \begin{cases} \frac{C_g}{\Delta}\left(1 - f_{i,j,k}\right) & F_{i,j,k} > \left(\frac{1}{2}\right)^2 \\ 0 & F_{i,j,k} < \left(\frac{1}{2}\right)^2 \end{cases},$$

where Δ cell size. The thickness of the flame is approximately of two cells both in original and modified CREBCOM models.

If we apply this formulation to a planar flame moving in the direction of X axes, no gas motion is existing. Let us consider a cell of coordinates (i, j, k) that is about to start burning. For such a cell

$$f_{i,j,k} = f_{i,j,k+1} = f_{i,j,k-1} = f_{i,j+1,k} = f_{i,j-1,k} = 0, \quad f_{i-1,j,k} \neq 0$$

and CREBCOM criteria simplifies to

$$f_{i-1,j,k} > \left(\frac{1}{2}\right).$$

Therefore, for a planar flame whenever more than half of the products are consumed, the next cell starts burning. Then the equation for a burning cell may be easily solved

$$f(t) = 1 - exp\left(\frac{-t \cdot C_g}{\Delta}\right).$$

So that the time t to burn a half of a cell is

$$\tau = ln(2)\frac{\Delta}{C_g},$$

and the flame speed induced by the method is

$$\frac{\Delta}{\tau} = \frac{C_g}{ln(2)}.$$

However, in reality, the flame phenomenon is always accompanied with gas motion. This is due to gas expansion in reaction. A measure of this expansion is σ, the expansion ratio in adiabatic isobaric combustion. To investigate the influence of gas expansion, let us consider a planar flame in a reference system attached to the flame. On one side of the flame there is fresh mixture with velocity v_f fundamental flame velocity whilst on the other side almost burned cells with velocity equal to σv_f. In order to obtain a stationary picture of the flux of

fresh mixture should be equal to chemical consumption rate. The approximation of an advective flux depends on implementation details, particularly on hydrodynamic solver. However we can try to estimate this flux in simplest case. If we consider $\tau = \sigma - 1$. And we perform the assumption, valid for slow flames

$$\rho = \frac{\rho_0}{1+\tau f},$$

Then,

Cell i	***Cell i+1***	***Cell i+2***
$f_i \approx 0$	$0 < f_{i+1} < 0.5$	$0.5 < f_{i+2} < 1$
$V_i \approx V_f$	$V_{i+1} \approx (1+\tau f_{i+1})V_f$	$V_{i+2} = (1+\tau f_{i+2})V_f$
$\rho_i = \rho_i$	$\rho_{i+1} = \frac{\rho_i}{(1+\tau f_{i+1})}$	$\rho_{i+2} = \frac{\rho_i}{(1+\tau f_{i+2})}$

The previous table allows formulating the problem as an infinite set of equations,

$$C_g \frac{1-f_1}{1+\tau f_1} = (f_1 - f_0)V_f$$

$$C_g \frac{1-f_2}{1+\tau f_2} = (f_2 - f_1)V_f$$

$$\vdots$$

$$C_g \frac{1-f_{i+1}}{1+\tau f_{i+1}} = (f_{i+1} - f_i)V_f$$

From this system, C_g is a function of σ only. A simple inspection allows estimating that the variable C_g may be related with the fundamental flame speed as

$$C_g \approx 0.346(\sigma+1)v_f$$

The non-sharp interface between reactants and products and the combustion taking place in several cells make that the model constant C_g should be calibrated numerically. The results of performed numerical tests allow writing the ratio of CREBCOM constant to fundamental flame speed as a linear function of the expansion ratio

$$C_g = (A \cdot s + \mathrm{B})V_f$$

The values *A* equal to 0.243 and *B* equal to 0.375 were obtained as a result.

4.1.2.2 Simulation approach

Inaccuracies in geometry.

The simulations were carried out utilizing initially a very simple geometry trying to simulate strictly the box and its surrounding as it should theoretically appear in the description of the experiments. This included the box and a domain around it (see picture bellow)

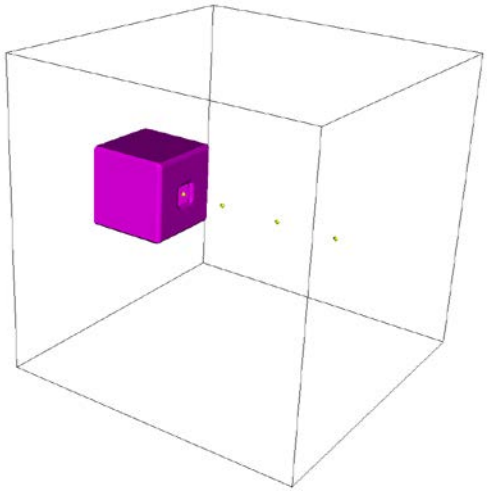

Figure 4-5. Initial geometry utilized for the initiation of the calculation.

After the results obtained in the calculations were evaluated, the facility was visited several times. It was discovered that the initially considered geometry, just regarding the garage, should be completed with significant additions.

Firstly, the facility consisted in four stages (see figure bellow). The two superiors floors are the ventilation system. The middle floor is the garage itself. Additionally, a supplementary volume located in a underground floor completes the set-up.

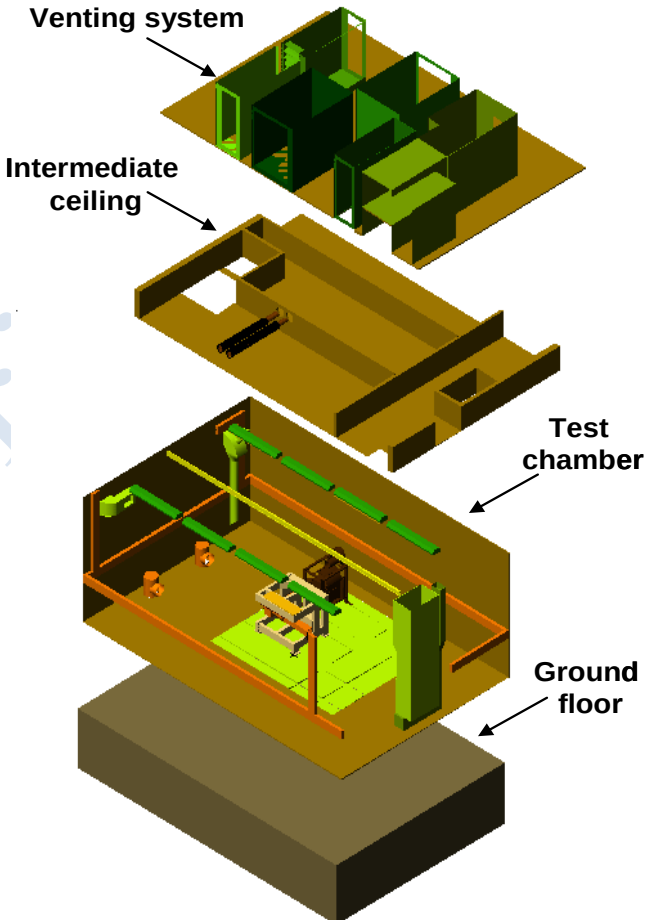

Figure 4-6. Realistic CAD decomposition of the facility into 4 stages.

Furthermore to the complex resulting geometry, non-reported holes and orifices like flaps were existing in the facility. Those orifices communicate the garage facility with the surrounding environment. The flaps are per se closed but open for an overpressure of 0.1 bar which is of the order of the overpressures reached for in this cases. No conclusive statement can be carried out for the status, open or closed, of the flaps.

Figure 4-7. Flaps communicating the interior of the facility with the exterior environment.

The communication between the different floors is also of interests. Certainly the ventilation system is connected through the pipes to the main volume of the facility. The very significant volume located downwards, can communicate through manholes and gaps with the main volume (see Figure 4-8, Figure 4-9 and Figure 4-10)

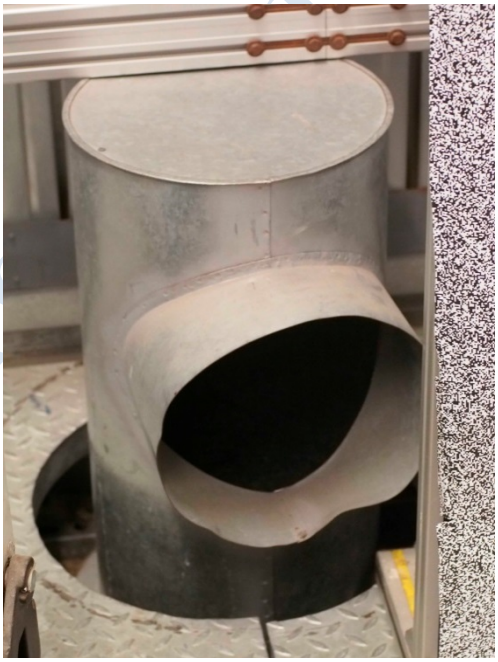

Figure 4-8. Pipe communicating the main volume of the facility and the underground room.

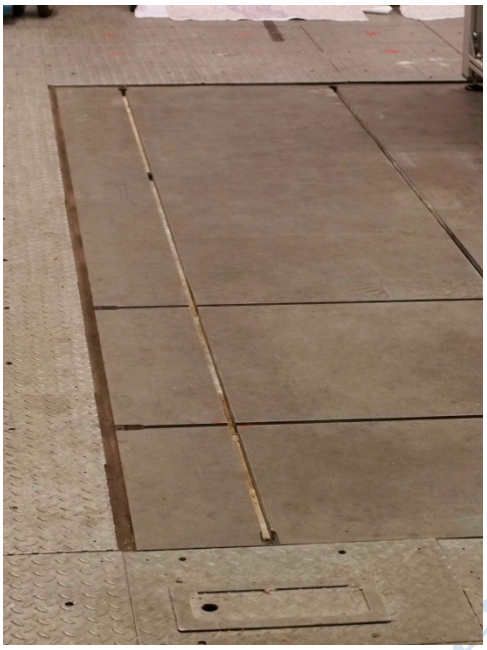

Figure 4-9. Gaps between the plates available for communication between the main volume of the facility and the underground room.

Figure 4-10. Manholes utilized for inspection of the underground volume.

Trials were carried out in order to consider a simplified modeling of the facility as to consider the whole amount of details was judged to be excessive. Several trials resulted into the adoption of the geometry shown in Figure 4-11.

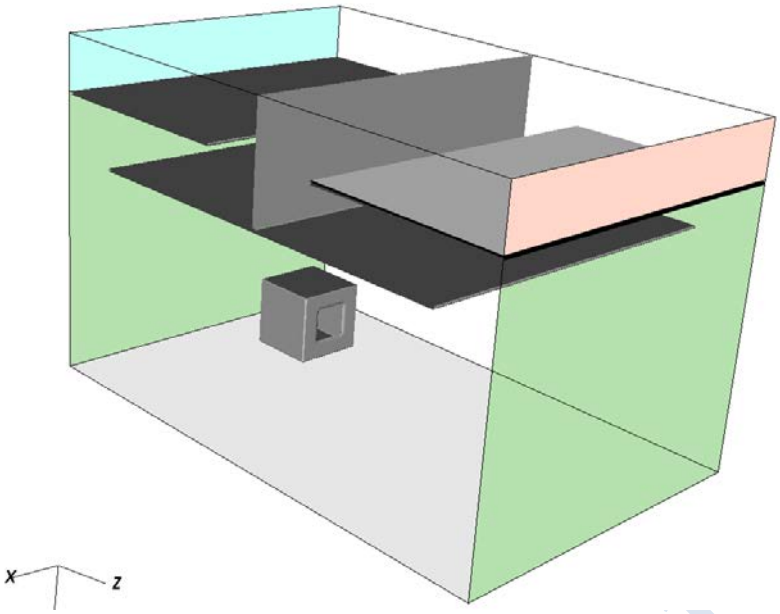

Figure 4-11. Geometry considering a simplified ventilation system (with open boundary conditions through the openings in blue and salmon) and open/closed or partially open boundary conditions in the green area.

In a final development stage, the whole amount of details of the facility was taken into account for the generation of the geometries considered for the experiments, see Figure 4-12, Figure 4-13, Figure 4-14 and Figure 4-15. Note the gap corresponding to the door in the Figure 4-12 and the holes practiced in the lateral surface of the facility. In Figure 4-13 the flaps that communicate with the exterior domain appear also as opened. In Figure 4-13 and Figure 4-14 the pipes communicating the main volume with the underground domains are observable. In Figure 4-14 the orifices communicating with the exterior domain located in the same plane of the door are clearly visible. The piping of the ventilation system can be partially seen in Figure 4-13 and Figure 4-14.

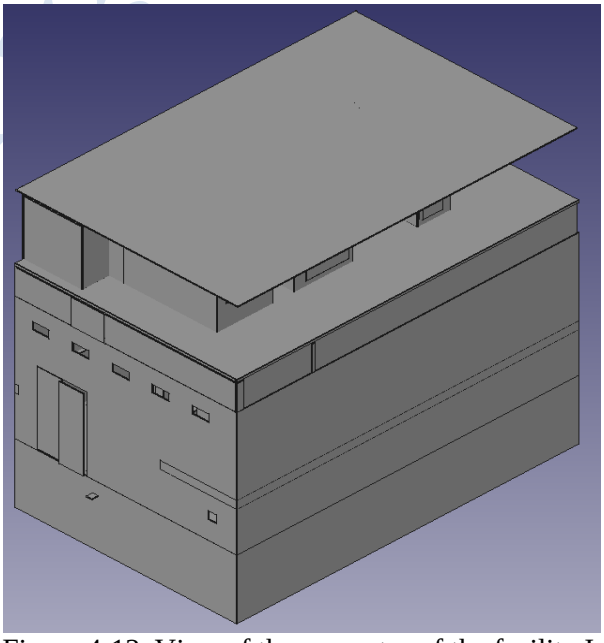

Figure 4-12. View of the geometry of the facility I.

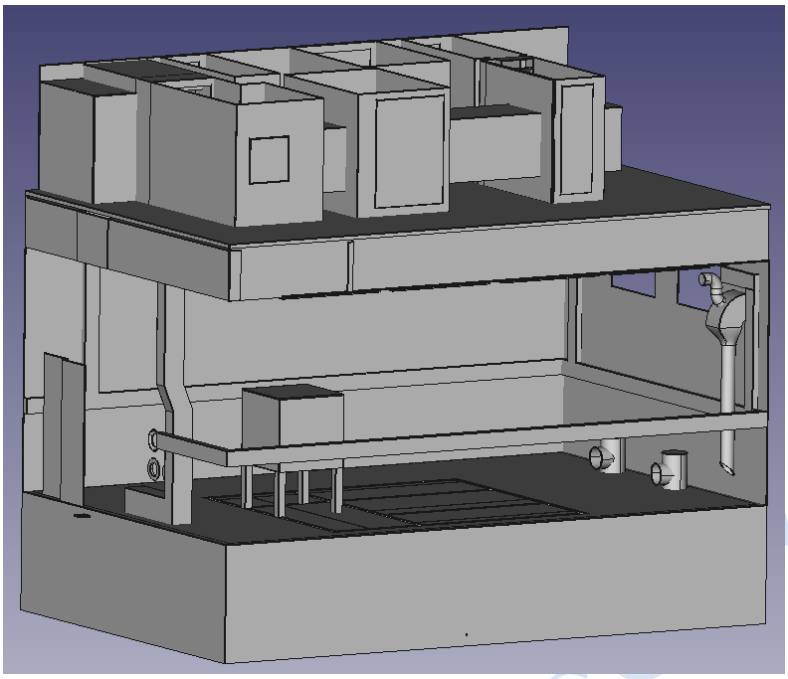

Figure 4-13. View of the geometry of the facility II.

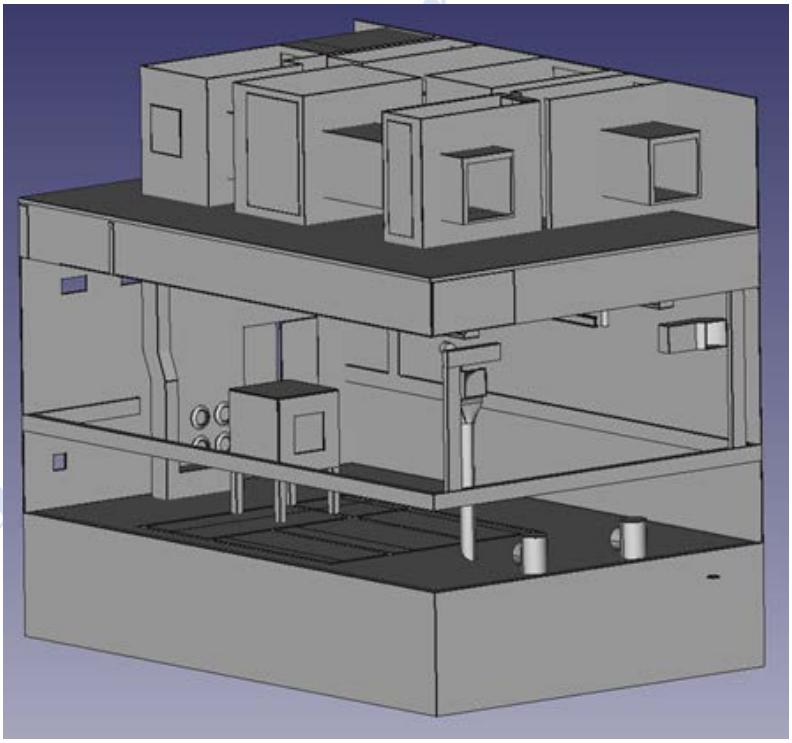

Figure 4-14. View of the geometry of the facility III.

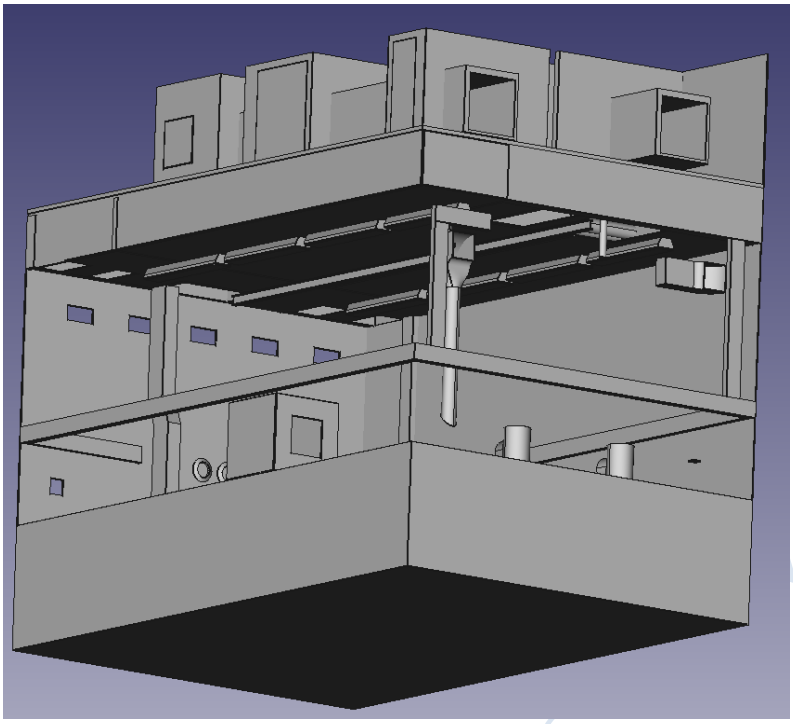

Figure 4-15. View of the geometry of the facility IV.

Summarizing, it could be stated that in this final geometry the following points have been considered in detail: ventilation system, piping of the ventilation system, volume underground (fully taken into account), communication between this volume and the volume above though ground gaps, funnel and manholes, orifices existing in the facility.

Grid information

- The COM3D utilizes exclusively a structured hexahedral grid.
- Details of the grid
  - Original grid: 212x110x68 resolution 4. cm
  - Intermediate grid: 212x132x68 resolution 4. cm
  - Final grid: 160x310x217 resolution 3.45 cm
- The calculations carried out were performed on the basis of “best estimate” methodology utilizing the finest grid possible with the available computational power. The models utilized are intended for under-resolved calculations.

Boundary conditions

Depending on the geometry and the position, the boundaries were considered as open, closed or mirror. When there were open boundary conditions, a sufficient discharge volume was provided in order to allow for the simulation of an open atmosphere. The location of each boundary condition can be easily understood visualizing Figure 4-5, Figure 4-11, Figure 4-12, Figure 4-13, Figure 4-14 and Figure 4-15.

4.1.2.3 Numerical details

- COM3D code an in house development of the KIT was utilized for the simulation in its version 4.6.

- The discretization utilized is a finite differences methodology.
- The solution was carried out utilizing the TVD scheme as hydrodynamic solver Harten 1983.
- The convective terms were discretized utilizing second order centered finite differences.
- The time step utilized was variable and equivalent to a CFL number equal to 0.94. the diffusion number was set-up to me less than 0.44. The most strict condition was taken for the limiting of the time step.

4.1.2.4 Results and discussion

Qualitative development of the explosion

In a first stage ignition takes place close to the wall. The flame propagates in hemispherical shape immediately after with small velocities of the order of the laminar burning velocity. The next qualitative stage starts when the flame abandons its spherical propagation and adopts a shape of half ellipse. Such a shape with an elongated axis in the direction of the discharge orifice continues until the orifice is reached. These three stages correspond to the Figure 4-16 a) and relate to a propagation regime without significant flame interaction with turbulence. Flame acceleration is exclusively due to flame folding and instabilities. In analogy to the so called 'finger flames', this acceleration can be very significant also in absence of turbulent enhancement.

The next propagation stage happens once the flame trespasses the orifice, it interacts with the detached boundary layer and due to the Kelvin-Helmtholtz instability increases very significantly its total shape. In summary, the flame becomes very turbulent and its propagation velocity is high. This stage corresponds to Figure 4-16 b) and c). The macroscopic shape of the flame is the one of a 'mushroom'. Due to the pushing of the flame once it was propagating inside of the box, a very significant amount of reactants have been discharged into the surrounding atmosphere. In this stage the combustion of reactants is very intense.

The final of the previous status is reached when the discharged reactants get exhausted. Afterwards the products propagate in the axial direction without existence of the flame due to inertia and expansion of the products. The temperature of the latter gets gradually reduced due the expansion and turbulent mixing (stages e) and f)).

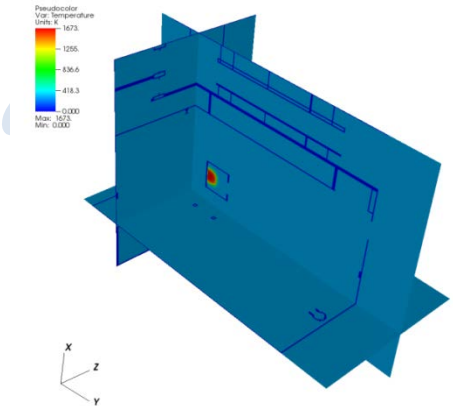

a)

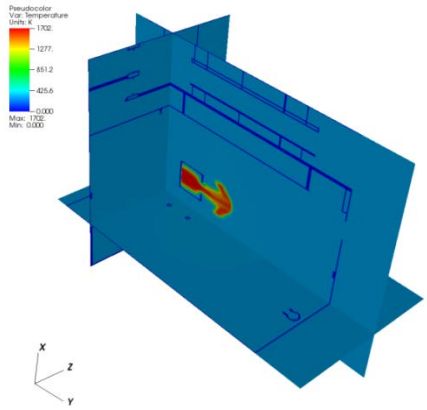

b)

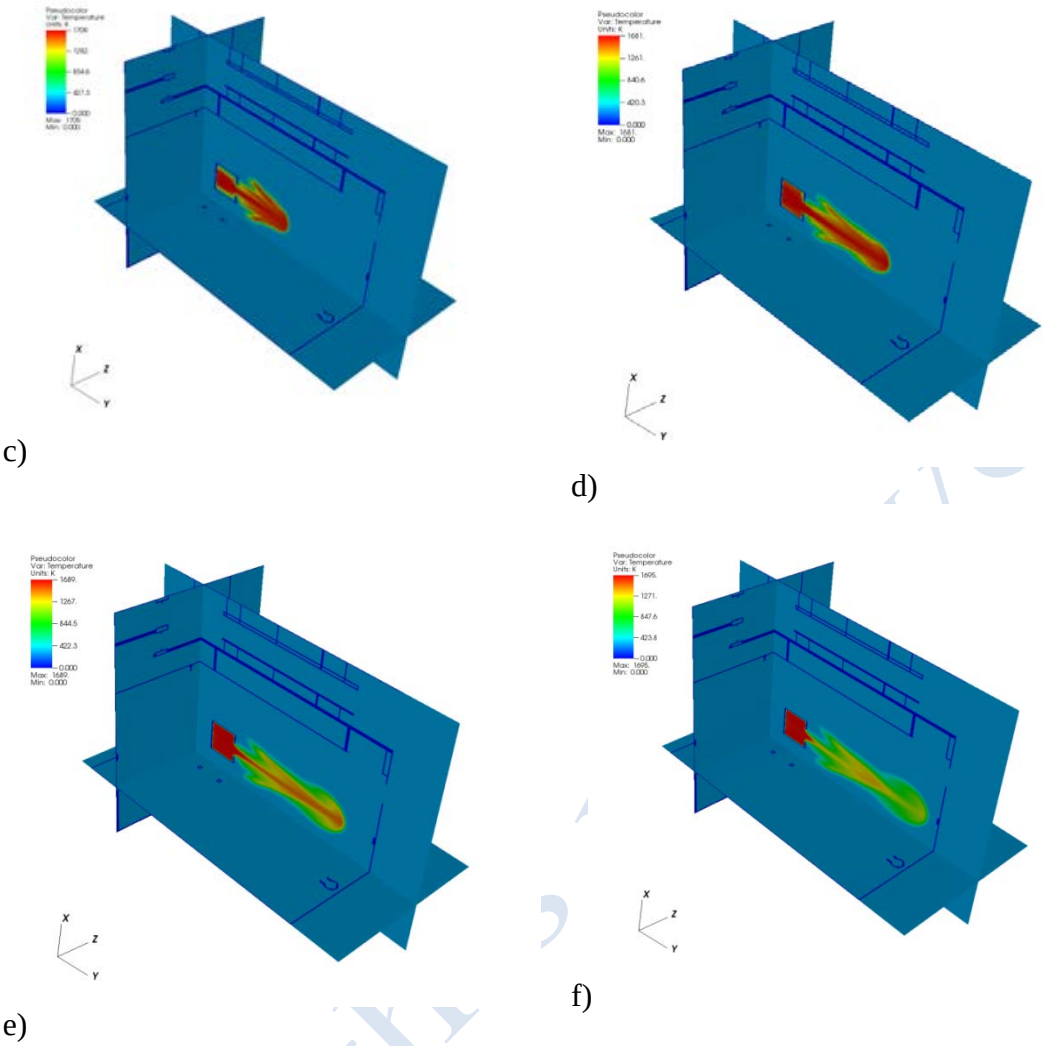

Figure 4-16 General evolution of the explosion.

Initial results

It was already mentioned that three geometrical representations of the facility has been taken into account for the calculations. The most simple one allowed to obtain good results inside of the gas box located inside of the facility.

For the comparison of the results with the experiments we may mention that the experiment was repeated three times. Although the number of repetitions is not suficient to extract statitistical conclusions on the systematic error of the experiments, it is qualitatively much more significant than comparisons againist a single experiment. This is the reason for the utilization of this experiment for the simulations, the unique one that was repeated. The results obtained (for transducers located inside of the box) have been depicted in the Figure 4-17 to Figure 4-20. For the comparions maximum, minimum and average values of the results obtained in the experiments have been plotted. The numerical values obtained show a good reproduction of the expeeriments. The increase, decrease and peak of the overpressure is well obtained.

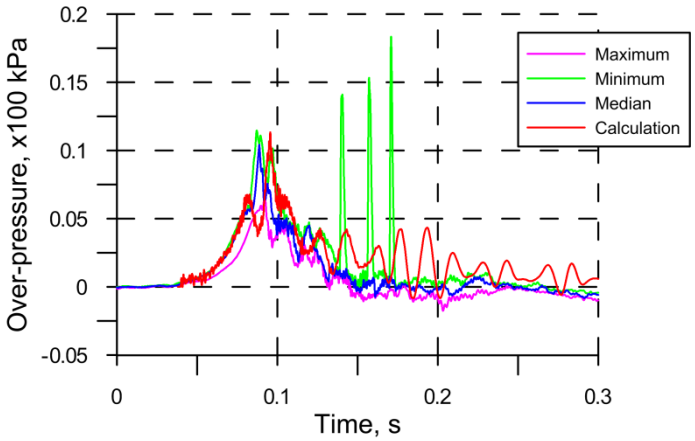

Figure 4-17 Transducer 1

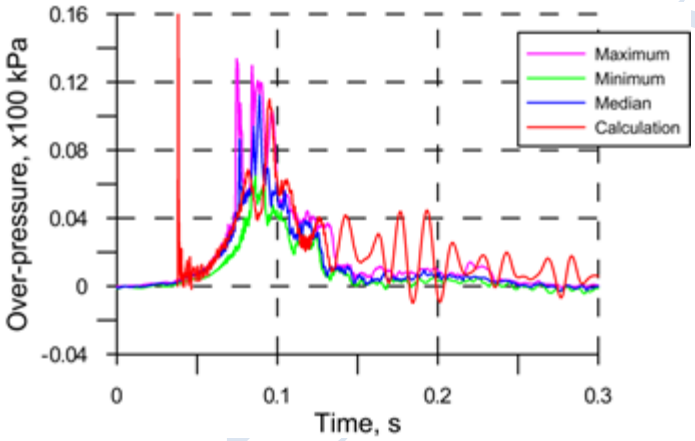

Figure 4-18 Transducer 2

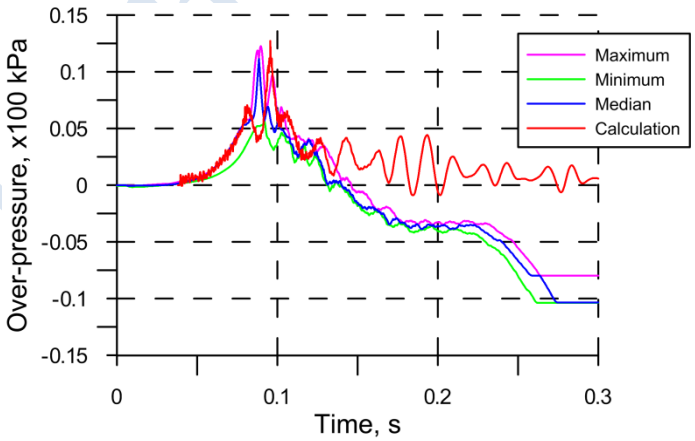

Figure 4-19 transducer 3

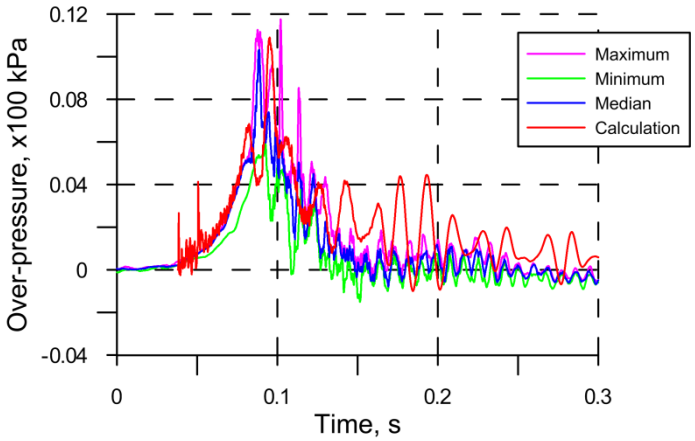

Figure 4-20 Transducer 4

The major divergences that can be seen between the experiments and the calculation are two: the periods appearing in the right side of the curves and the small decrease of the overpressure inside the general initial grow approximately at 0.08 s.

The existence of the cycles in the right hand side of the curves is connected with cycles of charge discharge of the box after the initial discharge of the products (similar to oscillating piston in cylinder). The experiments do not show this tendency in Figure 4-17 and Figure 4-18. The right hand side readings of the Figure 4-19 are not significant. Figure 4-20 show the cycles but strongly minimized. In the opinion of the author the divergences are motivated by two reasons. The first is the fact that the box was resonating in the experiments. These vibrations are motivated by a lack of stiffness due to the big glass windows that lack of inertia momentum. Also the box was not completely hermetic (disregarding the main hole).

The small descent in pressure at a time of around 0.08 s is more worrying is probably connected with an incorrect flame propagation. We may investigate this considering the flame propagation in the longitudinal direction. This magnitude can be traced utilizing the BOS of the experiment Figure 4-21.

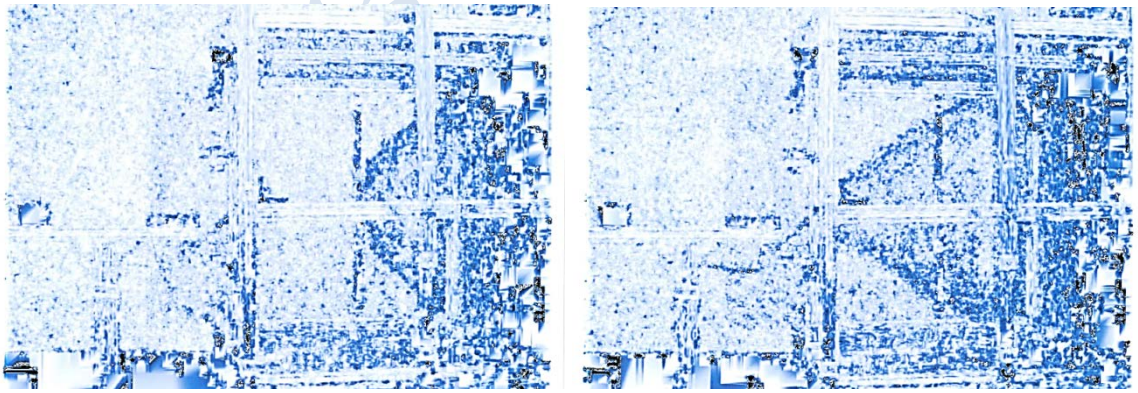

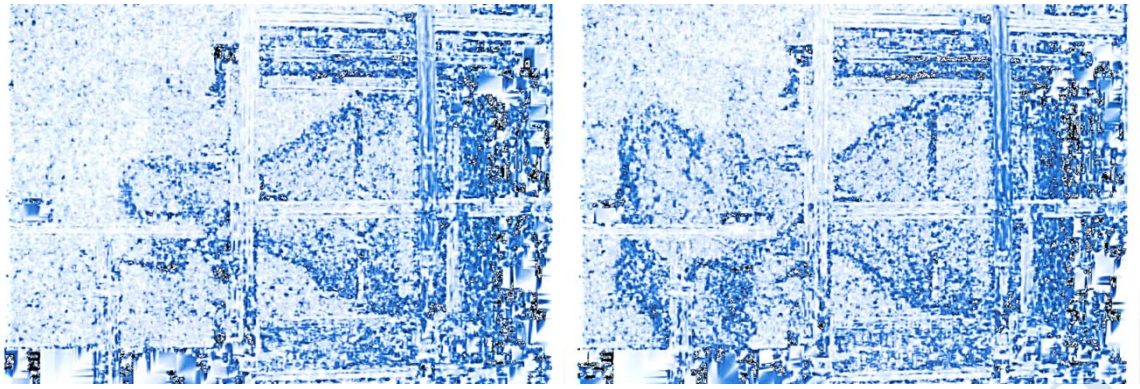

Figure 4-21 BOS pictures of the flame propagation

The resulting flame propagation is obtained from the treatment of the images and is presented in Figure 4-22 and Figure 4-23. It can be easily seen that the calculation show anslightly faster propagation than the experiments in the position, and velocities crossing over the experimental ones. Thus, the pressure decrease at 0.08 s is not connected with a lack of longitudinal flame propagation (overpressure is proportional to Mach number squared). Thus, the transversal propagation should be smaller than in the experiments. Although it is certainly non-conclusive it is suggested that a reason for this divergences could be the effect of the mechanical vibrations in form of sound flame interaction. This effect alters significantly the flame propagation velocity as investigated by Yanez (2013).

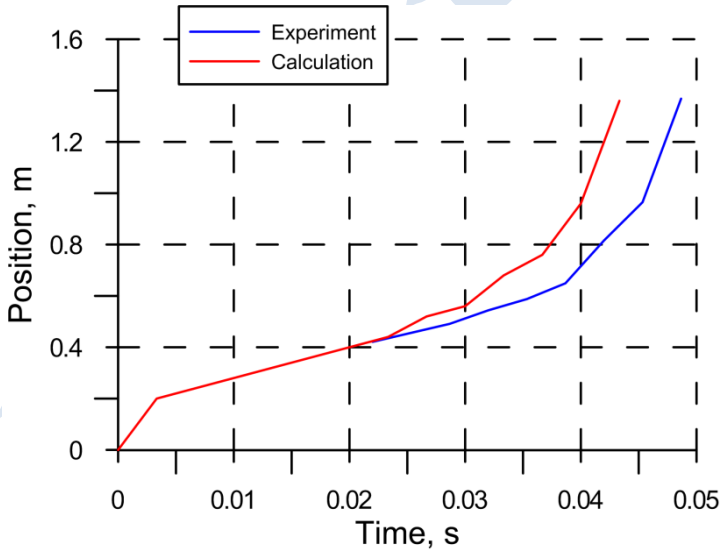

Figure 4-22 Position of the flame as a function of time.

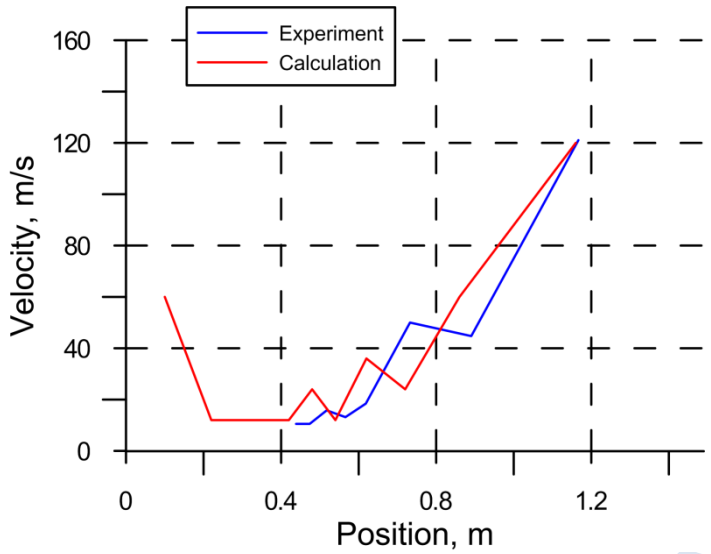

Figure 4-23 Velocity of the flame as a function of the position

The readings obtained at the transducers in the area exterior to the box (far away) was very unsatisfactory, e.g. Figure 4-24 for the transducer number 7, which show unacceptable and divergences at instants around 0.15s. It has been concluded that the divergences are due to a too low velocity provoked by: a) Obstacles; b) Oversimplification of geometry; c) deficit in the model.

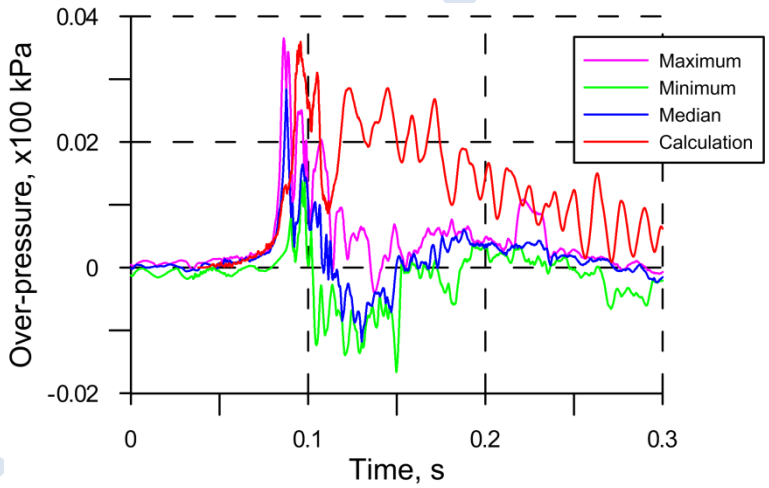

Figure 4-24 Reading of the transducer 7 in the initial simulations to illustrate the unacceptable divergences.

Thus, the original geometry was modified introducing partially opened boundary conditions in additional location to simulate the discharge of the products, see Figure 4-11. Several simulations were performed checking different opening degrees. For its significance, the results corresponding to the case in which the whole green area of the Figure 4-11 was considered to be opened are shown (extreme case). Results corresponding to this case are shown into the Figure 4-25, Figure 4-26, Figure 4-27 and Figure 4-28. The improvements between Figure 4-24 and Figure 4-28 are obvious. The Figure 4-25 and Figure 4-26 show also a reasonable behavior although no conclusive evaluation can be done based on a single experiment (no values for the error are then available). Figure 4-28 show a qualitative

agreement especially in what it touches the negative phase of the signal. Transducers inside the box show no significant divergences with the calculations shown in the original figures.

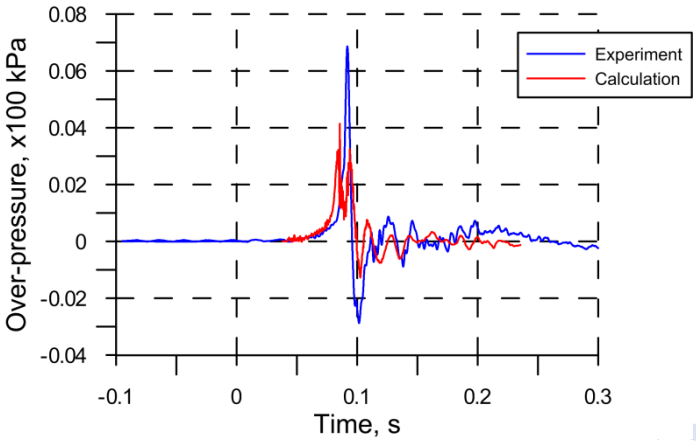

Figure 4-25 Readings corresponding to transducer 5

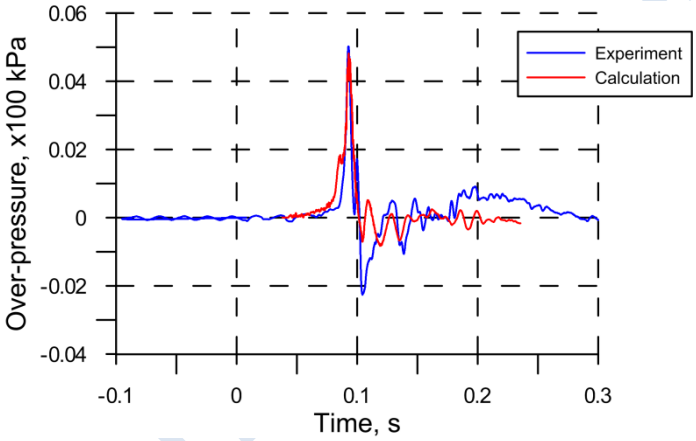

Figure 4-26 Readings corresponding to transducer 6

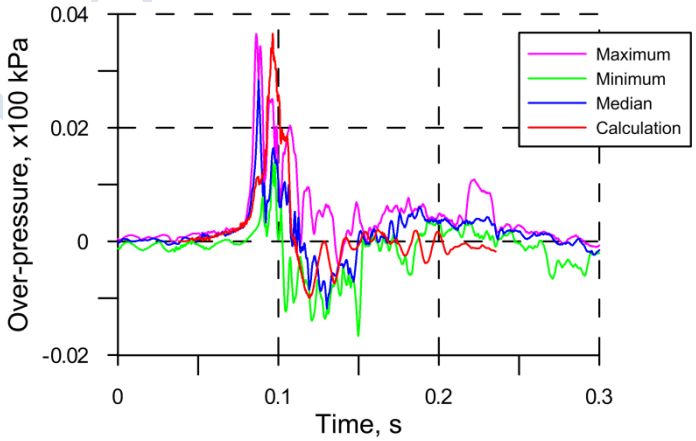

Figure 4-27 Readings corresponding to transducer 7

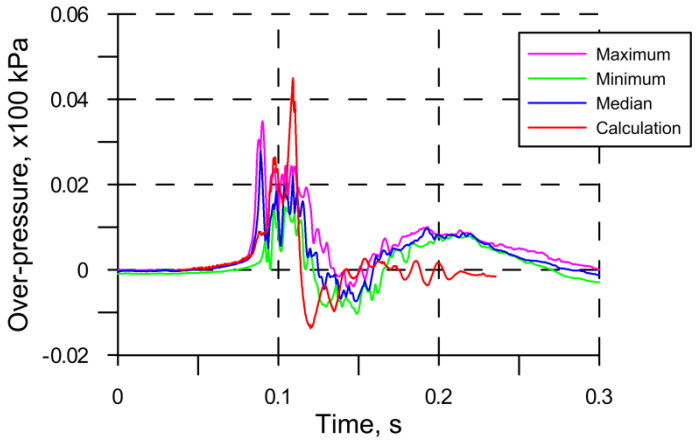

Figure 4-28 Readings corresponding to transducer 8

The relatively good agreement of the results with the theoretical findings motivated the "in place" deep examinations of the facility where the already mentioned divergences were found. As a result, the creation of the third geometry already mentioned was carried out taking the most of the details of the facility into account, see Figure 4-12 to Figure 4-15.

The calculations with this detailed geometry are ongoing.

4.1.2.5 Conclusions

The most important conclusion that can be drawn from this study is the necessity of strong interaction between numerical and experimental teams.

Experiments intended to be modelled should be designed in accordance with a pre-stablished plan in which necessities from modeller have been taken into account. When this is not possible, systematic and pre-stablished visits to the facility should be carried out by the modellers. Divergences between the blueprints and the real final set-up should be identified.

The measurements should be as non-intrusive as possible. Care should be given that the significant part of the process should not be significantly modified due to the instrumentation. The modeling should then consider the facility in full details. Partial modeling or simplified one should be avoided as the simplifications can have very important significance.

4.2 Open deflagration experiment

4.2.1 Experimental description

A series of experiments with near stoichiometric hydrogen-air deflagrations, in unconfined hemispherical volumes, were performed by the Fraunhofer Institute for Propellants and Explosives (Porter, Schneider, 1983). The principal aim of these experiments was to investigate the dependence of flame propagation velocity on the cloud size. Mixtures were ignited at ground level inside the shell made of thin polyethylene (PE) film to exclude the effect of reflected pressure waves. Although the experiments aimed to create a stoichiometric hydrogen-air mixture, a non-homogeneous composition could exist, particularly in the upper section of the balloon, leading to potentially inaccurate measurements (Porter, Schneider, 1983).

This present study focuses on test GHT 34, with hydrogen-air mixture equal to 29.7% by volume in a 20 m diameter hemisphere. The maximum flame propagation velocity was 84 m/s, with the initial burning velocity estimated to be 2.39 m/s (Porter, Schneider, 1983). A rhombus-shaped wire net was laid over the hemispherical balloon which was fastened to the ground at 16 points to compensate for the buoyancy force. In order to make the hydrogen-air flame visible in daylight finely ground NaCl powder was dispersed inside the balloon at the end of the filling process, in order to produce a yellow-coloured flame. The result of this is shown in the snapshots in Figure 4-29.

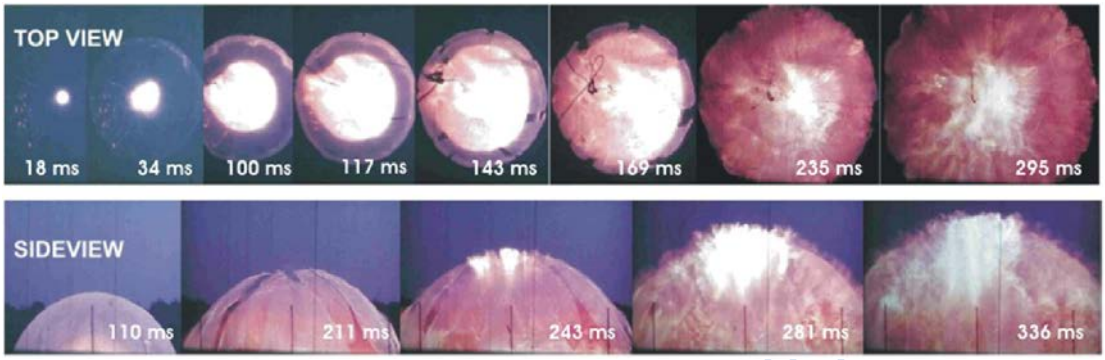

Figure 4-29: Snapshots of flame propagation in test GHT 34 (20 m H_2-air mixture diameter).

Explosion pressures were measured at distances of 2.0, 3.5, 5.0, 6.5, 8.0, 18.0, 25.0, 35.0, 60.0 and 80.0 m from the point of ignition. A summary of the experimental conditions for this test is shown in Table 4-1.

Table 4-1. Summary of experimental conditions and results for test GHT 34.

$H_2, \%vol$	T_i, K	p_i, kPa	E_{ign}, J	V, m^3	Hemisphere diameter, m	Maximum experimental flame speed, m/s
29.7	283	98.9	150	2094	20.0	84

During this test the flame propagated in an almost hemispherical form. The balloon shell first stretched slightly outwards until it burst, at the point where the flame had reached about half of the original radius of the balloon. The explosion overpressure of about 6 kPa was practically the same within the cloud distances in the test. A sharp overpressure peak of about 10 kPa followed flame propagation. This peak occurred when the flame passed the sensors on the ground, and it is thought that this peak is probably associated with the mounting of the PE foil in the sensor housing.

4.2.2 NCSRD modelling

4.2.2.1 Governing equations

For the CFD simulations the ADREA_HF code was used (Venetsanos et al. 2010). The model used solves the space-averaged Navier-Stokes equations along with the energy equation (conservation equation of static enthalpy) and the conservation equation of each of the mass fraction of the species that take part in the combustion process. The multi-component mixture is assumed to be in thermodynamic equilibrium. The equation of state for ideal gases relates pressure and enthalpy with density and temperature. Turbulence is modelled using the RNG LES. The set of main equations that was used are presented in (Tolias et al. 2014).

The main issue in deflagration modelling is the estimation of the reaction rate which appears in the equation of species as source term. The combustion process occurs typically in a very thin area (flame front) which propagates in space over time. For real case scenarios, this area is very small compared to the length scale of the problem. Consequently, direct numerical simulation with detailed chemistry is not possible at the present. As a result, models for the estimation of the reaction rate need to be used. The ADREA_HF code implements the "Multi-phenomena turbulent burning velocity model" (Molkov 2012) developed in UU. Details about the implementation in the ADREA_HF can be found in (Tolias et al. 2014).

Two variations of the combustion model were examined. The "Multi-phenomena turbulent burning velocity model" (Molkov 2012) and a simpler variation of it, the RNG combustion sub-model which has been previously used again for the simulation of the same experiment (Molkov et al. 2006).

RNG combustion sub-model

In this model, the turbulent burning velocity is estimated by the equation:

$$S_t = X_k \times S_u \times \exp\left(\frac{u'^2}{S_t}\right) \tag{4.2.1}$$

where S_u is the laminar burning velocity u' the subgrid scale velocity and X_k the wrinkling factor which accounts for the turbulence generated by the flame front itself. X_k is estimated from the equation:

$$X_k = 1 + \left(X_k^{\max} - 1\right)\left[1 - \exp\left(-R/R_0\right)\right] \tag{4.2.2}$$

where $X_k^{\max}$ the upper limit for a flame wrinkling factor (constant, equal to 3.6 in our simulations), R the distance from the ignition point and $R_0 = 1.2$ m. Finally, the laminar burning velocity is calculated from the equation:

$$S_u = S_{u0} \times \left(\frac{p}{p_0}\right)^{\varepsilon} \tag{4.2.3}$$

where S_{u0} the laminar burning velocity at the initial pressure p_0 (constant, equal to 1.96 m/s in our simulations) and $\varepsilon = 0.565$.

Multi-phenomena turbulent burning velocity model

A detailed description of the "Multi-phenomena turbulent burning velocity model" can be found in (Molkov 2012). The values of the main parameters that were used in our simulations are:

$$X_k^{\max} = 3.6,\ R_0 = 1.2\ m,\ y = 0.5,\ S_{u0} = 1.96\ m/s,\ \varepsilon = 0.565,\ X_{lp} = 1.25 \tag{4.2.4}$$

The above values was constant during the simulation.

4.2.2.2 Simulation approach

ADREA-HF uses Cartesian grid. Three different domain sizes were tested in order to examine the impact on the result:

- **Domain 1**: Main domain (L x W x H): 200 x 200 x 100 m
- **Domain 2**: Extended domain (L x W x H): 300 x 300 x 150 m

- **Domain 3**: More extended domain (L x W x H): 400 x 400 x 200 m

Furthermore, three different grids were tested to perform the grid independence study:

- **Grid 1**: Coarse grid: 442,225 cells (1.0 m cell size inside hemisphere)
- **Grid 2**: Fine grid: 953,127 cells (0.5 m cell size inside hemisphere)
- **Grid 3**: Finer grid: 1,371,791 cells (0.25 to 0.5 cell size inside hemisphere)

The cells' volume is increased gradually in the area away from the hydrogen-air mixture (expansion ratio from 1.08 to 1.12) in order to save computational time.

4.2.2.3 Numerical details

ADREA-HF uses the finite volume method on a staggered Cartesian grid. A difficulty in this kind of mesh is how to define accurately the initial conditions in the hemisphere. In order to generate easily the initial conditions when the grid changes, a code was developed which calculates the initial conditions in every cell of a given grid. In cells which are totally inside the hemisphere the mass fractions are calculated based on the 29.7% v/v hydrogen-air concentration. In cells which are partially inside the hemisphere: 1. We estimate (numerically) the volume of the blocked part of the cell (i.e. the volume of the union of cell with sphere) and 2. we "distribute" the mass of the blocked part of the cell in the whole cell and we calculate the new mass fractions (no mass loss). Fuel mass relative error (which is introduced only from the numerical method used to estimate the volume of the union of a cell with the sphere) in the whole domain was only 0.00023% for a coarse grid and even less for a fine one. In Figure 4-30 the initial hydrogen mass fraction iso-surfaces and contours are shown. We observe that an almost hemispherical shape of the initial distribution is achieved even with the coarse grid. This is observed also in Figure 4-31. In this figure, hydrogen mass fraction contours at z=0 plane are presented. The grid is also displayed.

The pressure and velocity equations are decoupled using a modification of the SIMPLER algorithm. For the discretization of the convective terms in the momentum equations a second order accurate bounded central scheme was used while in the conservation equations of species and energy a second order accurate bounded linear upwind scheme. The implementation was carried out using a deferred-correction approach via the source term. For the time advancement, the second order accurate Crank-Nicolson numerical scheme was chosen. The time step is automatically adapted according to prescribed error bands and the desired Courant–Friedrichs–Lewy (CFL) number which maximum value was set equal to 0.8.

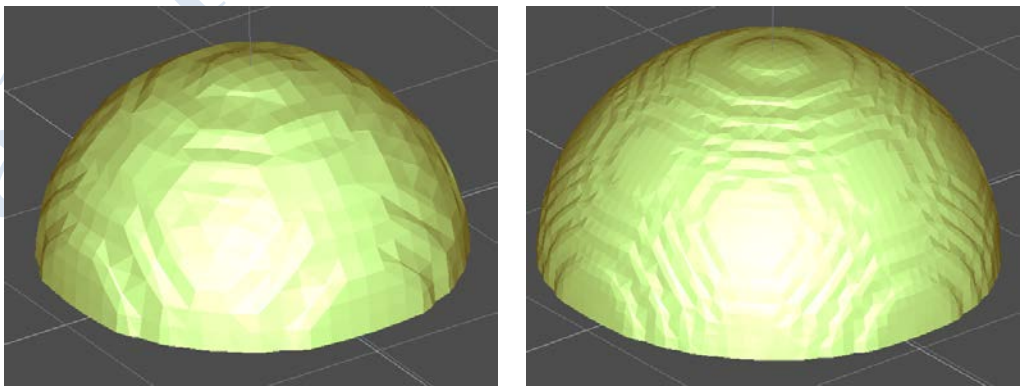

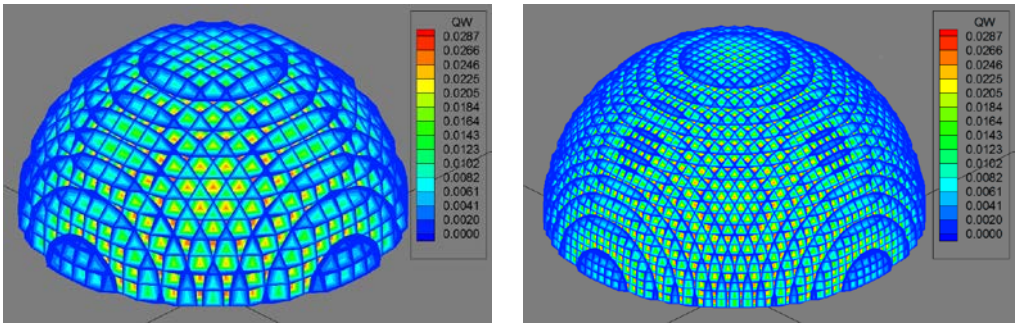

Figure 4-30. Hydrogen mass fraction Iso-Surfaces Q_W=0.02 kg/kg (top row) and Hydrogen mass fraction 3D contours (bottom row), for the coarse (left column) and the fine grid (right column) at initial conditions.

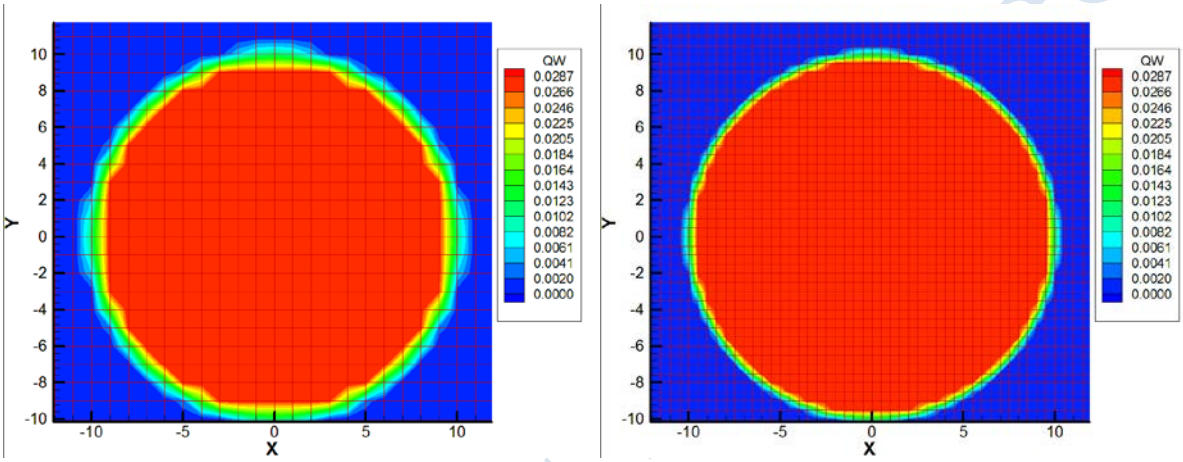

Figure 4-31. Hydrogen mass fraction contours at z=0 plane for the coarse (left) and the fine (right) mesh at initial conditions.

In all exit planes (lateral, front, back and top) the non-reflecting type boundary conditions for the normal velocities is chosen, while for the parallel to the exit planes' velocity components, zero gradient boundary conditions are applied. Zero gradient is utilized also for the mass fraction of species. As initial conditions, a stagnant flow field with no turbulence is specified. Initial temperature and pressure were set equal to experimental values, i.e. 283 K and 98900 Pa respectively. In the hydrogen-air premixed area an initial mass fraction of hydrogen and oxygen is specified as described above. Outside this area the mass fraction of oxygen is set equal to 0.2329. Nitrogen is the inert specie. Ignition is modelled by fixing the reaction rate in a cell at the ignition point, in order the initial amount of fuel to be burned at a determined interval. This interval is estimated by the formula $\frac{Dx/2}{E \times S_{u0}}$ where Dx the size of the cell at ignition point, E = 7.2 the expansion coefficient and S_{u0} = 1.96 m/s the laminar burning velocity at the initial pressure. The time interval for the Grid 1 is equal to 0.035 s, for the Grid 2 is equal to 0.0177 s and for the Grid 3 is equal to 0.00886 s.

4.2.2.4 Results and discussion

RNG combustion sub-model

In Figure 4-32 pressure at six different locations is presented for the three different grids using the RNG combustion sub-model. The Domain 1 was used. We observe that the results are almost identical between grids. Thus, grid independency is achieved even with the coarse

grid. Good agreement between simulations and experiment is observed regarding the maximum value of pressure for all positions except at 80 m. On the other hand, the negative phase of pressure peaks is not reproduced well in most cases. Furthermore, the rate of decrease of pressure after the maximum value has been achieved is underestimated by the computational model.

In Figure 4-33 the flame radius for the three different grids (on Domain 1) is presented as a function of time. Some discrepancies between the results of the different grids are observed. However, all the simulation lines exhibit the same behaviour: At the initial time the agreement with the experiment is very good. After approximately t=0.16 sec, the model fails to reproduce the acceleration of the flame front. As a result the simulated flame position diverge from the experiment.

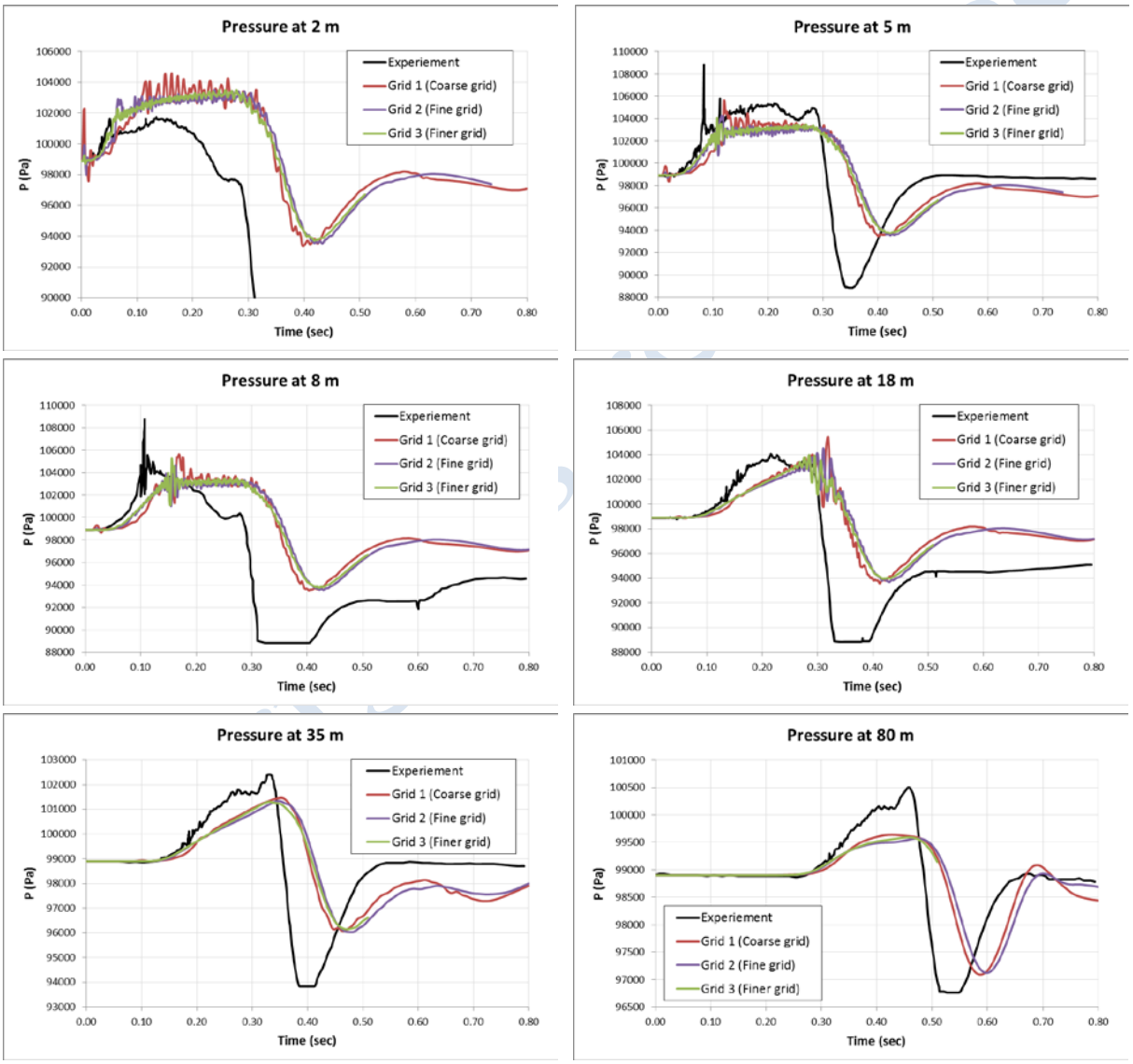

Figure 4-32. Pressure at 2, 5, 8, 18, 35 and 80 m from the center of the hemisphere, for three different grids (on Domain 1) - RNG combustion sub-model.

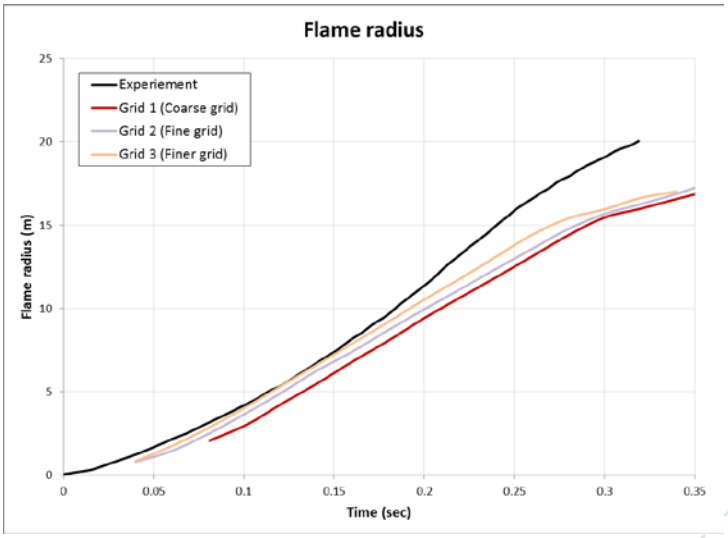

Figure 4-33. Flame radius as a function of time for the three different grids (on Domain 1).

In Figure 4-34 pressure at six different locations is presented for the three different domain sizes. The Grid 1 was used. We observe that the domain size has a significant impact on the results at the closest to the boundary sensor (80 m). At the other positions, the extended domains affect the results only at the tail of the pressure-time curve. We observe that when we use Domain 1 (200 x 200 x 100 m), the pressure fails to return to its initial value. Domains 2 and 3 (extended domains) however reproduce this physical behavior. Small differences between Domain 2 and 3 are observed only at the tail of the pressure-time curve at the last position (80 m). At that sensor, even the Domain 2 fails to restore the initial value of the pressure and the more extended Domain 3 is required. However, this different is not too significant and thus the Domain 2 will be used next.

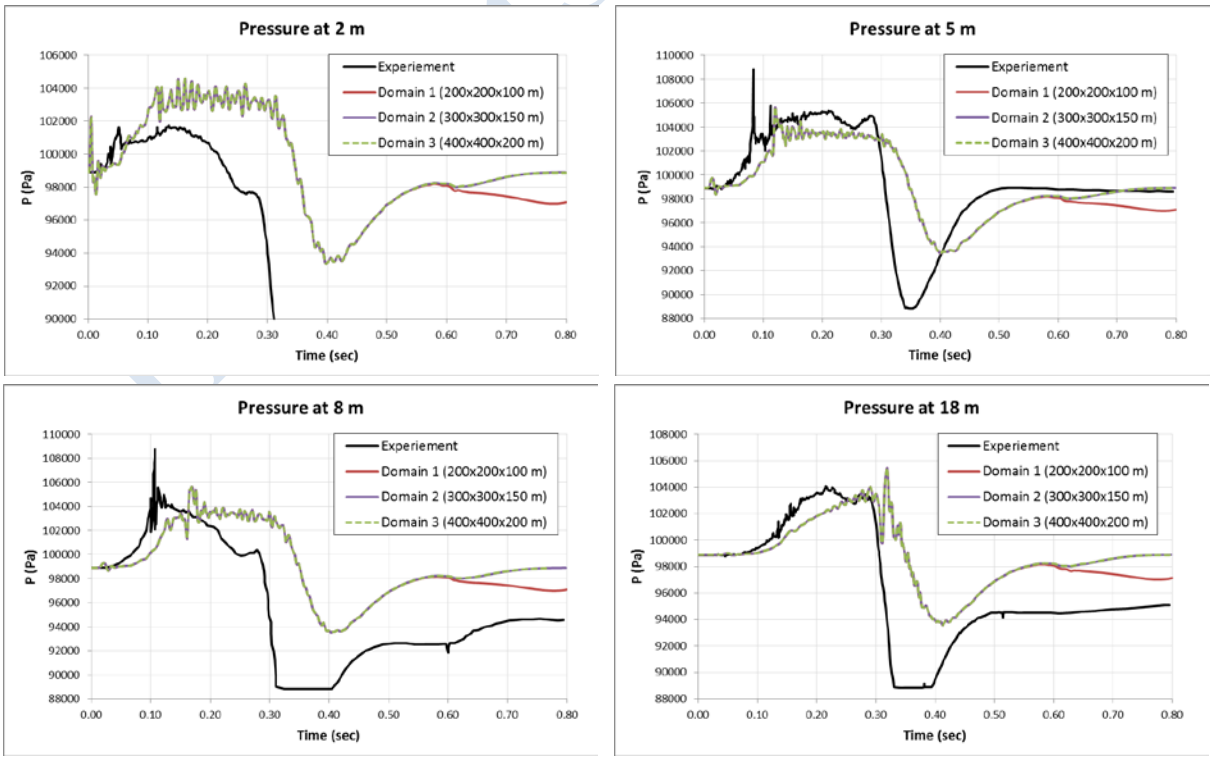

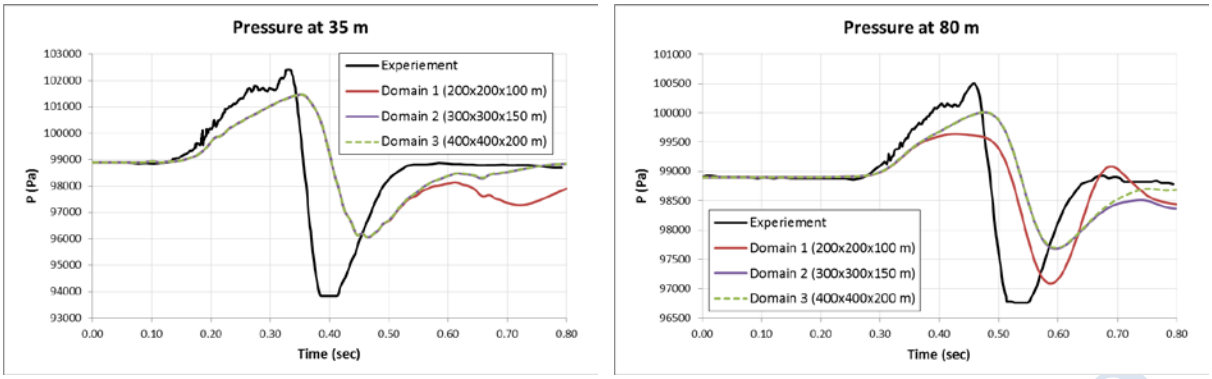

Figure 4-34. Pressure at 2, 5, 8, 18, 35 and 80 m from the center of the hemisphere, for three different domain sizes (on Grid 1).

Multi-phenomena turbulent burning velocity model

The coarse mesh and the extended domain were used for the "Multi-phenomena turbulent burning velocity model" simulations. A key parameter of this model is the fractal dimension. In Figure 4-35 the pressure time histories for three different values of the fractal dimension (2.1, 2.2 and 2.3) are compared against the experiment. We observe that the results are strongly dependent on the fractal dimension value. The best agreement with the experiment is obtained with the value of 2.3.

A Semi-empirical relation for fractal dimension which is suggested for the model (Molkov 2012) was also tested. The equation relates the fractal dimension with the subgrid scale velocity and the laminar flame speed.

$$D = \frac{2.04}{u'/S_u + 1} + \frac{2.35}{S_u/u' + 1} \tag{4.2.5}$$

In Figure 4-36 the model using this relation is compared with the model using constant values of the fractal dimension. We observe that the results of the semi-empirical relation lays between the results of constant fractal dimension equal to 2.1 and 2.2. Consequentially, the empirical relation fails to approximate the value of 2.3 for which the best agreement with the experiment had been achieved.

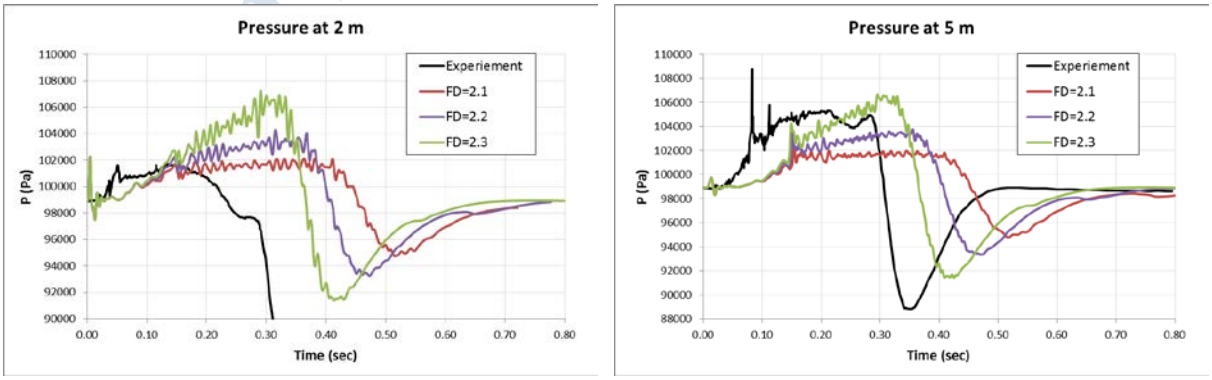

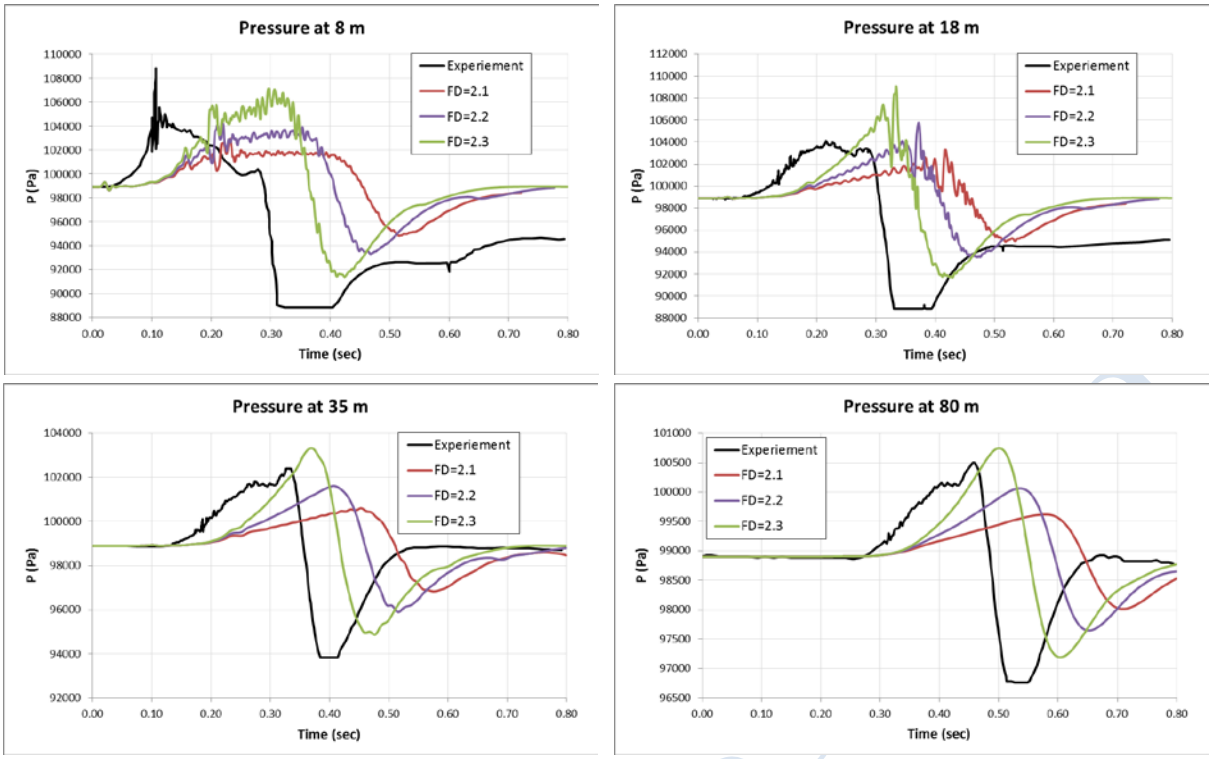

Figure 4-35. Pressure at 2, 5, 8, 18, 35 and 80 m from the center of the hemisphere, for three values of fractal dimension - Multi-phenomena turbulent burning velocity model.

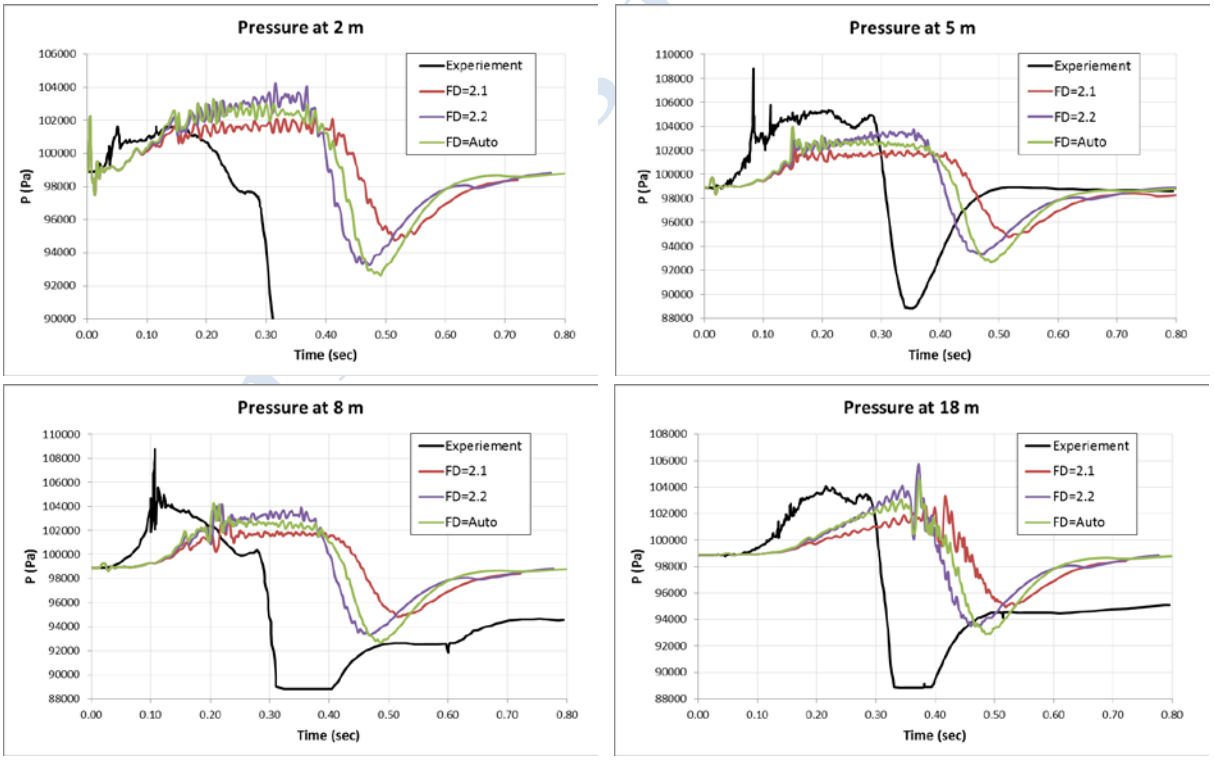

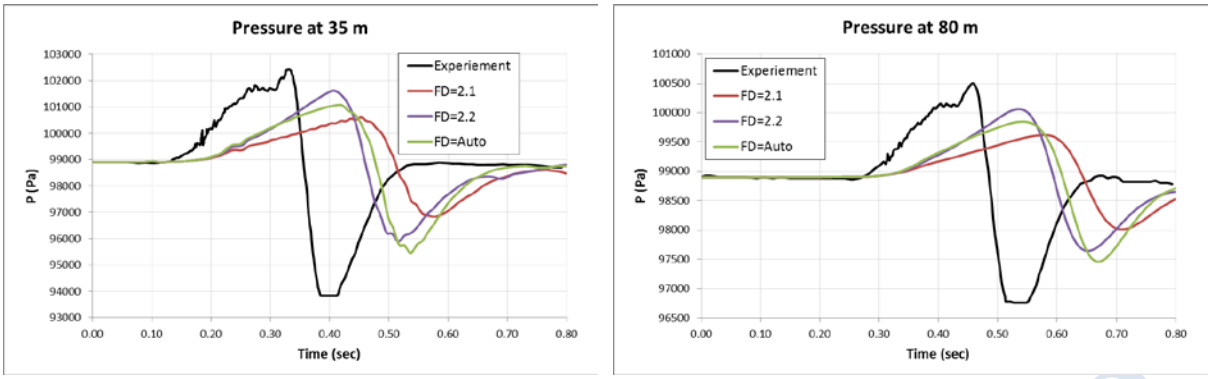

Figure 4-36. Pressure at 2, 5, 8, 18, 35 and 80 m from the center of the hemisphere - Comparison of the Fractal semi-empirical relation with the constant values model.

Finally, in Figure 4-37 the comparison between the two combustion models is shown. On overall, the "Multi-phenomena turbulent burning velocity model" with fractal dimension equal to 2.3 achieves better agreement with the experiment, both in terms of maximum/minimum pressure and in terms of rate of pressure rise/fall. The only drawback of the model is a time-delay that is observed in the pressure time histories. In Figure 4-38 the comparison regarding the flame radius is shown. The Grid 2 was used for these simulations. We observe that the "Multi-phenomena turbulent burning velocity model" predicts the acceleration of the flame front whereas the RNG model fails. On the other hand, a delay in time is observed.

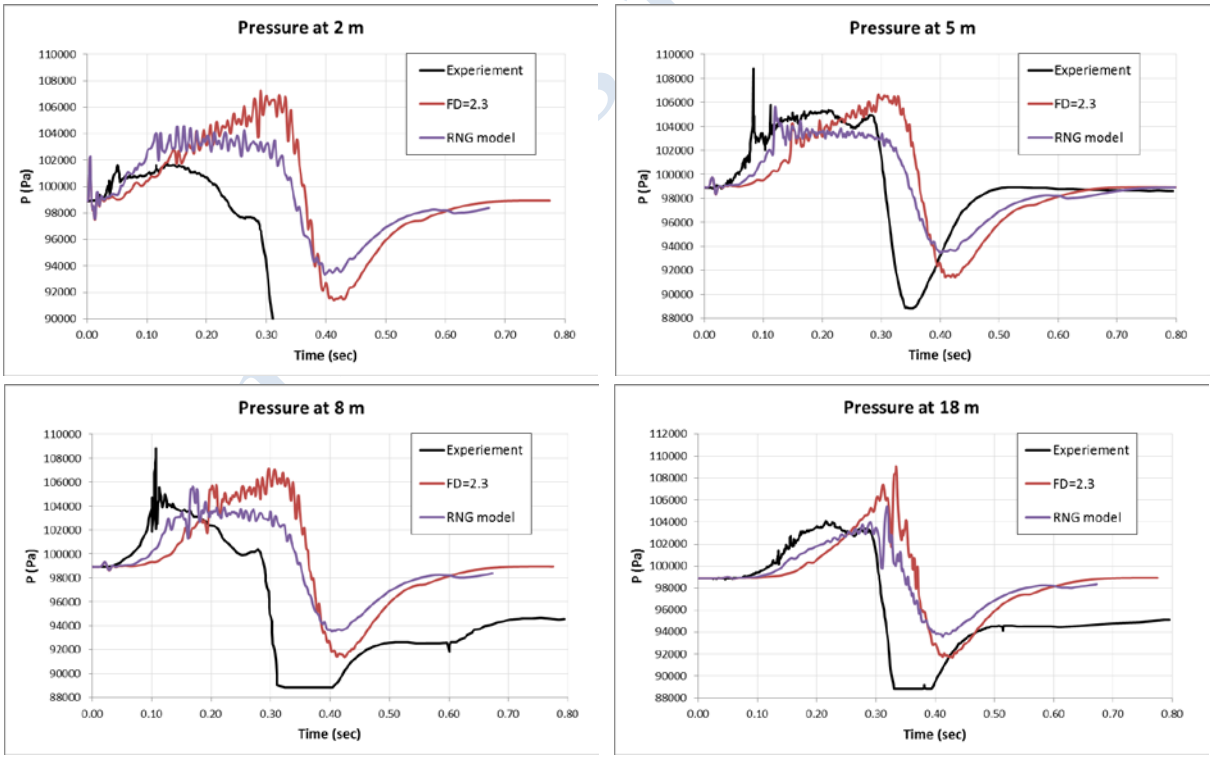

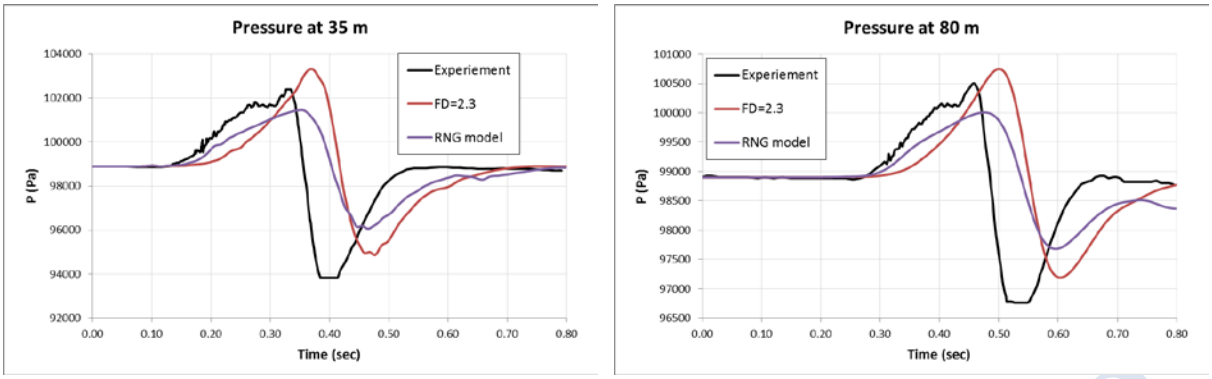

Figure 4-37. Pressure at 2, 5, 8, 18, 35 and 80 m from the center of the hemisphere - Model comparison.

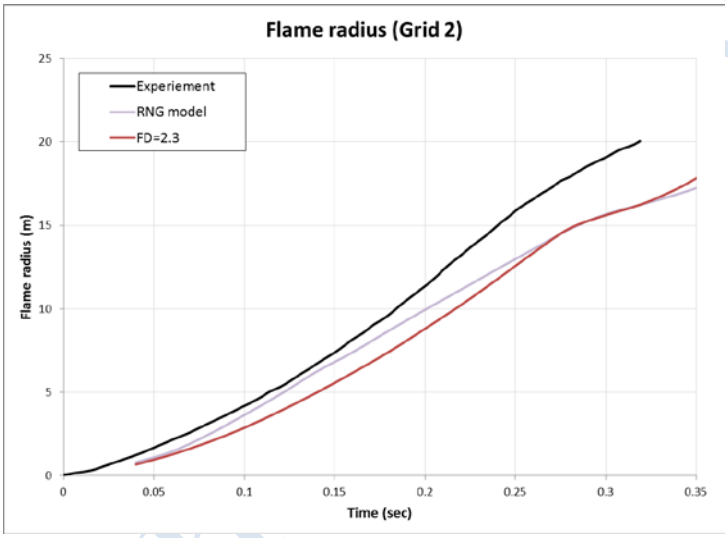

Figure 4-38. Flame radius as a function of time for the two combustion models.

4.2.2.5 Conclusions

A large scale open deflagration experiment was simulated using two combustion models. The "Multi-phenomena turbulent burning velocity model" and a simpler variation of it, the "RNG combustion sub-model". The effect of grid and domain size was examined. The grid with 1.0 m cell size inside hemisphere found to be proper for simulating the generated overpressures. The domain size of 300 x 300 x 150 m needs to be used in order to achieve unaffected from the boundaries results. A parametric analysis for the fractal dimension parameter of the "Multi-phenomena turbulent burning velocity model" was performed. The value of 2.3 achieved the best agreement with the experiment. A semi-empirical relation for the fractal dimension was also tested. This relation failed to approximate the value of 2.3. The "Multi-phenomena turbulent burning velocity model" achieved very good agreement with the experimental results. The agreement was better than the "RNG combustion sub-model", both in terms of maximum/minimum pressure and in terms of rate of pressure rise/fall. The "Multi-phenomena turbulent burning velocity model" was also succeeded in reproducing the acceleration of the flame front. However a time-delay of the flame front position was observed.

4.2.3 UU modelling

4.2.3.1 Governing equations

The governing equations used during the simulations describing combustion were obtained by filtering the three-dimensional conservation equations of mass, momentum, energy and species concentration and are published elsewhere, e.g. (Molkov et al., 2006).

Premixed flame propagation model

The transport equation for the progress variable, which is defined as the mass fraction of the products of combustion, is applied for flame propagation tracking:

$$\frac{\partial}{\partial t}\left(\overline{\rho}\widetilde{c}\right)+\frac{\partial}{\partial x_j}\left(\overline{\rho}\widetilde{u}_j\widetilde{c}\right)=\frac{\partial}{\partial x_j}\left(\frac{\mu_{eff}}{Sc_{eff}}\frac{\partial\widetilde{c}}{\partial x_j}\right)+\overline{S}_c.$$

The source term in the progress variable equation can be written using the gradient method (Prudnikov, 1967) as:

$$\overline{S}_c=\rho_u S_T\left|grad\ \widetilde{c}\right|,$$

where $|grad\ \tilde{c}|$ is the gradient of the progress variable. Using this method the integral of the source term through the numerical flame front thickness gives the same mass burning rate per unit flame surface area, $\rho_u S_T$, independent of the size of cells in the numerical front. The molecular Prandtl number and Schmidt numbers are both set to 0.7, reflecting the characteristics for air. The effective viscosity, effective Prandtl number and Schmidt number is calculated according to the renormalization group (RNG) theory (Yakhot, Orszag, 1986).

Due to the large scale, real world, experimental problems investigated in this study, the effects of turbulence and combustion instabilities must be modelled. This combustion model has been implemented through the utilisation of an appropriate user-defined function (UDF) available within the solver employed (ANSYS Fluent 14.0).

Multi-phenomena turbulent burning velocity model

The latest version of the multi-phenomena turbulent burning velocity deflagration model is described in (Molkov, 2012) and takes into account various phenomena affecting the turbulent burning velocity. The equation describing the turbulent burning velocity (Molkov, 2012) is written as:

$$S_T=S_u^w\cdot\exp\left(u'/S_T\right)^2=\left[S_u\cdot\Xi_K\cdot\Xi_{lp}\cdot\Xi_f\right]\cdot\exp\left(u'/S_T\right)^2,$$

where u' is the sub-grid scale (SGS) turbulent flow velocity (Pope, 2000). This equation is a modified form of Yakhot's original equation (Yakhot, 1988). The key step in the development of this model is the substitution of the laminar burning velocity term in Yakhot's original equation, S_u, with SGS wrinkled burning velocity, S_u^w. This introduced term accounts for the unresolved phenomena affecting burning rate at all SGS lengths. It should be noted that S_u^w influences the total turbulent burning rate through interaction with flow turbulence in the unburned mixture. Within the mechanisms contained within this equation, the dependence of the laminar burning velocity on transient pressure and temperature is taken into account following the assumption of adiabatic compression/expansion. This requires the calculation of the thermokinetic index which is taken from (Babkin, 2003), as $\varepsilon = 0.65$. The characteristic radius R_0 at which transition to the fully turbulent self-similar regime occurs is set to 1 m

(Gostintsev et al., 1989). The 'ad-hoc' parameter ψ contained with the model ($\psi < 1$) is set to 0.5 following (Verbecke, 2009).

4.2.3.2 Simulation approach

Calculation domain

As shown in Figure 4-39 and in Figure 4-40 in the area of combustion the calculation domain was meshed using tetrahedral control volumes (CVs). In the vicinity of the pressure sensor locations, hexahedral CVs were implemented. These CVs were more refined in these areas of interest. The rest of the calculation domain was occupied using much less defined hexahedral CVs.

The total number of CVs in the calculation domain was 353,422, with the average CV size in the area of combustion equal to 0.77 m and the ignition cell size equal to 0.77 m.

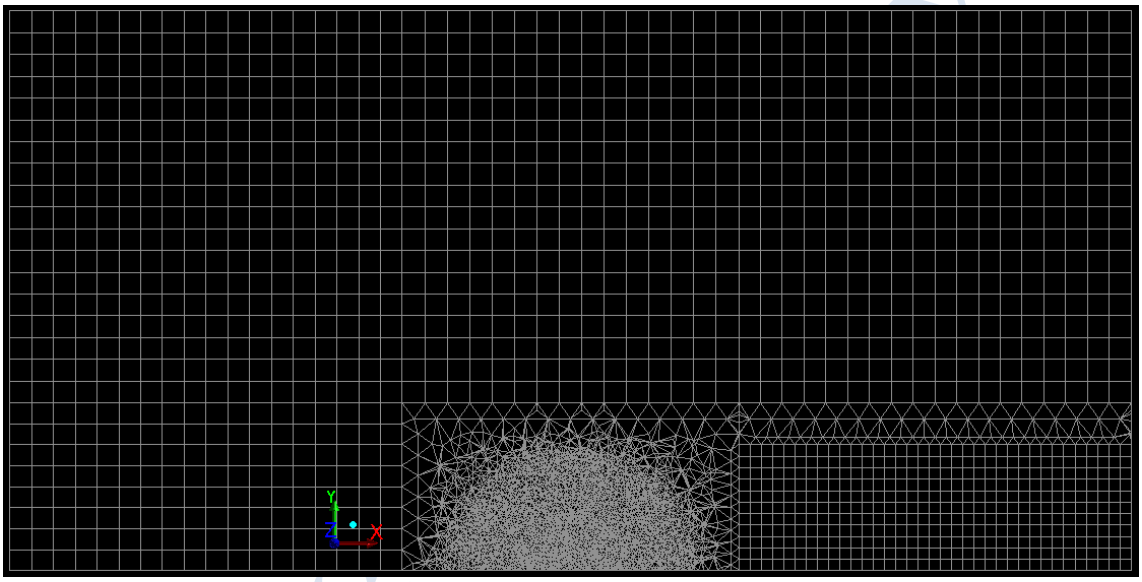

Figure 4-39: Calculation domain for test GHT 34, LES simulation.

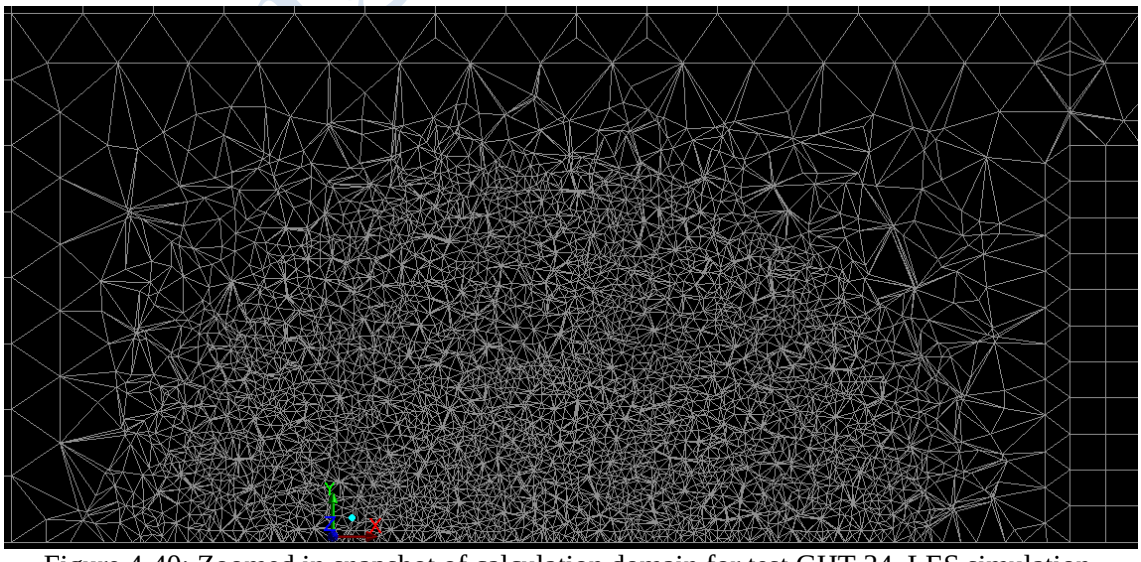

Figure 4-40: Zoomed in snapshot of calculation domain for test GHT 34, LES simulation.

A grid sensitivity analysis was undertaken for this test. The original grid, shown in Figure 4-39 and in Figure 4-40 and, was compared against a simulation undertaken using an adaptive grid. The LES model reproduces overpressures within $\pm 10\%$ (which complies with the requirements for grid sensitivity as outlined in (Pope, 2004)).

Initial and Boundary Conditions

Initial temperature and initial pressure were set to 283 K and 98.9 kPa (as per the experiment). The mixture was initially quiescent. The progress variable was equal to $c = 0$ throughout the domain. Air concentration was equal to $Y_a = 0.9713$ (for hydrogen $Y_{H2} = 0.0287$) within the hydrogen-air cloud, outside this cloud it was $Y_a = 1$ (for hydrogen $Y_a = 0$).

Non-slip impermeable adiabatic boundary conditions were used for the ground. Non-reflecting boundary conditions, as implemented by ANSYS Fluent based on Riemann invariants, were used for the boundaries representing the far-field in the atmosphere.

Ignition was modelled by increasing the progress variable from $c = 0$ to $c = 1$ in one CV. Duration of ignition was assumed to be equal to the flame propagation time from the centre to the edge of the ignition CV: $\Delta t_{ign} = 1/2 \cdot (\Delta_{CV}/S_u \cdot E)$.

4.2.3.3 Numerical details

- Code: The model was realised using ANSYS Fluent 14.5
- Discretisation: finite volume
- Solver type: coupled, density based solver
- Numerical scheme for convective terms: second order upwind
- Transient numerical scheme: explicit time stepping
- CFL number: 0.8

4.2.3.4 Results and discussion

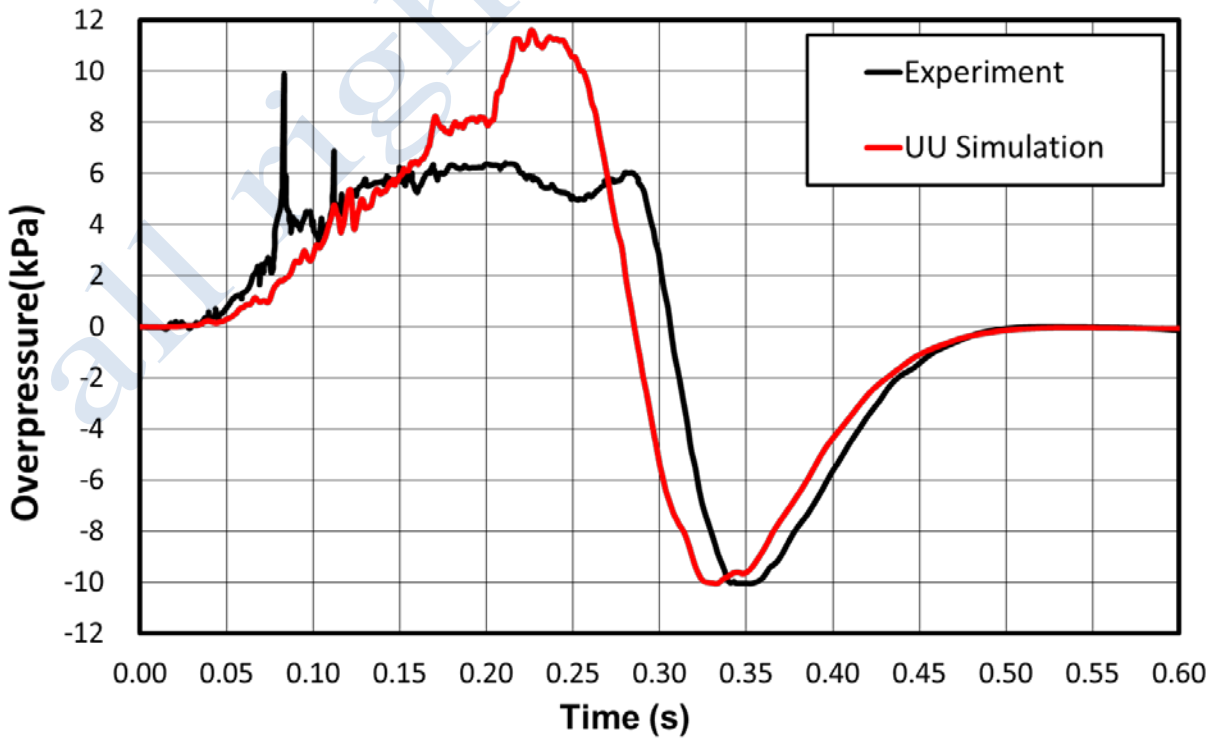

Figure 4-41: Experimental and simulated overpressure dynamics for test GHT 34: *R* = 5 m.

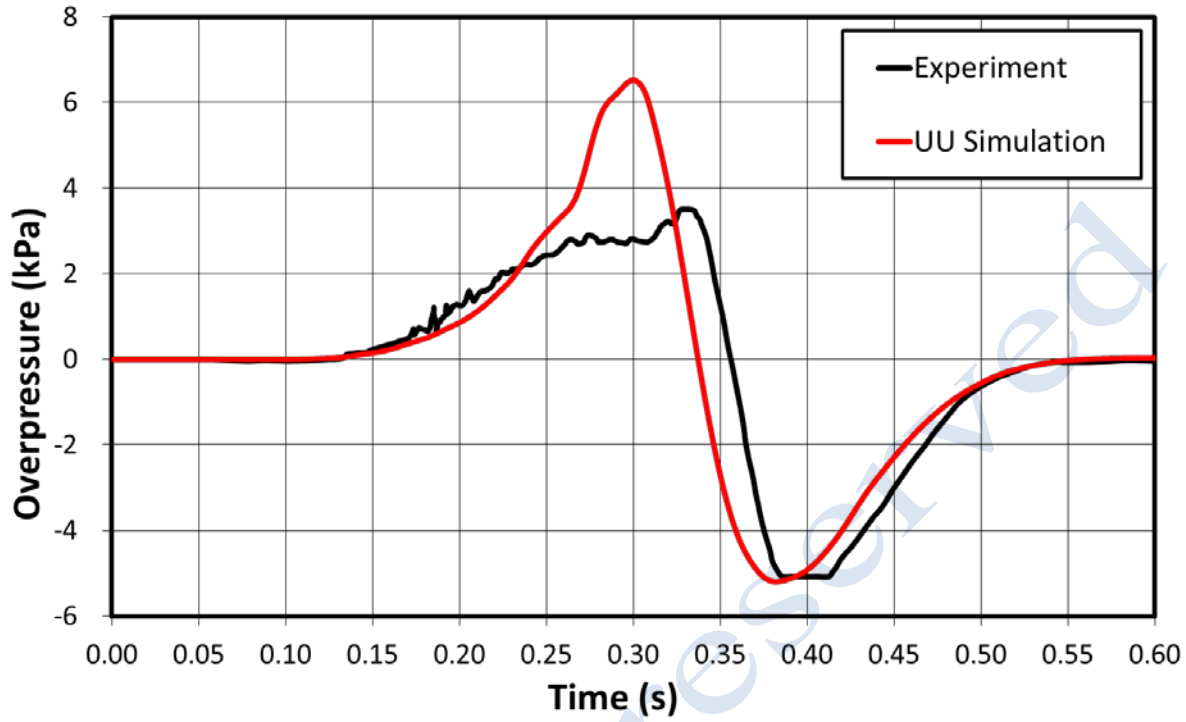

Figure 4-42: Experimental and simulated overpressure dynamics for test GHT 34: *R* = 35 m.

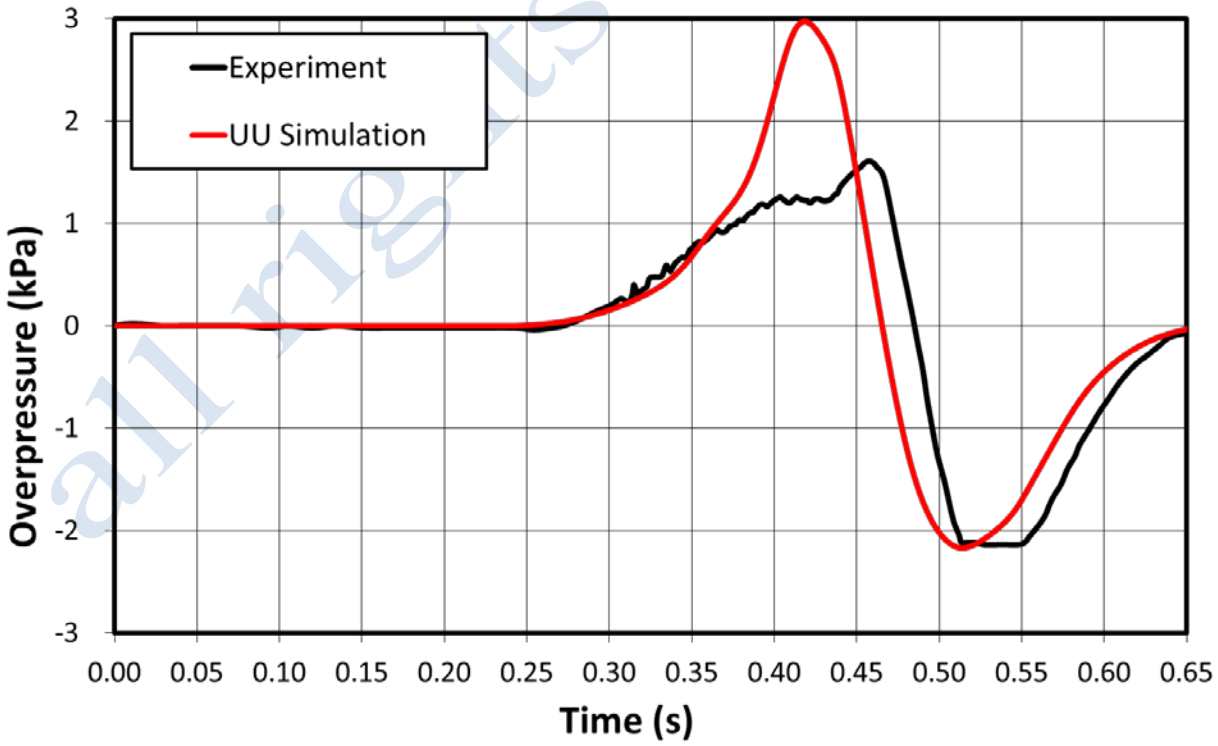

Figure 4-43: Experimental and simulated overpressure dynamics for test GHT 34: *R* = 80 m.

4.2.3.5 Conclusions

Simulations were conducted using the most up-to-the-date realisation of multiphenomena combustion being developed at Ulster University using the same numerical grid as in the previous validation exercise (Verbecke, 2009).

Simulation results for pressure dynamics are in a good agreement with the experimental measurements.

Simulation results are practically identical to simulation results with the previous realisations of UU combustion model (Verbecke, 2009), which were demonstrated for grid independence.

4.2.4 Overall conclusions

The large scale open deflagration experiment of a hydrogen-air mixture equal to 29.7% by volume in a 20 m diameter hemisphere was simulated by NCSRD and UU. Both partners used the "Multi-phenomena turbulent burning velocity model" model. Differences in the results are observed although. Even though the combustion and the turbulent model used were the same, differences in the simulation approach may affect the results. Firstly, the numerical grid is different. UU uses unstructured grid whereas NCSRD uses structured grid. Due to the spherical geometry of the problem, structured grid may not be appropriate and may have an impact on the results. Secondly, different values of some model parameters were chosen from the partners, e.g. the thermokinetic index e and the characteristic radius R_0. Finally, some implementation details of the model are different, e.g. NCSRD does not use the progress variable equation but it solves for the conservation equation of each of the species mass fraction that takes part in the combustion. A more thorough analysis is required in order to gain a better insight on the reasons of the discrepancies.

4.2.5 References

Babkin, V. S., 2003. Private communication. Institute of Chemical Kinetics and Combustion, Siberian Branch, Russian Academy of Science, Novosibirsk, Russia

Bak, P., Chen, K. and Tang, C. (1990), "A forest-fire model and some thoughts on turbulence." Phys. Lett. A 147, 297 300

Efimenko A.A., Dorofeev S.B. CREBCOM code system for description of gaseous combustion. Journal of Loss Prevention in the process industries. 2001;575-581

Fureby, C., On modelling of Unsteady Combustion utilizing Continuum Mechanical Mixture Theories and Large Eddy Simulation

Gostintsev, Y. A., Istratov, A. G., Shulenin, Y. V., 1989. Self-similar propagation of a free turbulent flame in mixed gas mixtures, *Combustion, Explosion and Shock Waves*, 24 (5)

Harten A. High resolution schemes for hyperbolic conservation-laws. *Journal of Computational Physics*, 49:357--393, 1983.

Jones and Launder. The prediction of laminarization with a two equation model for turbulence. Int. J. Heat Mass Transfer 15, 301-314 1972

Molkov, V., 2012. *Fundamentals of Hydrogen Safety Engineering, parts I & II*. Free download e-book, bookboon.com, ISBN: 978-87-403-0279-0

Molkov, V., Makarov, D., Schneider, H., 2006. LES modelling of an unconfined large-scale hydrogen-air deflagration. *Journal of Physics D (Applied Physics)*, 39(20), pp.4366–76

Pope S. B., 2004. Ten questions concerning the large-eddy simulation of turbulent flows, *New Journal of Physics*, 6 (35)

Pope, S. B., 2000. *Turbulent Flows*. Cambridge University Press

Porter, H., Schneider, H., 1983. "Research program - Release and explosion of gas and the effects of containment on the pressure waves. Balloon experiments to investigate the deflagration of hydrogen / air mixtures (Final report). (Translated from German - Forschungsprogramm “Prozeßgasfreisetzung - Explosion in der Gasfabrik und Auswirkungen von Druckwellen auf das Containment”. Ballonversuche zur Untersuchung der Deflagration von Wasserstoff/Luft-Gemischen (Abschlußbericht))", Fraunhofer Institute for propellant and explosive materials, ICT Projektforschung 19/83, Dec. 1983

Prudnikov, A. G., 1967. Burning of homogeneous fuel-air mixtures in a turbulent flow. *Physical Principles of the Working Process in Combustion Chambers of Jet Engines, B.V. Raushenbakh, Ed., Chapter 5, Clearing House for Federal Scientific & Technical Information, Springfield, Ohio, USA*, pp. 244–336

Schmidt HP, Habisreuther P, Leuckel W. Comb Flame 1998;113:79

Tolias, I.C. et al., 2014. CFD modeling of hydrogen deflagration in a tunnel. *International Journal of Hydrogen Energy*, 39(35), pp.20538–20546

Venetsanos, A.G., Papanikolaou, E. & Bartzis, J.G., 2010. The ADREA-HF CFD code for consequence assessment of hydrogen applications. *International Journal of Hydrogen Energy*, 35(8), pp.3908–3918

Verbecke, F., 2009. Formation and Combustion of Non-Uniform Hydrogen-Air Mixtures. Ph.D Thesis, HySAFER centre, University of Ulster, Newtownabbey, N. Ireland, U.K.

Yakhot, V., 1988. Propagation velocity of premixed turbulent flames, *Combustion Science and Technology*, 60, pp.191–214

Yakhot, V., Orszag, S. A., 1986. Renormalization group analysis of turbulence. I. Basic theory. *Journal of Scientific Computing*, 1(1), pp.3–51

Yanez, j, Kuznetsov, M. and Redlinger, R. The acoustic–parametric instability for hydrogen–air mixture. Combustion and flame, 160 (2013) 2009-2016

5. Detonation Benchmark

5.1 RUT experimental series

5.1.1 Experimental description

In order to support the WP3 'Best Practise in Numerical Simulation', several experiments in the validation database have been selected as the benchmarking to help people who have no much experience in validation.

Among the experiments, KI-RUT-HYD05 and KI-RUT-HYD09 (S. B. Dorofeev et al.) are selected as the benchmarking in detonation simulation. The two experiments are given in the 60m long RUT facility. In the two experiments, different premixed hydrogen-air mixtures and ignition points are given. Basic geometry of the RUT facility is given in Figure 5-1.

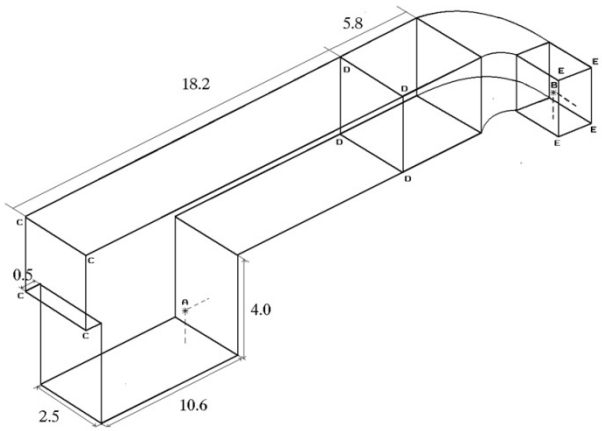

Figure 5-1. Geomerty of RUT facility

Size of the RUT facility is in the same magnitude of common industrial facilities, so numerical reproduction of detonation waves inside such size of facility may have very good practical meaning. In addition, thanks to the complex geometry, simulation of detonation in the RUT facility may also be a good test of the compatibility of the numerical models to computational domain with complex geometries.

In the two experiments, both hydrogen concentrations and ignition positions are different. In the Figure 5-1 two ignition points are indicated. The ignition point A is given in the corner of the canyon and the ignition point B is given in the end of the curved channel, both ignition points are located 80 cm to the floor and 50 cm to the wall. High explosive charges (TNT) are given in the two ignition points to initiate the detonation wave directly. Details of experiments such as the hydrogen concentrations and the ignition points are given in Table 5-1.

Table 5-1. Experimental details

File name	Volume of gas (m^3)	H_2 concentration (%vol)	Ignition point	Mass of the explosive charge (g)

KI-RUT-HYD05	263	20.0	A	200
KI-RUT-HYD09	263	25.5	B	200

The mixture temperature and pressure were 20°C and 1 atm in both experiments. Mixing was assured by fans. Hydrogen concentration and mixture uniformity were checked by taking samples from two points of the experimental volume. It was found that the uniformity was less than 0.5% vol. on hydrogen concentration.

To collect experiment data in the experiments, several pressure transducers are installed in the RUT facility. In the following figure, locations of the 11 transducers are given.

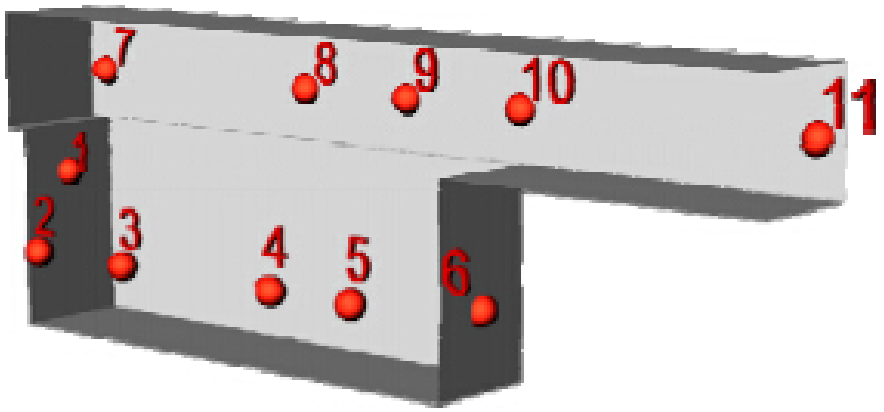

Figure 5-2. Transducers in RUT facility.

Shown as the figure, transducers 7-11 are installed on the rear wall of the channel, they are more likely installed for detecting the propagation of detonation wave initiated at the end of the channel. Transducers 2-5 are installed on the front wall of the canyon, so they are more proper for recording the detonation wave initiated in the canyon.

5.1.2 KIT modelling

5.1.2.1 Governing equations

Since the molecular transportation effects and heat transfer can be ignored in the transportation of detonation, the Euler equations are used to simulate the gas dynamics in detonation wave.

Size of the RUT facility is in the same magnitude as the common industrial facility, to control the total computational efforts considerably coarse (compared with the thickness of the induction zone and reaction zone of the detonation wave) mesh size should be used. In this case, in order to represent the correct physical phenomena of detonation wave in such coarse resolution the Heaviside detonation model should be used in the chemical reaction part (Kotchourko A. et al. 2014). This model allows defining the consumption of fuel

$$\Delta y_{H_2} = 100 \cdot C_f \frac{\Delta t}{\Delta x} y_{H_2} \cdot R_r \tag{5.1.1}$$

This consumption formula has no real physical interpretation, it is just a mechanism to provide enough variation of the species and heat release to generate and maintain the detonation.

Here C_f is the constant of the model of the order of 6. The model shows almost no influence of the C_f constant as the R_r factor works as a shocking capturing algorithm.

The "Heaviside" factor R_r is defined with

$$R_r = \begin{cases} 0 & T < T_0 \\ \dfrac{T - T_1}{T_1 - T_0} & T_0 < T < T_1 \\ 1 & T > T_1 \end{cases} \quad (5.1.2)$$

The values of the temperatures, for this model, are:

$$T_0 = 800K$$
$$T_1 = 1700K$$

5.1.2.2 Simulation approach

Besides the selection of numerical models, preparation of the simulation such as the construction of the computational domain, setting of the boundary conditions and setting of the initial conditions are all very important.

Domain setting

In some experiments with tube or channel, the facility may be symmetric in some directions and bring lots of conveniences in constructing half or even a quarter of the facility (by using the mirror boundary) to save computational efforts. However the RUT facility is not symmetric in any directions, the full geometry should be constructed in the computational domain. In this case, grids size should be coarse to keep the total computational effort under an acceptance level. Combustion simulation code COM3D is used to make the two detonation simulation, in the code only the uniform Cartesian grid is available.

Thanks to the code's capability of parallel calculation, considerable fine grid (compared with the acceptable resolution for serial simulation code) can be used in the construction of the computational domain. In order to achieve a better performance, resolution 0.05m is used to construct the computational domain. Under the 0.05m resolution, the domain has the size of 555X110X126 cells and the total cell number is 7.7 million.

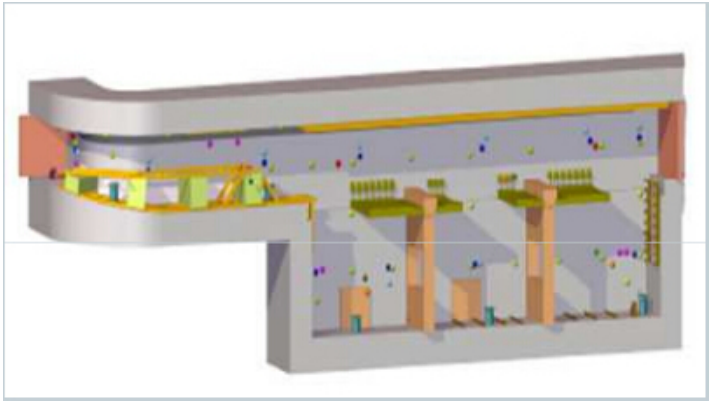

Figure 5-3. Details of RUT facility.

In the construction of computational domain, representation of the details of the geometry is another important point needed to be take care. Figure 5-3 shows a more detailed description of the RUT facility, inside the facility there are still some detailed structures such as the bolts, transducers and steel lines for supporting. To produce a numerical simulation being compatible to the reality, it is better to include all the details in the real facility in the computational domain. Figure 5-4 and Figure 5-5 show the details in canyon and channel of the RUT facility in computational domain with resolution 0.05m.

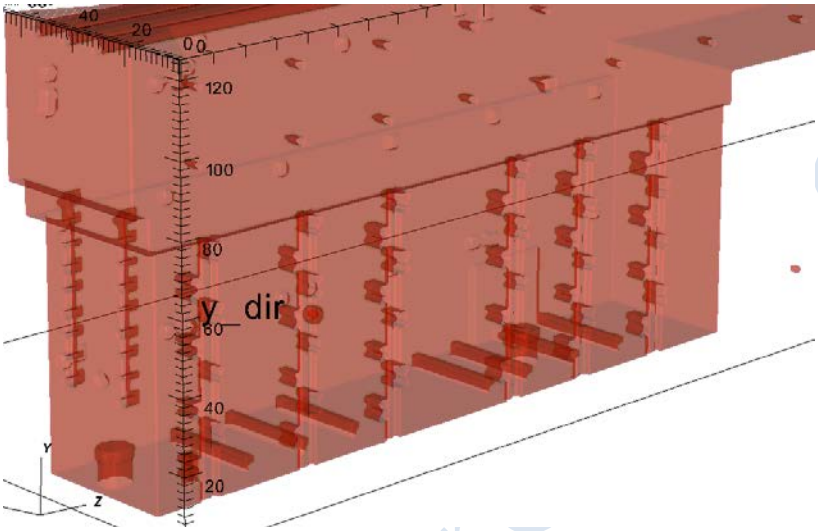

Figure 5-4. Details in canyon of RUT facility.

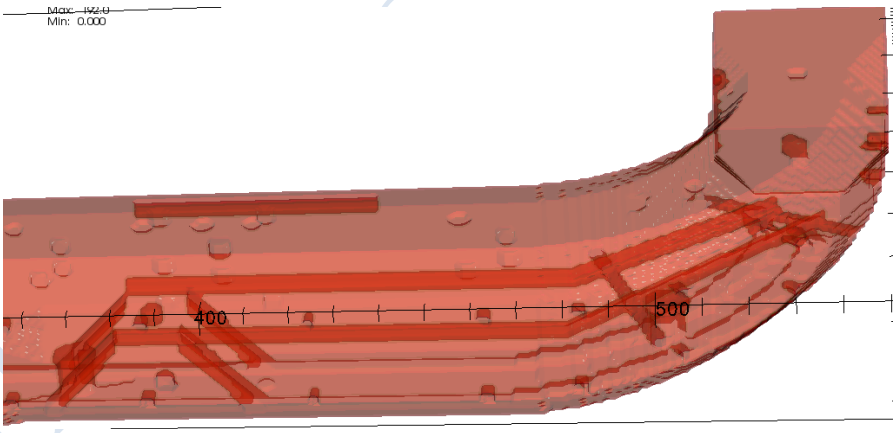

Figure 5-5 Details in channel of RUT facility

The details of the RUT facility are transported from the CAD file provided by the experiment agency. However, restricted by the resolution of the domain, the details have the size less than 0.05m are ignored in the domain construction. Comparing to the size of the facility, the inaccuracies resulted by the resolution can be ignored.

Boundary setting

The descriptions of the two experiments show that the RUT facility is a closed vessel. Although some fans are installed in the facility to mix the hydrogen and air uniformly, they are closed several minutes before the ignition. So there are no boundaries such as the open

boundary or velocity in boundary. Attentions should be focused on the setting of the wall boundaries.

As mentioned in section 5.1.2.1, the effects of molecular transportation such as viscosity, diffusion and heat conductivity can all be ignored in detonation and the Euler equations are used to describe the basic gas motion in detonation propagation. So in the boundary setting, both slipping boundary (mirror boundary) and non-slipping boundary (wall boundary) can be used. As the wall boundary is the default option for the setting of boundary condition in code COM3D, the wall boundary is set in the computational domain.

Initial setting

In the setting of initial conditions, most of the working efforts are focused on the initiation of detonation. In the experiments, ignitions are achieved by 200 gram high explosive charges. In such situation the detonation is thought to be initiated directly without the DDT process. In numerical simulation, such detonation initiator can be described by a region with high pressure and high temperature. By consulting the energy release by TNT which is about 4.2kJ per gram, a 0.18m sphere structure region with 100 bar pressure and 3000K temperature should be given to reach such amount of energy. However, in case of the numerical diffusion brought by the coarse grids and the numerical scheme, larger initiator should be given in the simulation to avoid the decay of detonation wave. By several numerical testing, the sphere structure with the radius of 0.2m or bigger can initiate the detonation wave successfully. Figure 5-6 shows the initiator of detonation in simulation of experiment KI-RUT-HYD05 and Figure 5-7 shows the initiator of detonation in simulation of experiment KI-RUT-HYD09.

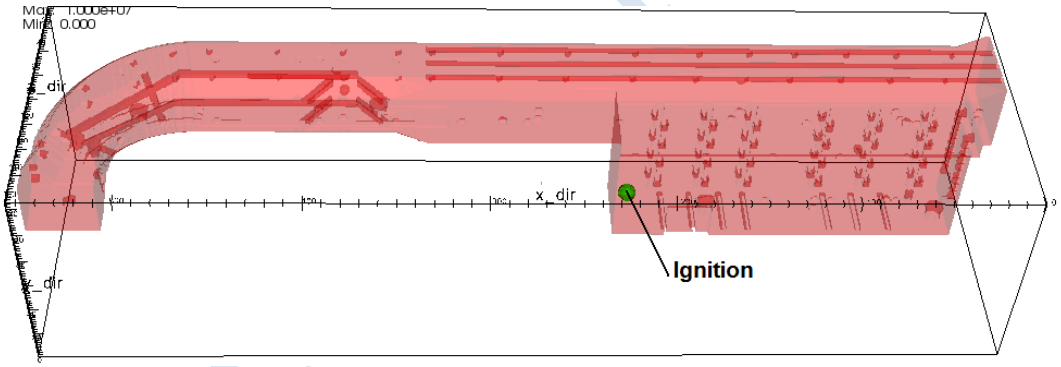

Figure 5-6. Initiator for numerical simulation of KI-RUT-HYD05.

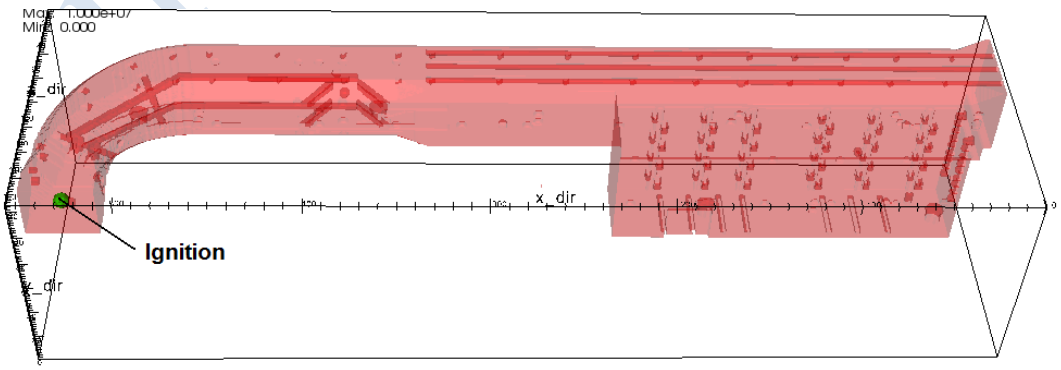

Figure 5-7. Initiator for numerical simulation of KI-RUT-HYD09.

The initial conditions setting for other regions (expect the initiator) follow the description of the experiments.

5.1.2.3 Numerical details

In the former section it has already been mentioned that the COM3D code is used to reproduce the two detonation experiments numerically. The version of the code is 4.7 which is released in 2014. The turbulent fluid dynamics code COM3D was developed at the Institute for Nuclear and Energy Technologies (IKET) in the Karlsruhe Institute of Technology (KIT) with the aim to simulate combustion including explosion and detonation, transport, and mixing of hydrogen and other gases in nuclear reactor containments and other industrial facilities. The turbulent reactive flow code is intended to model development of large-scale combustion events in geometrically complex environment with multiple compartments and internal structures in a multi-block computational domain.

Under the consideration of the fast process of the chemical ration in detonation and supersonic propagation speed of the wave, explicit methods are used in the simulation. Two finite discretization schemes are tried in the simulations: the van Leer flux splitting scheme (B. van Leer, 1982) and the TVNI scheme (Harten A., 1983). Both schemes are second order spatial discretization schemes and can simulate the propagation of detonation wave properly, but the van Leer flux splitting scheme shows worse performance in simulation the reflection wave due to its high diffusivity. So, the TVNI scheme is finally selected to make the simulations.

For explicit solvers, the CFL number should be strict less than 1.0 to avoid the divergence of the error in explicit iteration. However, to avoid some unphysical oscillations, CFL number should be less than 0.3 or even 0.2. Default CFL number for the van Leer flux splitting method is less than 0.2 and the optimal CFL number for the TVNI scheme is around 0.37. In this case the CFL 0.2 number is used in simulations of both experiments.

5.1.2.4 Results and discussion

Simulation for KI-RUT-HYD05

In the experiment KI-RUT-HYD05 20% vol. hydrogen was ignited at the corner of the canyon. In simulation of this experiment, comparisons of numerical simulation and experiment data are focused on the transducer 2-5 (shown as the Figure 5-8).

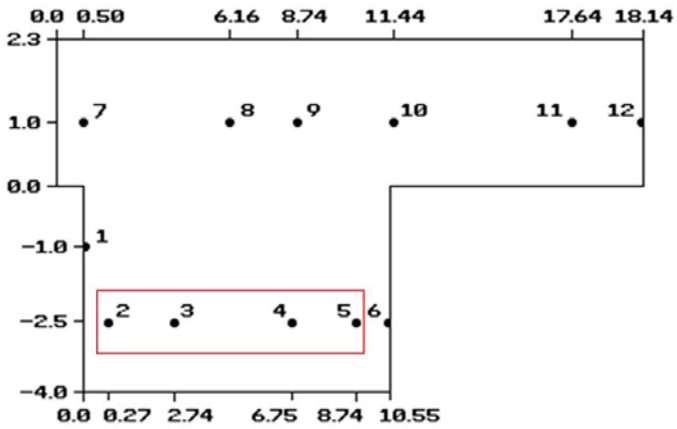

Figure 5-8. Transducers focused in KI-RUT-HYD05.

In comparisons between the simulation results and experiment results, shock wave at one transducer should be synchronized and then comparisons at other transducers are made to show if the numerical model can represent the real world. In this experiment, transducer 5 is the nearest one to the ignition point and its result is selected for synchronization. Figure 5-9 is the synchronization of experiment and simulation at transducer 5.

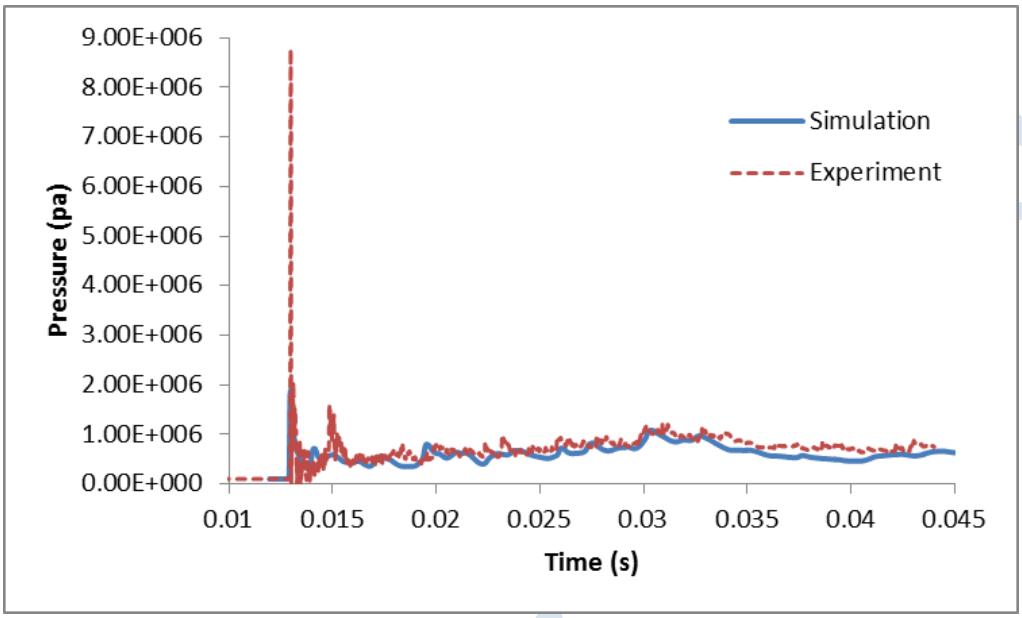

Figure 5-9. Synchronization at transducer 5.

Shown as Figure 5-9 two shock waves are synchronized, and then the simulation results are compared with the experiment results at the other 3 transducers by using the same time shift as at transducer 5 did. Figure 5-10, Figure 5-11 and Figure 5-12 show the comparisons at the transducer 4, transducer 3 and transducer 2.

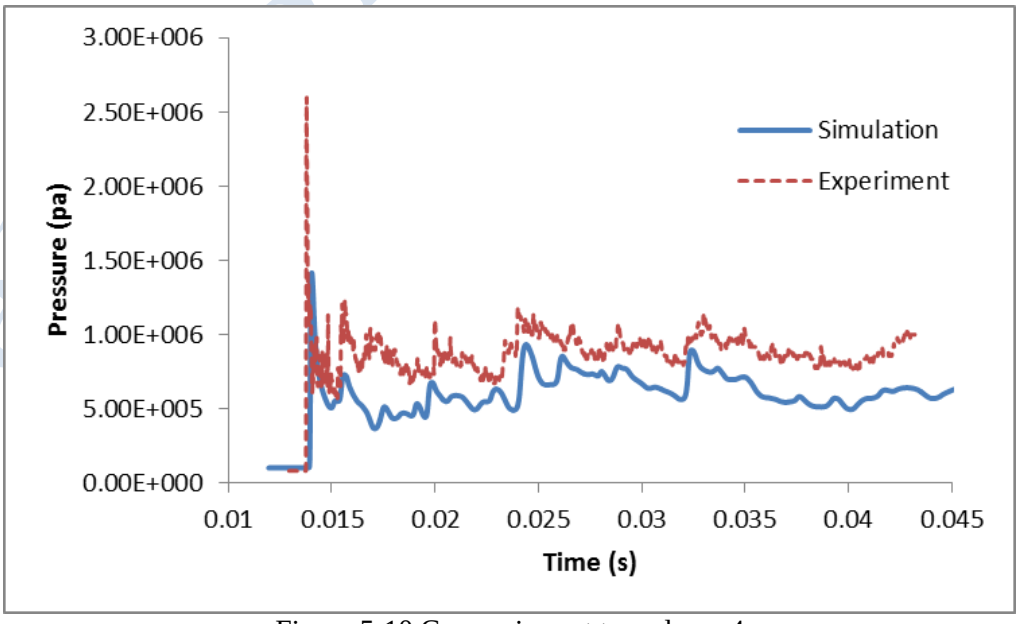

Figure 5-10 Comparison at transducer 4

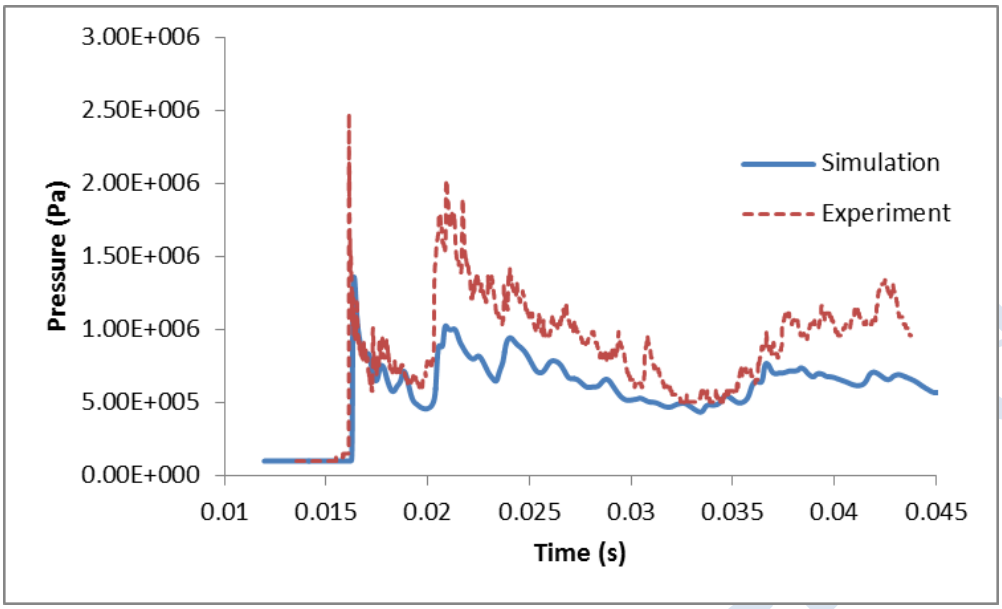

Figure 5-11. Comparison at transducer 3.

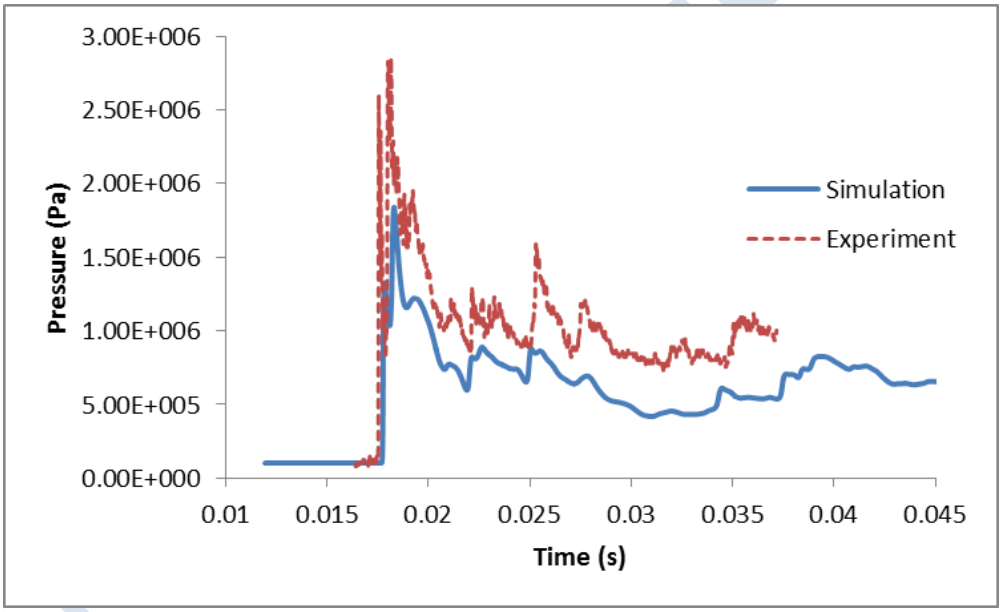

Figure 5-12. Comparison at transducer 2.

In the comparison of the three transducers we can found that the trends of the two curves (simulation curve and experiment curve) fit with each other quite well at each transducer. However, the shock fronts of the two curves do not fit with each other at each transducer and the propagation of detonation wave in experiment shows a faster speed. Theoretically the real world detonation wave may transfer slower than the numerical simulation because of the heat losses exist in the real world, but the detonation wave in the real world should not travel in a faster speed than the numerical simulation. Figure 5-13 shows the R-t diagram of the experiment and simulation, detonation propagation speed and the speed of the reflection are shown by the slope the lines in the diagram. In this figure the X axel is the time (ms) and the Y axel is the length (m), the experiment pressure curves and the simulation pressure curves of transducers 5-2 are given from top to bottom. It is clear that the propagation speed of

detonation maintain a constant speed but the propagation speed of the detonation in experiment was very high at the very beginning and later its propagation at almost the same speed as the numerical detonation. It is quite possible that the transducer 5 is too closed to the ignition point and the detonation wave it detected may still be driven by the explosive shock wave.

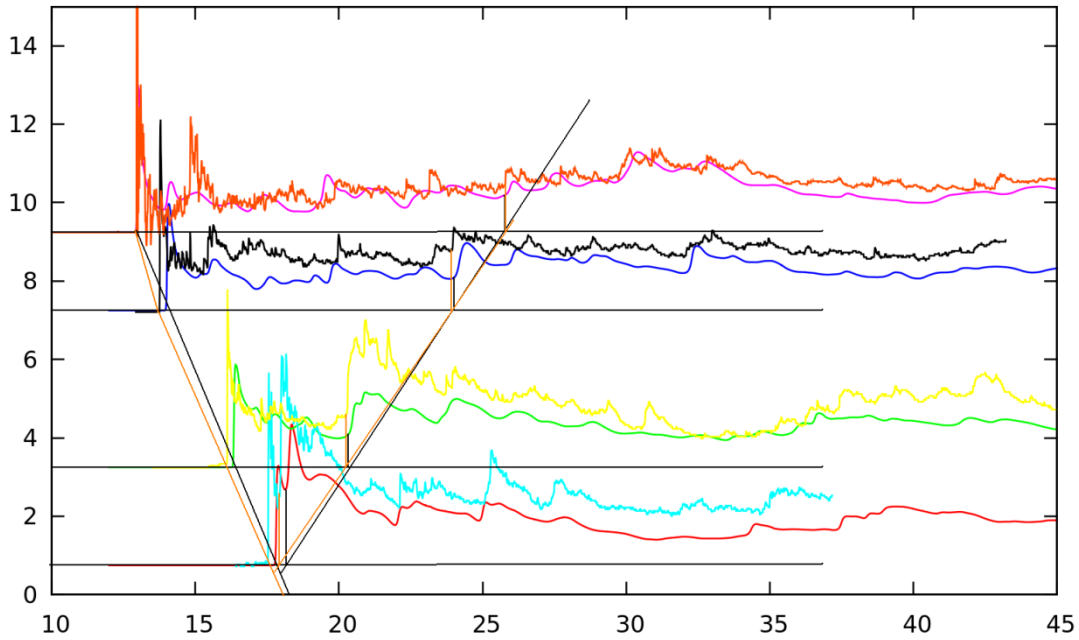

Figure 5-13. R-t diagram.

So, the synchronization between the simulation and the experiment should be made at transducer 4 instead of 5 to avoid the driven effect of the high explosive charges. Figure 5-14 shows the synchronization at transducer 4.

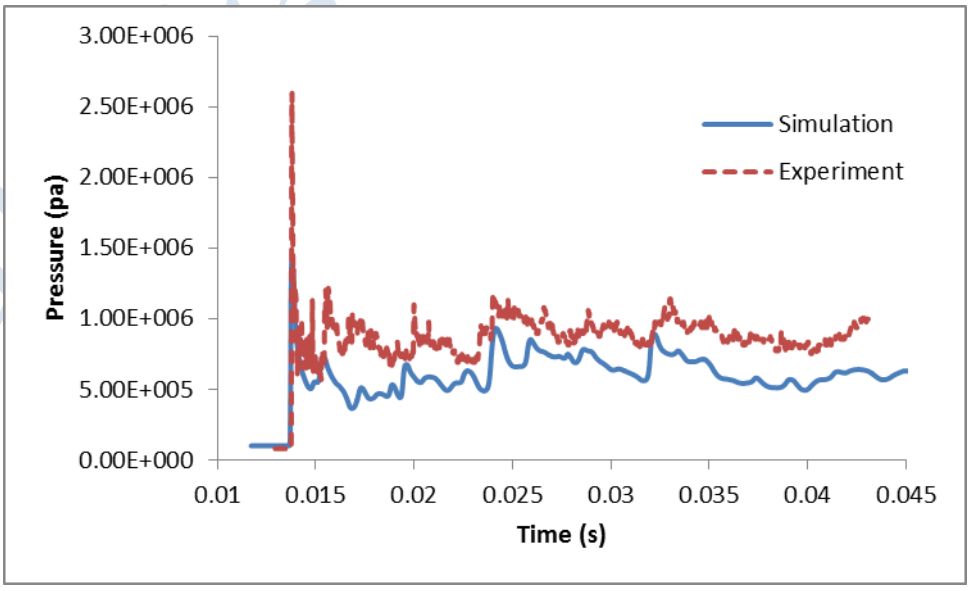

Figure 5-14. Synchronization at transducer 4.

Then, based on the time shift used in the synchronization at transducer 4, comparison between the simulation results and experiment results can be made on transducer 3 and transducer 2. Figure 5-15 and Figure 5-16 show the comparisons.

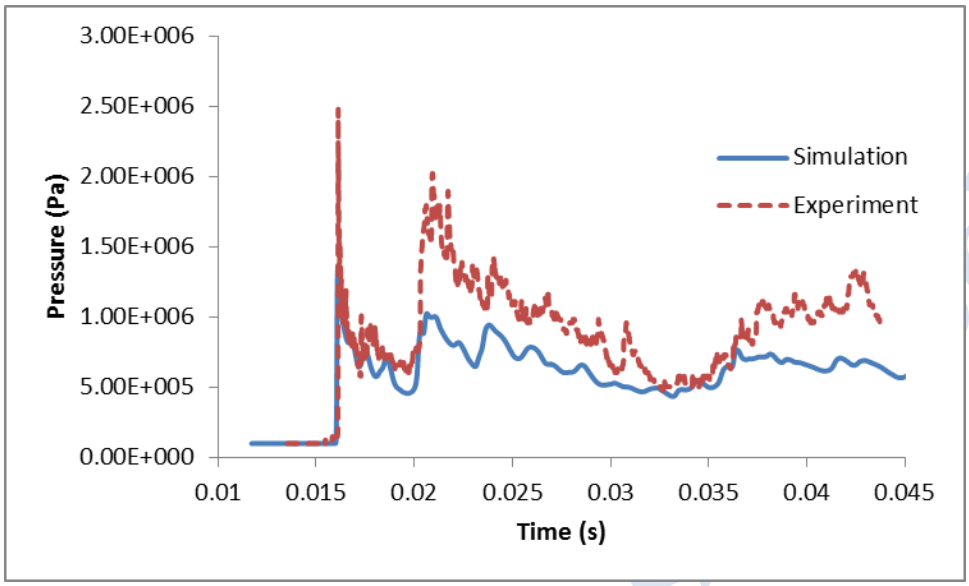

Figure 5-15. Comparison at transducer 3.

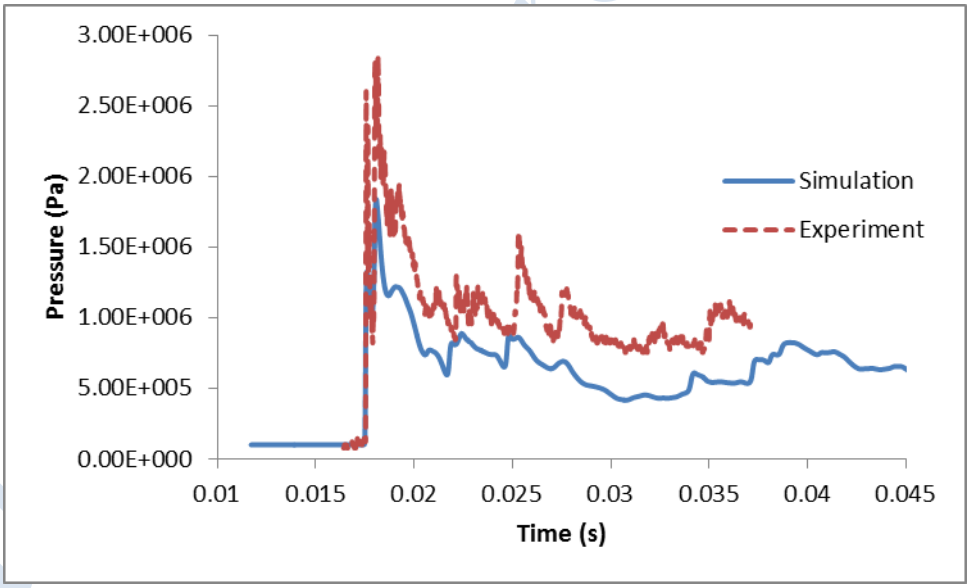

Figure 5-16 Comparison at transducer 2

It is clear that the shock front of the experiment curve and simulation curve fit with each other quite well at the two transducers after changing the synchronization from transducer 5 to transducer 4. The R-t diagram with the synchronization at transducer 4 is shown in Figure 5-17, in the figure the curves from top to bottom are the results at transducer 4, transducer 3 and transducer 2. At this moment the detonation in simulation shows the same propagation speed to the experiment. Then in the propagation of the reflection waves, since the reflection wave in simulation ignore the effects of energy losses due to heat transfer and friction, the simulation shows a faster speed than the experiment.

In all, with a proper synchronization of the experiment and numerical simulation the simulation results show quite good compatibility to the experiment results. At least in reproduction of the detonation in experiment KI-RUT-HYD05 the code COM3D shows quite good performances.

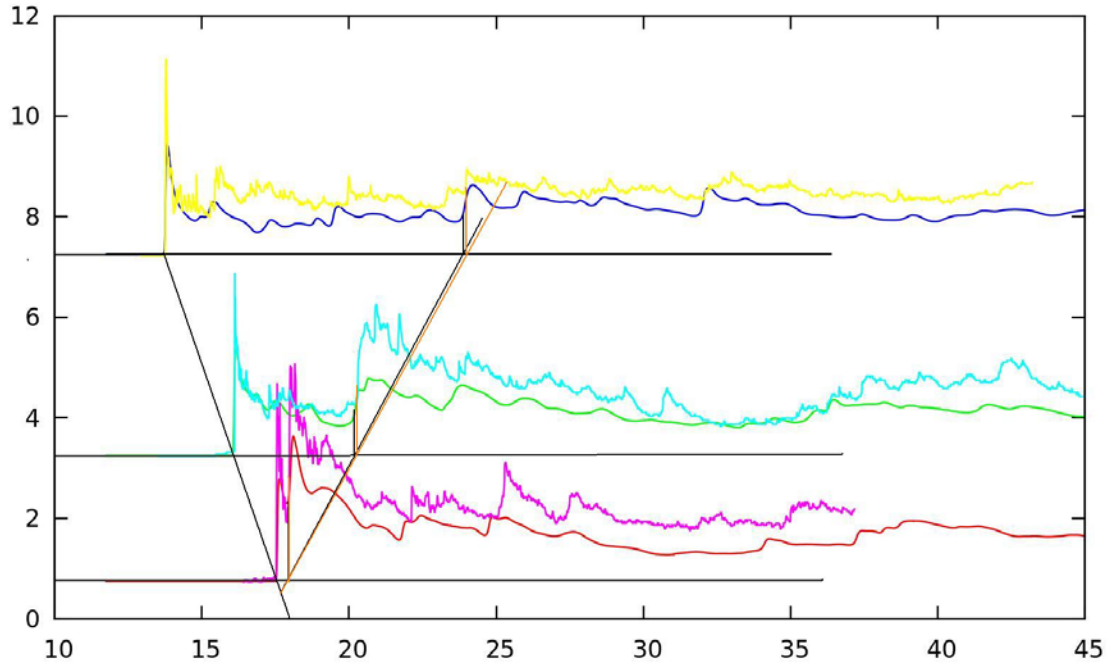

Figure 5-17 R-t diagram with the new synchronization

Simulation for KI-RUT-HYD09

In the experiment KI-RUT-HYD09 25.5% vol. hydrogen was ignited at the end of the curved channel. In simulation of this experiment, comparisons of numerical simulation and experiment data are focused on the transducer 7-11 (shown as the Figure 5-18).

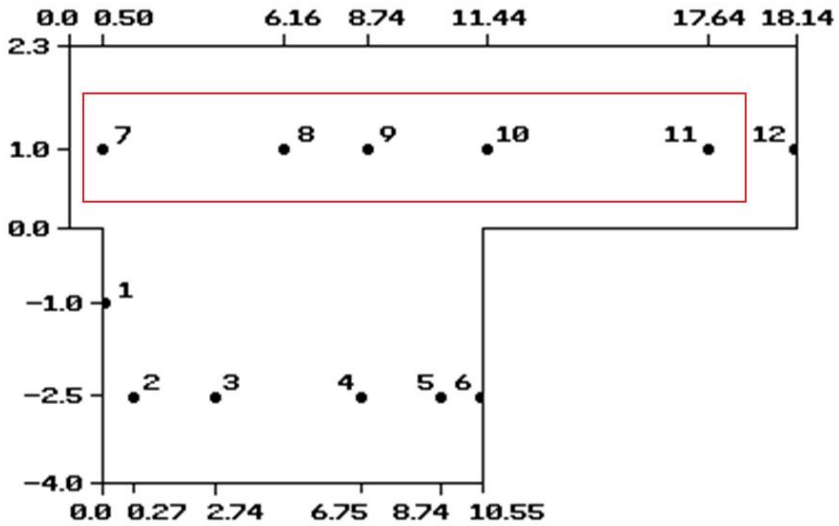

Figure 5-18. Transducers focused in KI-RUT-HYD09.

Similar to the simulation for KI-RUT-HYD05, experiment data and simulation results should be synchronized at one transducer and comparisons are made in the others. Ignition point in this experiment is given at the end of the channel, and transducer 11 is the nearest one among all the transducers. Figure 5-19 shows the synchronization of the pressure curves of experiment and simulation.

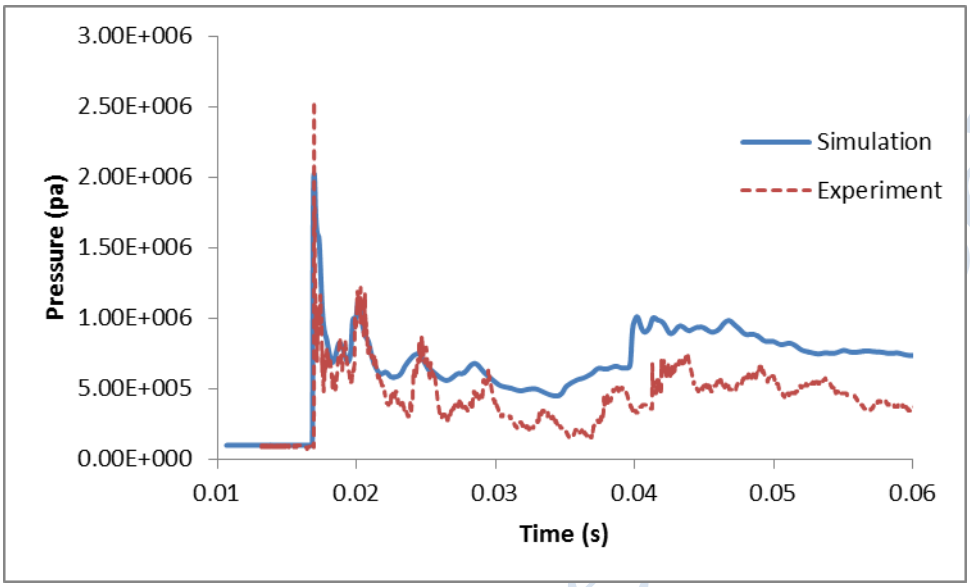

Figure 5-19 Synchronization at transducer 11

In the synchronization, simulation result shows the same trend to the experiment at the transducer 11. Then based on the same time shift, comparisons at the others transducers are made and the results are shown in Figure 5-20 -Figure 5-23. In all comparisons, simulation results show the similar trends as the experiments. However, the detonation shock of the simulation does not coincide with the experiment exactly, and as the shock wave approaching the end of the channel the difference becomes bigger.

Just as mentioned in the former section, numerical simulation does not include the influence of energy losses caused by friction and heat conductivity but the energy losses exit in reality. Since the energy released in the chemical reaction is used in propagation of detonation only, the detonation in numerical simulation may travel in a faster speed than the detonation in experiment. Therefore, in comparisons at the transducer 7-10, numerical results show a faster propagation speed.

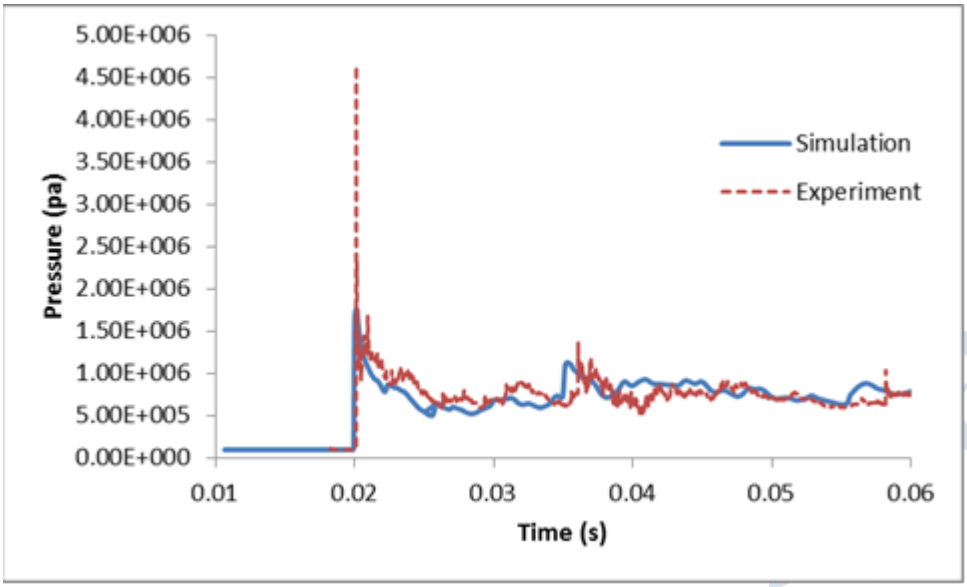

Figure 5-20. Comparison at transducer 10.

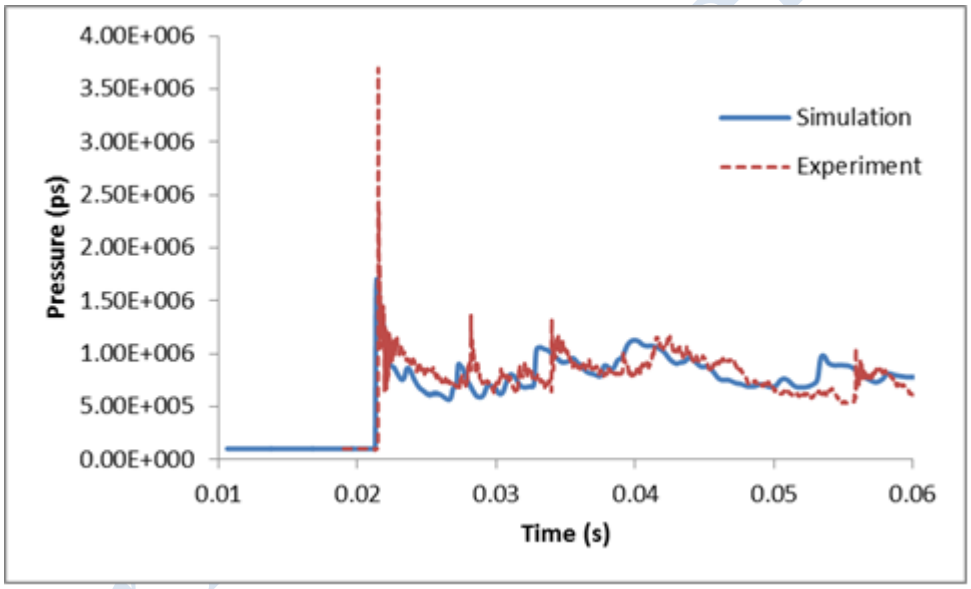

Figure 5-21. Comparison at transducer 9.

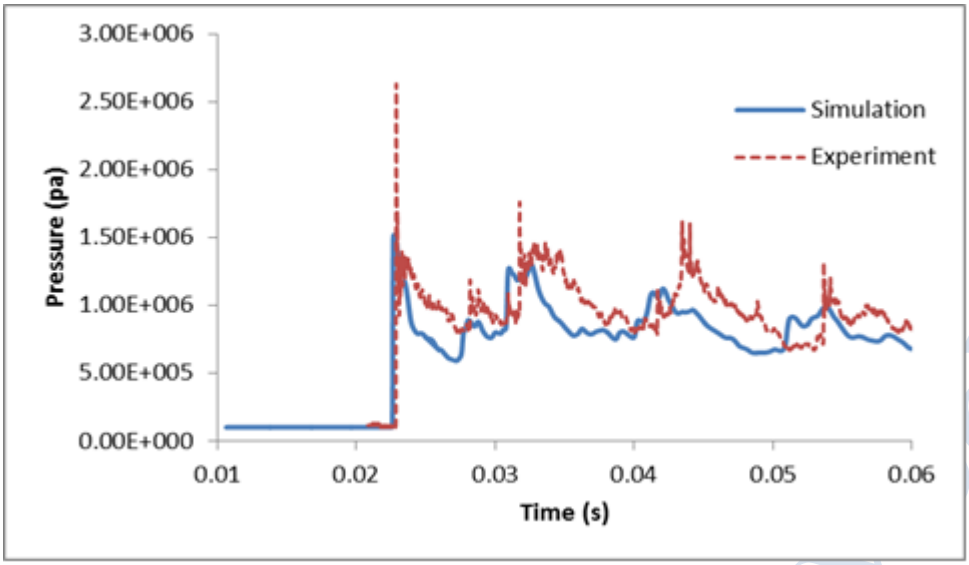

Figure 5-22. Comparison at transducer 8.

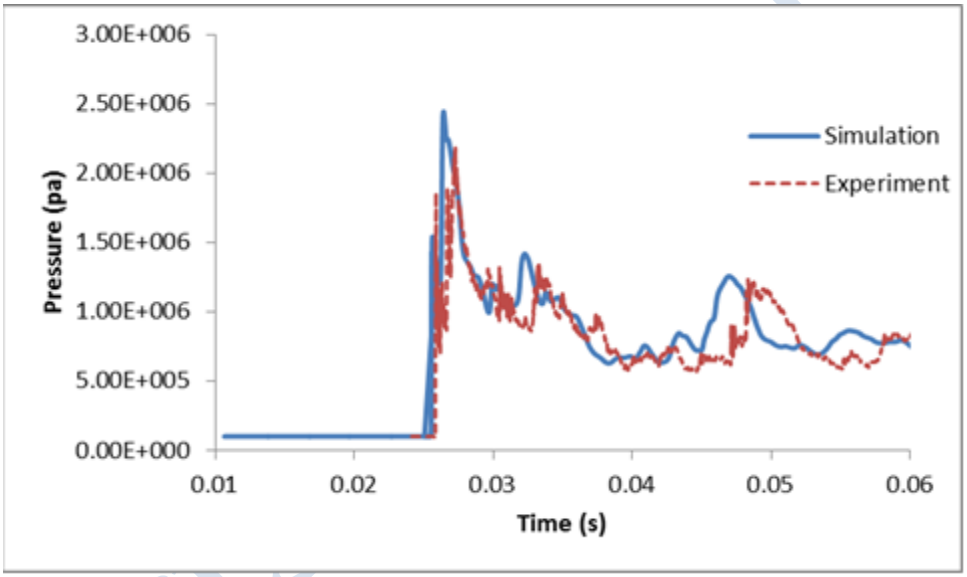

Figure 5-23. Comparison at transducer 7.

Figure 5-24. R-t diagram of KI-RUT-HYD09.Figure 5-24 is the R-t diagram of the experiment, comparisons of the pressure between simulation and experiment at sensor 7-11 are given from the bottom to the top. Corresponding to the analysis in former sentences, velocity slopes of detonation in simulation is bigger than the experiment which means that the numerical detonation wave travels faster than the one in experiment. Then, after reflecting of the two waves at position 0 (where the wall of the facility located), reflection in numerical simulation also shows faster propagation speed than the reflection in experiment. All of these differences in propagation speed between simulation and experiment are due to the ignoring of energy losses in numerical simulation.

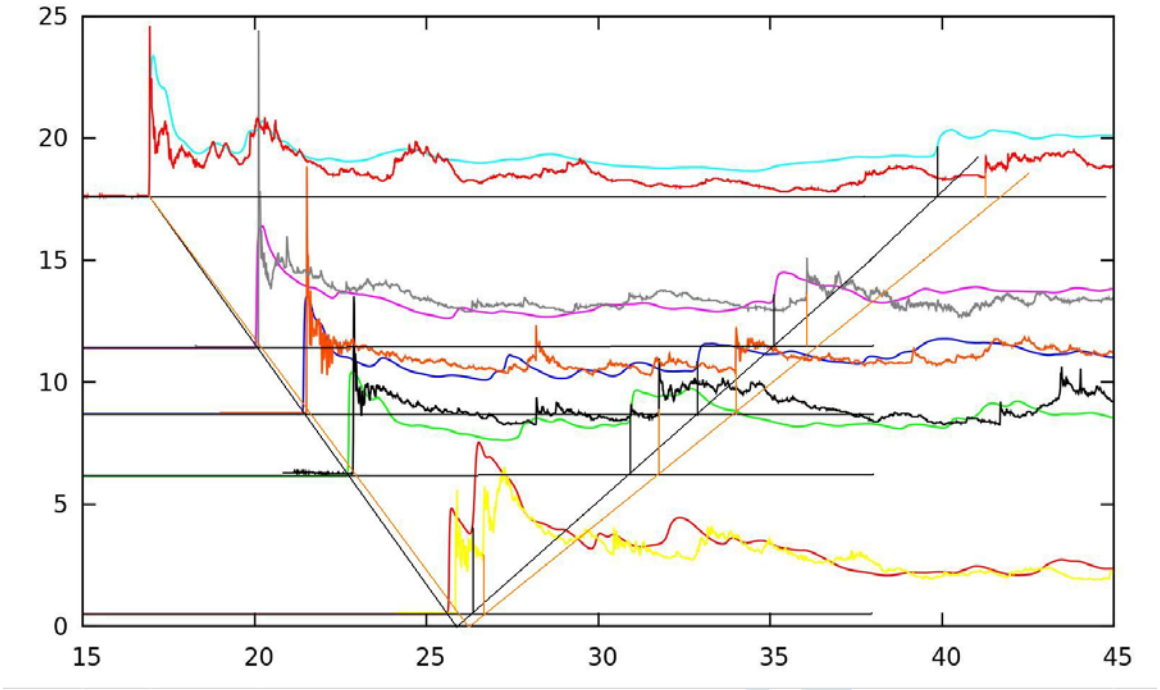

Figure 5-24. R-t diagram of KI-RUT-HYD09.

In general, numerical simulation made by COM3D can represent the physical properties of detonation in experiment. Faster propagation speed in numerical simulation is expected to be solved by using turbulence model in governing equation and proper wall functions.

5.1.2.5 Conclusions

This report includes the numerical simulations of detonation in RUT facility with the 20.0% vol. and 25.5% vol. of hydrogen and different ignition locations.

In the numerical simulations, 0.05m resolution is used to construction the computational domain and all the details of the facility are included in the computational domain. Simulation results made by the code COM3D shows very good agreement with the experiment results. Especially in the simulation of experiment KI-RUT-HYF09, comparisons between the simulation and experiment at each transducer show the numerical work can represent the real detonation quite well.

In the analysis of the simulations it is also been found that the commonly used Euler equations may results in the overestimation of the propagation speed of detonation wave and its reflection. In next step's work, more complicated turbulence models and wall functions are expected in simulation to reproduce better results.

5.1.3 References

B. van Leer, 1982, Flux Splitting for the Euler Equations, Report ICASE No. 82-30.

Harten A., 1983, High resolution schemes for hyperbolic conservation-laws. *Journal of Computational Physics*, 49, pp. 357--393.

Kotchourko A., Lelyakin A., Yanez J., Xu Z., Ren K., 2014, COM3D: Turbulent Combustion Code Tutorial Guide Version 4.7, KIT.

S. B. Dorofeev, V. P. Sidorov, S. M. Velmakin, A. V. Zhernov et al. Large Scal Hydrogen-Air Detonation Experiments, The effect of Ignition Location and Hydrogen Concentration on Load, Laboratory of induced Chemical Reactions. Russian Research Center “Kurchatov Institute”, Report number RRCKI-80-05/59.